# Electrochemical Study of the Corrosion of Stainless Steel 304, Nickel, and Inconel 600 in Molten Eutectic and Composite Salts

A Thesis

Presented in Partial Fulfillment of the Requirements for the

Degree of Master of Science

with a

Major in Nuclear Engineering

in the

College of Graduate Studies

University of Idaho

by

Eugene Tettey Engmann

Major Professor: Haiyan Zhao, Ph.D.

Committee Members: Richard Christensen, Ph.D.; Dong Ding, Ph.D.; Michael McKellar, Ph.D.

Department Administrator: Richard Christensen, Ph.D.

August 2019

## Authorization to Submit Thesis

This thesis of Eugene Tettey Engmann, submitted for the degree of Master of Science with a Major in Nuclear Engineering and titled "Electrochemical Study of the Corrosion of Stainless steel 304, Nickel, and Inconel 600 in Molten Eutectic and Composite Salts," has been reviewed in final form. Permission, as indicated by the signatures and dates below, is now granted to submit final copies to the College of Graduate Studies for approval.

| | | |
|---|---|---|
| Major Professor: | _____<br>Haiyan Zhao, Ph.D. | Date: _____ |
| Committee Members: | _____<br>Richard Christensen, Ph.D. | Date: _____ |
| | _____<br>Dong Ding, Ph.D. | Date: _____ |
| | _____<br>Michael McKellar, Ph.D. | Date: _____ |
| Department Administrator: | _____<br>Richard Christensen, Ph.D. | Date: _____ |

## Abstract

The electrochemical properties of stainless steel 304, Nickel, and Inconel 600 were investigated in a three-electrode electrochemical cell using $0.67Li_2CO_3$-$0.33K_2CO_3$ eutectic salt, and 0.3 GDC – 0.7 ($0.67Li_2CO_3$-$0.33K_2CO_3$) composite salt from 500 to 600 °C in the air. The aim of this study was to understand the corrosion mechanism that take place on these materials surface used as electrodes, and for materials screening in terms of corrosion resistance and polarization resistance in both salts. The electrochemical methods employed were Linear polarization resistance (LPR), Tafel analysis, and electrochemical impedance spectroscopy (EIS). The best scan rate of 1mV/s was determined for the LPR and Tafel measurements and used for all of the electrochemical measurements. According to both the LPR and EIS measurements, Stainless steel 304 demonstrated the highest resistance to corrosion in the eutectic salt with high resistance polarization ($R_p$) and Rct values (measure for charge transfer), and consistent and high P values (measure permeability of the salt through the oxide layer), which are owing to stainless steel 304 rich Cr content. Inconel 600 performed the second best in eutectic salts, possibly due to its chromium content as well. Nickel came in third with low resistance to eutectic salt. In the composite salt, according to the $R_p$, the $i_{corr}$ and the P values, Nickel ranked exceptionally high possibly due to the formation of a composite nickel oxide cerium gadolinium oxide (NiO-CGO) film on the surface of the nickel electrode. Inconel 600 ranked second, followed by stainless steel. Temperature also played a significant role in contributing to the acceleration of corrosion. As temperature decreased, the resistance of stainless steel 304 to corrosion increase in the eutectic salt. However, for Inconel 600, at higher temperatures resistance to corrosion was high. The corrosion mechanisms based on EIS results using equivalent circuits revealed that the corrosion for the metal structural materials in the salts includes oxide layer formation, and various oxide layers formation with diffusion control and electron transfer.

## Acknowledgements

I would like to acknowledge Dr. Haiyan Zhao, my major professor, for all her support and encouragement in such an undertaking. I would also like to acknowledge my committee members, the faculty and staff here at University of Idaho for all their support, Idaho National Laboratory for the available funding to run this project, and The Center for Advanced Energy Studies for providing the research laboratory in which the experiments were performed. Work supported through the INL Laboratory Directed Research & Development (LDRD) Program under DOE Idaho Operations Office Contract DE-AC07-05ID14517.

## Dedication

I would love to thank my wife Dora for all her support and love and my kids Mikhael-Eugene and Mykhie-Elaine for constantly rooting for their dad. I would like to thank Amey Shigrekar for putting up with me as his cubicle mate and for the inputs he shared with me, as well as Winfred Sowah.

# Table of Contents

## List of Tables

## List of Figures

# Chapter 1: Introduction

## 1.1. Research Challenges and Motivation

The high operating temperature of Molten Carbonate Fuel Cell (MCFC) enables enough conductivity of the carbonate electrolyte, but it places severe demands on the corrosion stability and life span of cell components concerning the corrosivity and volatility of molten carbonate at 650 ºC. On the cathode end, the separators are exposed to highly oxidizing environment, and, after reaction with the thin, creeping electrolyte resulted from evaporation, they form a multi-layered corrosion scale [1,2]. Stainless steel 304, Nickel and Inconel 600 are of interest to researchers due to their appreciable corrosion resistive natures, and have been used as construction for nuclear power production [1] [2], fuel cells [3] [4], and battery components [5]. In the case of fuel cell applications, these materials require introduction into molten salt electrolytes. However, these electrolytes react differently with stainless steel 304, Nickel and Inconel 600 and prompt different corrosion rates. One such electrolyte is molten carbonate salt. Its stability at high temperature, high thermal conductivity, and specific heat capacity has sparked interest among researchers in pursuing it as a suitable form for heat transfer purposes [6]. A great amount of research [7] [8] have been channeled towards understanding the corrosion mechanisms in alloys and stainless steel. Temperature [9] [10], melt composition, alloy composition [11] [12], and gas environment [13] have been some of the areas of research focus. Furthermore, composite salts such as GDC have been suggested as an option for molten salt electrolyte in midrange temperature due to its improved conductivity at moderate temperature, which leads to less corrosion and challenges for operation [14].

Understanding how stainless steel 304, Nickel, and Inconel 600 react in theses salts with varying temperature of the salt is key to this research. Corrosion is an electrochemical process that involves the transfer electrons. Due to its electrochemical nature, corrosion kinetics and mechanism can be studied using electrochemical methods [15][15]. The corrosion kinetics that takes place on the surface of a metal in a specific system can be very complex or complicating. However, when studied with electrochemical methods, the complexity of these kinetics is made simpler [15] . Electrochemical methods such as linear polarization resistance (LPR), Tafel analysis, and electrochemical impedance spectroscopy (EIS) are the most popular ones used in corrosion analysis [16] [17] [11] [18] [19] [20].

### 1.2. Research Objectives and Tasks

The objective of this project is to prove the suitability of stainless steel, nickel and Inconel 600 in eutectic carbonate salt and GDC composite salts using electrochemical methods.

### 1.3. Research Scope

This study will focus on employing the LPR technique, Tafel analysis, and EIS to obtain the electric and electrochemical properties for stainless steel 304, Nickel and Inconel 600 in the eutectic salt and composite salts at the temperature range from 500 ºC to 600 ºC.

# Chapter 2: Literature Review

## 2.1 Comparative review

Compared to other methods such as transmission electron microscopy and scanning electron microscopy, electrochemical methods are nondestructive, and provides information about the intrinsic properties of the electrode of interest under operational conditions [21] [22]. Experimental measurements are faster as samples do not need to be tested after the experiment is complete, but rather can be done in situ.

## 2.2 Systematic review

LPR is a nondestructive electrochemical method that aids in determining the corrosion rate of a sample. It is a direct current (dc) corrosion method which provides information on the resistance polarization ($R_p$) based on an applied potential [23]. Before each run of an experiment, the OCP (potential of an electrode before polarization, which corresponds to the to the corrosion potential when the system is stationary) of the working electrode (CE) needs to be identified versus some reference electrode. The counter electrode (CE) pushes the potential of the electrode towards cathodic values. However, polarizing the WE in the anodic direction; by applying a potential allows the WE to get excited in the neighborhood of the corrosion potential within a potential range of $\Delta E = E - E_{corr}$. The $R_p$ is defined as

$$R_p = \left(\frac{\delta \Delta E}{\delta i}\right)_{i=0, dE/dt \to 0} \quad (1)$$

The equation above suggests that $R_p$ is the slope of a potential versus current density line at OCP, where the rate of the potential is almost zero, and at the point of zero current density [23]. Figure 2.1 illustrates the basic composition of a $R_p$ plot.

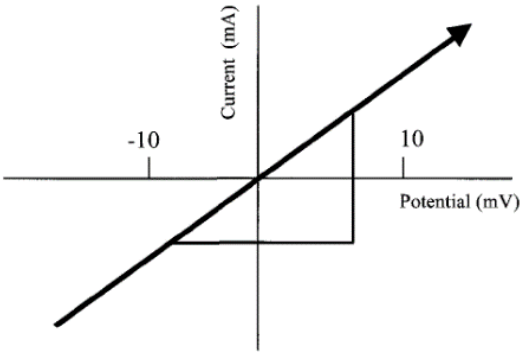


Figure 2.1. Resistance polarization plot. $R_p$ is the slope of the line between -10 mV to 10 mV.

Kuril et al. [23], employed the use LPR to evaluate the corrosion rate of five samples of stainless steel in a concrete pore solution with varying pH and chloride content. They reported that for martensitic stainless steel (FeCr12), the curved part of the plot positioned in the negative part of the plot with respect to the OCP was not linear. Employing the definition of $R_p$ stated above, Kuril et al. applied the zero current rule. However, they found out that $R_p$ did not correspond with the OCP but its corresponding potential was shifted cathodically. In order to combat this, they resorted to reducing the scan rate. However, Kuril et al. noticed that as the scan rate decreased, the shift from OCP reduced, and the zero current point slightly moved away from the nonlinear region. Further test was done, and it was found that using the zero current rule was not always a reliable way of finding the resistance polarization, as such a method did not distinguish between corrosion in passivity or activity. Furthermore, in order to calculate the corrosion rate in the form of corrosion current density, the $R_p$ has to be used in conjunction with the Tafel slopes.

Tafel analysis is also a dc method [24]. Unlike LPR, Tafel analysis incorporates the use of larger potentials. This allows for more measurable currents, results in a nonlinear current-potential relationship, and is modeled using a semi-log plot. This plot is known as the Tafel plot. The Tafel plot consists of an anodic and cathodic curve (see Figure 2.2). The anodic and cathodic curves simulate oxidation and reduction reactions respectively. A linear region is visible on both curves and extrapolating this region to the OCP results in the Tafel coefficients. The draw back to using the Tafel analysis is that large potentials can facilitate unwanted reactions which affects the linear region of the anodic and cathodic curve. When this happens, the values of the anodic and cathodic slope are inaccurate, and the surface of the electrode is altered [24]. Figure 2.3 shows the various kinetics that can be deduced from a Tafel plot; such an active reaction, a passive reaction, a spontaneous reaction and a transpassive reaction.

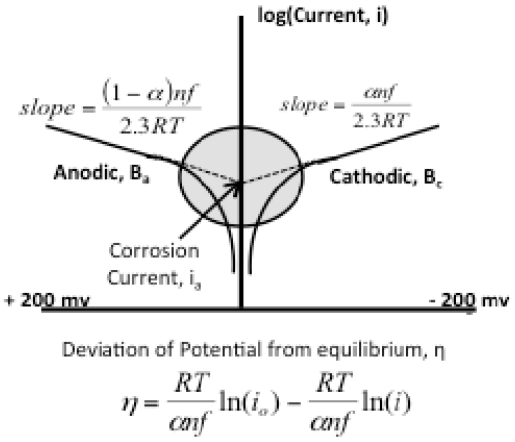


Figure 2.2. A pictorial explanation of different types of kinetics that can be described using Tafel analysis.

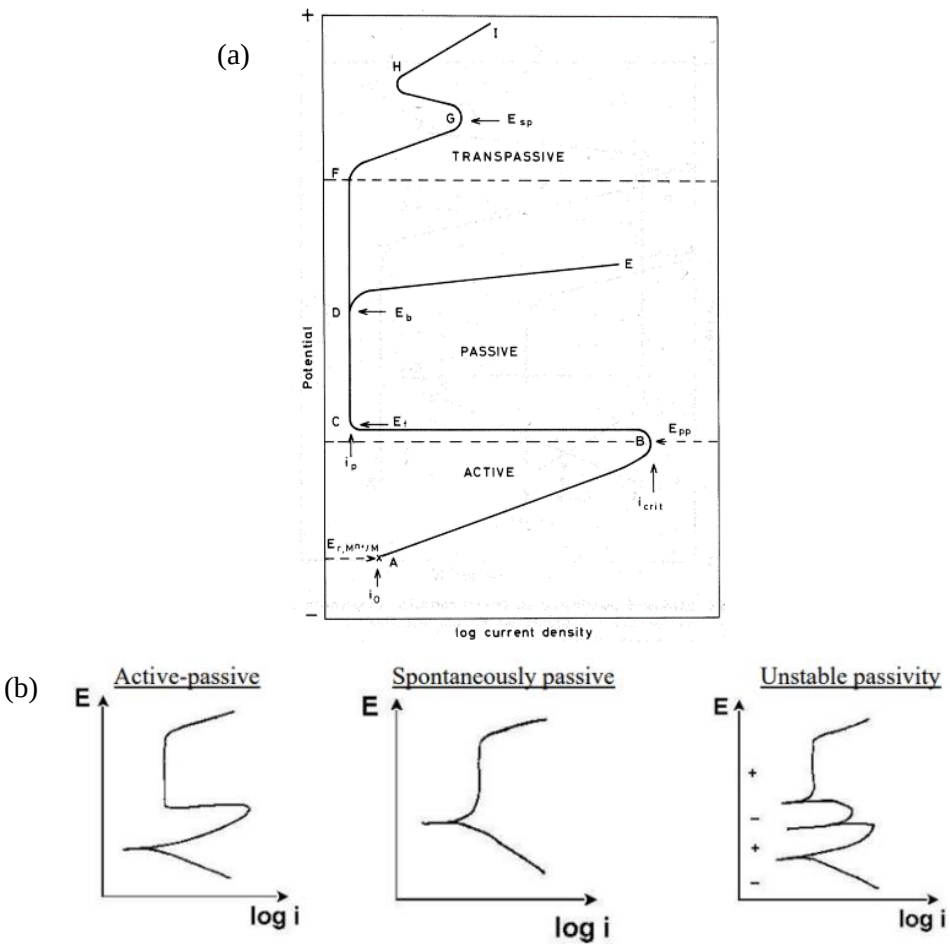


Figure 2.3. (a) Schematic anodic curve for a metal that shows passive ebehavior [25]. (b) Different forms of passivation

With calculated $R_p$, $b_a$ and $b_c$, the corrosion density ($i_{corr}$) can be calculated using Stern-Geary equation (equation 2), and the corrosion rate (CR) can be calculated using equation 3.

$$i_{corr} = \frac{b_a b_c}{2.303(b_a + b_c)R_p} \quad (1)$$

where $b_a$ and $b_c$ are the Tafel slopes of the anodic and cathodic reaction, respectively. $R_p$ was obtained from the LPR measurement

$$CR = \frac{i_{corr} K * EW}{\rho A} \quad (2)$$

where $i_{corr}$ is the corrosion current in ampere.cm$^{-2}$, K is a constant that defines the unit for the corrosion rate and has a value of K 327.2 (mm/(A-mm-yr)) [26], *EW* is the equivalent weight in grams/equivalent, $\rho$ is the density of the material, and A is the electrode surface area in mm$^2$ immersed in the salt.

Sarvghad et al. [16] employed the use of Tafel analysis in analyzing the corrosion of steel alloys in eutectic NaCl+$Na_2CO_3$ at 700 °C and $Li_2CO_3$+$K_2CO_3$+$Na_2CO_3$ at 450 °C. From their experiment, they were able to calculate $i_{corr}$ values, $b_a$ and absolute $b_c$. They reported that samples with the highest $i_{corr}$ had faster anodic and cathodic rates. They further report that the reason why $i_{corr}$ for CS1008, type of stainless steel alloy, in the carbonate salt (85.2 μA cm$^{-2}$) is much lower than in the chloride salt (1686.5 μA cm$^{-2}$) could be as a result of a mechanism change between both salts. They corroborate this claim with the fact that at lower temperatures, molten carbonate salt is less aggressive. Furthermore, in a paper published by Xie et al. [19] on the corrosion behavior of stainless steel in highly concentrated chloride salts they employ the abilities of the Tafel plot to understand their system They report significant current density spikes in the passivation region or on the anodic curve and attribute them to the formation of metastable pit occurring as a result of a cycle of formation and passivation of micro pits. LPR and Tafel are faster ways of understanding the mechanisms that take place in corrosive systems, however, they do not provide in depth information as does EIS.

EIS is an electrochemical method that is popularly used to study corrosion of a WE [27]. It is a nondestructive method, meaning it does not severely deteriorate the surface of the WE. EIS employs the use of frequency and low amplitude sinusoidal voltage wave to perturb a WE. The current response as a result of the applied frequency or voltage is used to determine the corrosion rate. Instruments such as potentiostats with frequency analyzers, are used to measure the impedance

of the system. And this information is displayed on a Nyquist plot (impedance plot) and a Bode plot (an impedance-frequency-phase angle plot) [27]. The purpose of EIS is to analyze the resistance and capacitance values and create a model that explains the phenomena that takes place at the surface of the electrode. Thus, EIS gives more details about the intrinsic properties of the corrosion taking place; allowing for a more in depth study of corrosion mechanisms. Due to the capability of EIS to produce high precision results, it is used to analyze charge transfer parameters of the double layer. Also due to its precision, $R_p$ from the EIS method is more accurate than the polarization methods [27]. Table 2.1gives information about the types of circuit elements used to construct an equivalent circuit. Figure 2.4 sheds more light into what happens when an electrode is immersed in an electrolyte

Table 2.1. Elements within an equivalent circuit [28]

| Equivalent Element | Admittance | Impedance |
|---|---|---|
| R | 1/R | R |
| C | jωC | 1/jωC |
| L | 1/jωL | jωL |
| W (infinite Warburg) | $Y_0\sqrt{(j\omega)}$ | $1/Y_0\sqrt{(j\omega)}$ |
| O (finite Warburg) | $Y_0\sqrt{(j\omega)}Coth(B\sqrt{(j\omega)})$ | $Tanh(B\sqrt{(j\omega)})/Y_0\sqrt{(j\omega)}$ |
| Q (CPE) | $Y_0(j\omega)^a$ | $1/Y_0(j\omega)^a$ |

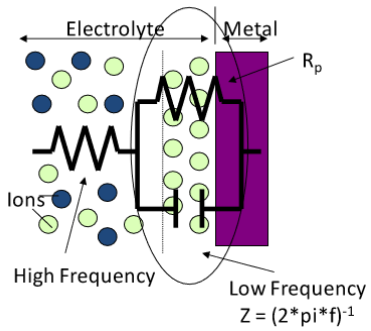


Figure 2.4. Equivalent circuit modeling of the corrosion kinetics of an electrode.

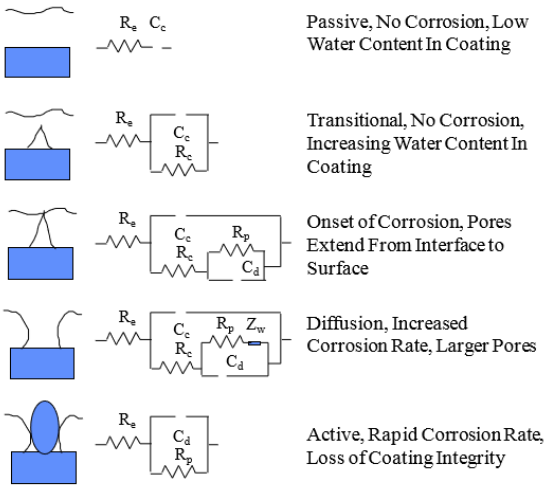


Figure 2.5. Different electrochemical circuits for different stages of degradation of paint coating.

Using EIS, Zeng et al. proposed four theoretical models for molten salt; non active metal, active metal with a porous scale, active metal with a protective scale, and localized attacks. (Figure 2.6 and Figure 2.7). These models take into account various forms of corrosion that take place when a metal is introduced into molten salt. Due to the chemical stability of different metals when introduced to molten salt, the metals can be grouped into two categories; i.e. active and non-active. Active metals are metals that have high enough activation to react with their surroundings, and as such are not chemically stable, thus, creating a protective layer on its surface to prevent corrosion. An example of an active layer is $Ni_3Al$ in molten salt. Non active metals on the other hand, have high chemical stability in their surroundings, example platinum in molten salt system [29].

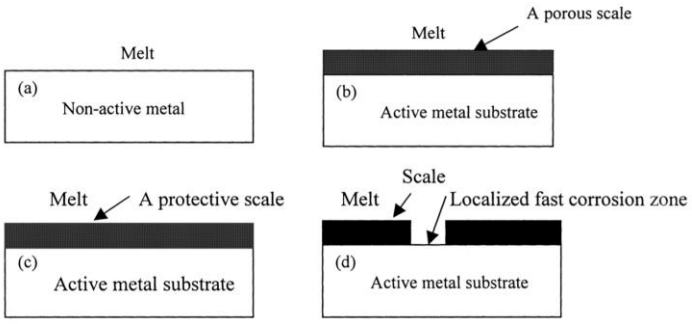


Figure 2.6. Different corrosion phenomenon in molten salt [29].

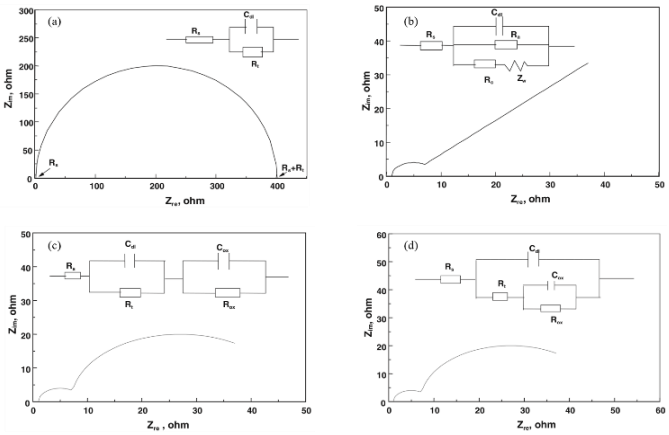


Figure 2.7. Equivalent models for (a) non-active (b) active metal porous scale (c) active metal protective scale and (d) active metal localized corrosion [29].

Conducting their experiment using $Ni_3Al$ in molten $(Li,Na,K)_2SO_4$ at 700 °C, Zeng et al. reported a drop in free potential of $Ni_3Al$ to -900 mV. There was a slight drop from -900 mV over an extended period of time indicating steady corrosion. With a Nyquist plot showing a small semicircle at high frequency and a line at low frequency, they predict a diffusion controlled reaction and not rate limiting because charge transfer at the scale/melt interface can easily occur. At low frequency, there was an emergence of a Warburg resistance which could indicate that the alloy suffered from fast corrosion due to the formation of a non-protective layer. This was confirmed using XRD, and SEM coupled with EDAX, and this revealed the formation of a non-protective layer. This was modeled using the active metal porous scale model, which is an equivalent circuit of a resistor (solution resistance) in series with a parallel combination of a two resistor (representing anodic and cathodic charge), a double layer capacitor, and a Warburg resistor (considering dispersion effect).

Zeng et al. further tested platinum in molten $(Li, K)_2CO_3$ at 650 °C in air. The Nyquist plot showed a larger semicircle at high frequency. The loop was related to the impedance of the charge transfer at the platinum/ molten salt interface. This was fitted using the model for non-active metals which is a circuit of a resistor; representing the solution resistance in series with a parallel combination of a capacitor (double layer capacitance) and a resistor (charge transfer). They also found out that the rate limiting process in the melt was the electrochemical charge transfer of the porous scale model.

Lastly, Zeng at al. tested FeAl in molten $(Li, K)_2CO_3$ at 650 °C for 5 and 48 hours. Two impedance plots were generated for the initial and later stage. This was attributed to the change of oxide layer growth. The initial stage displayed diffusion-controlled reaction while the later stages of the experiment (> 20 hours of immersion) displayed two capacitance loops indicating that gradual

formation of a protective layer containing $LiFeO_2$ (external layer) and $Al_2O_3$ (internal layer). At later immersion times, corrosion was enhanced by transportation of ions in the scale and not diffusion of oxidants in the salt. Zeng et al. concluded that for a porous scale or oxide layer, an equivalent circuit of a double layer capacitance in series with oxide capacitance can be used to describe it [29].

Fernandez et al. studied the corrosion of rate of stainless steel 304, T22 steel and OC -4 steel (a type of alumina-forming austenitic steel) in $NaNO_3/KNO_3$ (60:40 ratio) and 390 °C at 2, 8,24,72,150, 240 and 340 hours. The impedance diagram displayed two capacitance loops for stainless steel 304 and OC-4 steel. This was modeled using an equivalent circuit that modeled the presence of a protective layer as discussed by Zeng et al. The first loop at high frequency was attributed to interactions between the metal and the salt. The second loop at low frequency was attributed the process controlled by the transport of ions in the scale. Fernandez et al. went on to further state that because corrosion is controlled by the transport of ions in the scale, the radius of the second loop at lower frequency is higher than the radius of the first loop at higher frequency. However, OC-4 performed better in the $NaNO_3/KNO_3$ salt compared to stainless steel 304 and T22 steel due to to its Al-Cr rich layer. [30].

Zeng and Li also conducted some EIS studies on Ni-based super alloy M38G in molten (0.9Na, $0.1K)_2SO_4$ induced hot corrosion [31]. It was observed that the impedance spectrum was composed of a small semi-circle at high frequency and a large semicircle at low frequency. However, this was not shown clearly on the phase angle versus log(f) which displayed only one loop at low frequency. Zeng and Li go on to say that the fused alloy can form a protective layer during corrosion. The two capacitive loops can be represented by a double layer capacitor at high frequency in series with an oxide capacitance at low frequency. Considering dispersion effect Zeng and Li modeled the double year capacitance and the oxide capacitance with a constant phase element during the fitting process. The fitting values on the fused alloy do not undergo clear changes with exposure time. However, for the first three values, there is a trend on the first three values, which indicated a steady corrosion rate. Zeng and Li reported that the deviation of $n_{dl}$ and $n_{ox}$ from 1 shows the presence of dispersion effect, a notable feature for molten salt. The irregular change of $R_{ox}$ for the fused alloy, according to Zeng and Li indicate dissolution of the oxide layer on the surface of the alloy. They conclude that the presence of the fused alloy in $(Na,K)_2SO_4$ alloys oxygen to easily reach the surface of the alloy and thus contribute to the formation of the oxide layer, so that the corrosion rate of the alloy is the controlled by ion transfer in the scale.

Frangini et al. conducted a corrosion analysis on 13-Cr ferritic stainless steel protected by a perovskite conversion treatment. They studied the relation between the coating microstructure and formation mechanism. The analysis comes as a result of the growing interest to produce materials that are more corrosion resistant in molten salt fuel cells. The employed the use of La-based perovskite and prepared their coupons by coating the stainless steel coupons in 53 mol% $Li_2CO_3$ + 47 mol% $Na_2CO_3$ with 2 mol% of $La_2CO_3$. The coated coupons were placed in 62 mol% $Li_2CO_3$ + 38 mol% $K_2CO_3$ and slowly heated to 650 °C. Electrochemical techniques used to analyze the efficiency of corrosion protection by the perovskite were open circuit potential evaluation, anodic polarization at a scan rate of 1 mV/s and alternate current impedance at a frequency range of 10 kHz to 10 mHz, and a voltage amplitude of 5mV. Corrosion results for the coated sample shows a very quick shift of OCP to noble potential and remaining at steady state within a few hours, and higher than that of the uncoated surface by 0.8 V. Proving that passive layer formed on the coated sample remained stable over a long period of time. The polarization curves of the uncoated surface show no active to passive transition, which the authors attributed to a surface conversion process. The impedance plot of the coated alloys remains unchanged over a long period of time. Also, it shows the presence of a Warburg element at intermediate frequency with a 45° slope which the authors attribute to the limiting transport of ion across the oxide layer. The rise in steepness of the slope as frequency drops, could be attributed to the finite length effects or bounded diffusion. On the contrary, the depress arc seen on the impedance plot for the uncoated surface, represents a charge transfer reaction or a reaction-controlled process. The high values of the oxide resistance of the coated surface. Frangini et al. concluded that the perovskite along with the initial formed $LiFeO_2$ layer provides excellent shielding from the molten salt [32].

Also, Wu et al. reported that. the operation of direct carbon fuel cells (DCFC) require high temperature between 700 °C to 900 °C. At high temperatures, materials degrade faster, parts become expensive and output efficiency reduces as a result of the gasification of solid carbon to form carbon monoxide. A great approach is to reduce the operating temperature of the cells. One way to do this is to develop a faster ionic conductor by coming up with an electrolyte that is a mixture of molten carbonate or hydroxide and oxygen ion conductors at low temperatures. A promising oxygen ion conductor which can be mixed with molten carbonate is gadolinium doped ceria (GDC) [14] also known as gadolinium dopes cerium oxide (Gd:CeO2). A lot of effort have been put into the research of GDC [33] [34] [35] [36] and its ability to be used to conduct midrange temperature experiments, including understanding its thermal structures and morphology (a challenge involving the commercialization of solid oxide fuel cells) (400-700°C ) but less has been researched into corrosion mechanisms involving GDC.

However, there is finite information regarding research studying the kinetics and mechanisms of stainless steel in molten salt 304, nickel and Inconel 600 whiles varying the temperature and with the electrode in the salt eutectic carbonate and composite salt. This study would allow for the variation of temperature while an electrode is immersed in the salt and a correlation between temperature and oxide layer formation in both eutectic and composite GDC salts using the electrochemical methods of linear polarization resistance (LPR), Tafel analysis, and electrochemical impedance spectroscopy (EIS).

# Chapter 3: Experimental Methodology and Analysis

A lot has been done with analyzing sample over a long period of time and at only one temperature. What happens when the sample is kept in the salt and the temperature is changed? Bringing this knowledge to the table would be beneficial to researchers.

## 3.1. Materials and Setup

A three electrode system was used for the impedance measurements. The working electrode (WE) was stainless steel 304 (see Table 3.1 for chemical composition), nickel, and Inconel 600 (see Table 3.1 for chemical composition) for their respective experiments. The counter electrode (CE) was glassy carbon, and the reference electrode (RE) was Ni/NiO. 0.635mm diameter stainless steel 304, 0.5mm diameter nickel wire, 1.041 mm, and 3.175 mm diameter glassy carbon rod were cut to appropriate lengths. The Ni/NiO electrode was prepared by inserting fine powdered NiO into an MgO tube with a diameter of 6.25 mm. The powder was filled to an appropriate height in the tube to make sure that it stayed submerged in the molten salt whiles in the tube. The already cut Ni was inserted into the MgO tube. The electrodes were each placed in MgO tubes to allow them to be bundled up together using a piece of steel wire. A glassy carbon crucible was used to contain 25 grams of $0.67Li_2CO_3$-$0.33K_2CO_3$ (a mole ratio of 2:1), for the eutectic carbonate experiment, and 25 grams of composite salt comprising of gadolinium doped ceria (GDC) and $0.67Li_2CO_3$-$0.33K_2CO_3$. The experimental apparatus used in the experiment is shown in Figure 3.1. The electrochemical measurements were controlled by Princeton Applied Research, versaSTAT 4 potentiostat, and a VersaStudio software was used for data acquisition.

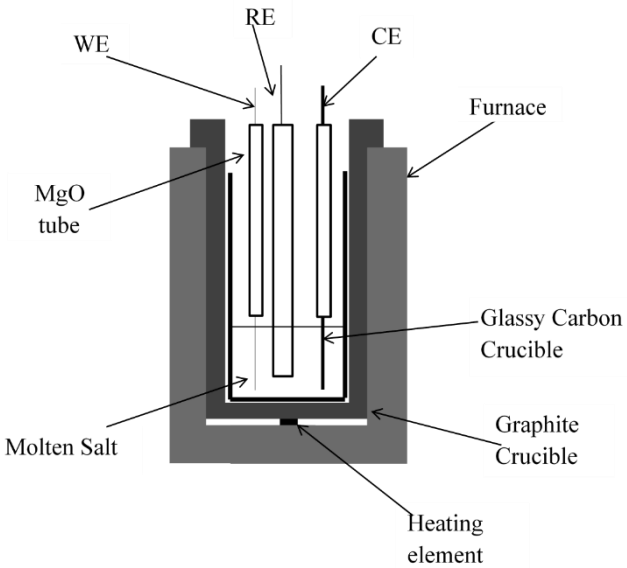


Figure 3.1. Electrochemical cell for studying the corrosion of stainless steel 304, nickel, and Inconel 600, at various temperatures in eutectic $0.67Li_2CO_3$-$0.33K_2CO_3$ and carbonate-GDC composite salt, in air.

Table 3.1. Chemical composition of stainless steel 304 and Inconel 600

| Stainless Steel 304 | C | Mn | Cr | Ni | Mo | Cu | Si | Nb | S | Fe | Cu |
|---|---|---|---|---|---|---|---|---|---|---|---|
| | 0.08 | 1.54 | 18.47 | 8.30 | 0.30 | 0.37 | 0.48 | 0.027 | 0.006 | Bal. | n/a |
| Inconel 600 | 0.15 max | 1.00 max | 14.0-17.0 | 72.00 min | n/a | n/a | 0.50 max | n/a | 0.015 max | 6.0-10.0 | 0.50 max |

### 3.2. Parametric study for reliable measurements and results

There is clear information on what are the proper values for the electrochemical measurements including the step time and step height, which are essential to determine the scan rates. Thus, a various value was tested to decide the proper scanning rate number that should be used for the electrochemical measurements.

#### 3.2.1. Linear Polarization Resistance

The final and initial potential was set at -20 mV and 20 mV versus open circuit potential respectively. The parameters, the step height (SH) and step time (ST) was varied between 0.1 mV to 0.4 mV, and 0.1 s to 0.4 s, respectively. The data was exported from versaStat4 and plotted in Microsoft excel (see Figure 4.1). A line was fitted at the region where the current is zero, also known as the open circuit potential, to avoid potential loading on the sample [37]. The polarization resistance ($R_p$) was calculated using VersaStudio 4 and is listed in Table 4.1 for each run. The parametric test was conducted only on the stainless steel 304, with an electrode diameter of 0.635mm and immersion depth in the salt of 32.2 mm and an immersion surface area of 64 $mm^2$.

#### 3.2.2. Tafel Plots

The final and initial potential was set at -250 mV and 250 mV versus open circuit potential respectively for Tafel measurements at different SHs and STs as shown in Table 4.2. The data was exported and plotted in Microsoft excel (Figure 4.3). The Tafel plot was fitted using VersaStudio and the obtained parameters cathodic beta ($b_c$) and anodic beta ($b_a$) constants are tabulated in Table 4.2. With calculated $R_p$, $b_a$ and $b_c$, the corrosion density ($i_{corr}$) can be calculated using Stern-Geary equation (Equation 2), and the corrosion rate (CR) using in Equation 3. The related corrosion rate constants for CR calculation are listed in Table 3.2

Table 3.2. Corrosion rate constants for calculating corrosion rates in mm/yr and milli-inches/yr [38]

| Units for corrosion rate | K | Units |
|---|---|---|
| mm/year | 3272 | mm/(A-cm-year) |
| milli-inches/year (mpy) | $1.288 \times 10^5$ | milli-inches /(A-cm-year) |

### 3.3. Electrochemical Measurements (Non-Parametric Study)

The linear resistance polarization (LPR) measurements were carried out using an initial potential of -20 mV and a final potential of 20 mV versus open circuit potential (OCP). The parameters, step height (SH) and step time (ST) were set at 0.1 mV and 0.1 s respectively. The Tafel curve measurements were carried out using an initial potential of -250 mV and a final potential of 250 mV versus open circuit potential. The SH and ST were set to 0.1 mV and 0.1s respectively. Fitting for the Tafel plot was done using VersaStudio and the obtained parameters include the cathodic beta ($b_c$) and anodic beta ($b_a$) constants. With calculated $R_p$, $b_a$ and $b_c$, the corrosion density ($i_{corr}$) can be calculated using Stern-Geary equation (Equation 2), and the corrosion rate (CR) can be calculated using Equation 3. Knowing the immersions depth and diameter of the electrode aloows one to calculate the immersion surface area which was 61.38 $mm^2$ for stainless steel 304, 52.42 $mm^2$ for nickel, and 100.24 $mm^2$ for Inconel 600 in the eutectic salt. For the composite salt, stainless steel 304 had an immersion surface area of 54.5 $mm^2$, nickel had an immersion depth of 52.05 $mm^2$, and Inconel 600 had an immersion depth of 100.4 $mm^2$.

EIS measurements were carried out between 0.01 Hz and 100,000 Hz and analyzed using a disturbance sinusoidal voltage with a signal of 10 mV amplitude (rms). Replicate test runs were done to ensure consistency in the data. The data recorded was the real and imaginary impedance, and the frequency. From these parameters, the Nyquist plot (real vs imaginary impedance) and the Bode plots (frequency versus phase angle, and frequency versus magnitude of impedance) can be created. The EIS data were fitted in Zview, an advanced software for electrochemical research and development. The Nyquist and Bode plots were the plots of interest during the fitting process. The fitting process first consisted of using the instant fit method Zview provides and then using the initial values from the instant fit as a starting point to design appropriate equivalent circuits.

# Chapter 4: Results and Discussion

## 4.1. Parametric Study

### 4.1.1. Linear Polarization Resistance

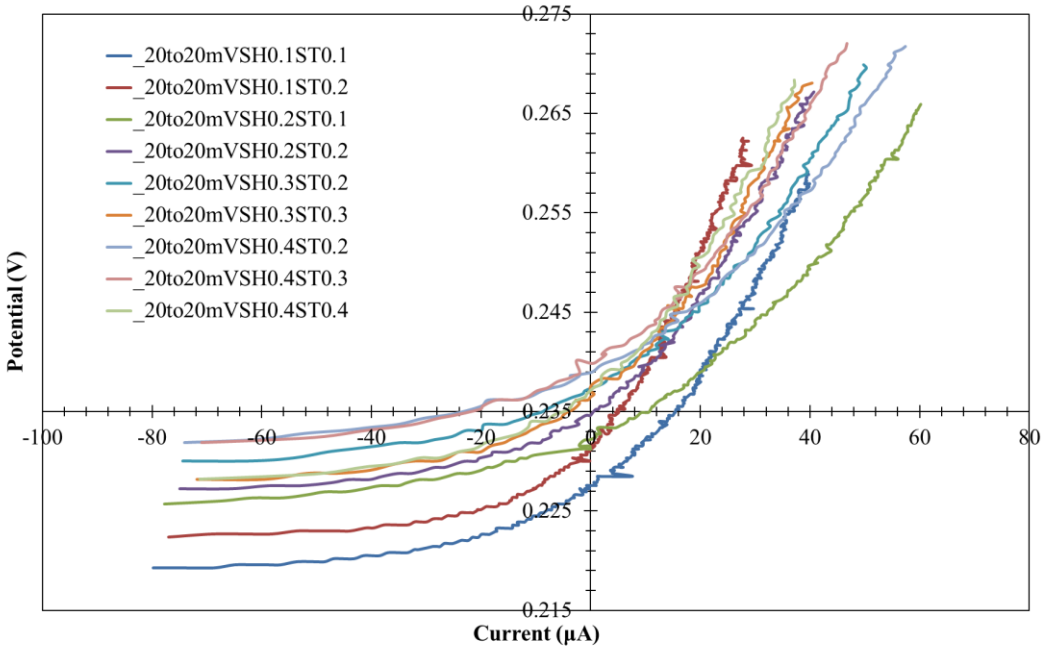


Figure 4.1. Parametric study of stainless steel 304 with surface area of 64.2 $mm^2$ in eutectic $Li_2CO_3$-$K_2CO_3$ salt at 600 ˚C employing the use of linear polarization measurements at various scan heights and scan times, to determine the polarization resistance.

The linear polarization resistances for stainless steel 304 in $Li_2CO_3$-$K_2CO_3$ salt at 600 ˚C for were measured at various scanning height from 0.1 ~ 0.4 mV and scanning time from 0.1 to 0.4 s (see Figure 4.1). Accordingly, the scanning rates are between 0.5 to 2.0 mV/s. The $R_p$ determined by the linear polarization methods varied between 160 ohms to 250 ohms (Table 4.1). The $R_p$ values increased as the scanning rate decreased (Figure 4.2). This can be attributed to the fact that at larger step heights and times, sufficient time is not allowed for the system to stabilize at each potential [39].

Table 4.1. Polarization resistance ($R_p$) for stainless steel 304 with surface area of 64.2 $mm^2$ after parametric analysis at different step heights and step time in eutectic $Li_2CO_3$-$K_2CO_3$ salt at 600 ˚C

| Step Height (mV) | Step Time (s) | Scan rate (mV/s) | Rp (ohms.$cm^2$) |
|---|---|---|---|
| 0.1 | 0.1 | 1.00 | 248.3 |
| 0.1 | 0.2 | 0.50 | 336.5 |
| 0.2 | 0.1 | 2.00 | 186.4 |
| 0.2 | 0.2 | 1.00 | 253.0 |
| 0.3 | 0.2 | 1.50 | 195.4 |
| 0.3 | 0.3 | 1.00 | 254.2 |
| 0.4 | 0.2 | 2.00 | 159.9 |
| 0.4 | 0.3 | 1.33 | 211.4 |
| 0.4 | 0.4 | 1.00 | 280.2 |

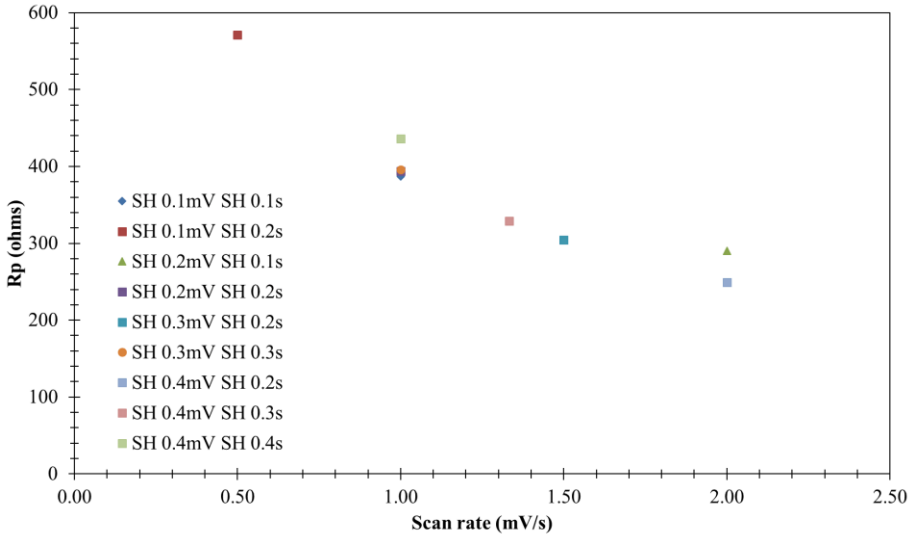


Figure 4.2. Scan rate versus the resistance polarization for various steps heights and times for stainless steel 304 in $Li_2CO_3$-$K_2CO_3$ salt at 600 ˚C after the parametric study.

### 4.1.2. Tafel measurements

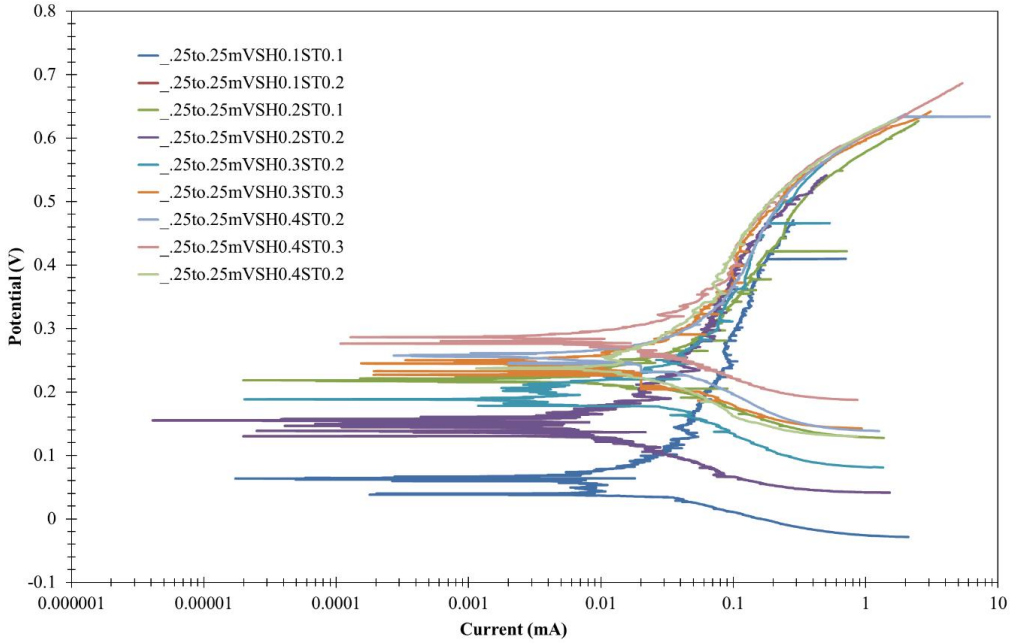


Figure 4.3. Tafel measurements at various step heights and step time for stainless steel 304 in $Li_2CO3$-$K_2CO_3$ salt at 600 ˚C after parametric analysis, in order to obtain Tafel constants.

The Tafel lines were measured using similar step heights and step times for linear polarization resistances. The corresponding cathodic beta and anodic beta values were evaluated and the $i_{corr}$ was calculated (Table 4.2). There are results obviously off the average range of the results, which are highlighted in red. These results suggesting that the parameters used for measurements were as a result of a not so proper fit. It is seen (Table 4.2) that at for scan rate of 1 mV/s, the values for the current density are generally coherent, thus 1 mV/s is an appropriate scan rate for LPR and Tafel analysis. With the scan rate determined, actual run for the eutectic and composite salts using stainless steel 304, nickel, and Inconel 600 can be conducted.

Table 4.2. Cathodic beta ($b_c$) and anodic beta ($b_a$) constants from Tafel measurements of stainless steel 304 in $Li_2CO_3$-$K_2CO_3$ salt at 600 ˚C, and corresponding corrosion current density after parametric study.

| Step Height (mV) | Step Time (s) | bc (mV) | ba (mV) | Icorr ($\mu A/cm^2$) |
|---|---|---|---|---|
| 0.1 | 0.1 | 103 | 8.29E+30 | 179 |
| 0.1 | 0.2 | 977 | 6450 | 1005 |
| 0.2 | 0.1 | 64 | 220 | 115 |
| 0.2 | 0.2 | 106 | 266 | 130 |
| 0.3 | 0.2 | 6760 | 989173 | 14920 |
| 0.3 | 0.3 | -1.34E+09 | 4.57E+07 | $8.07 \times 10^8$ |
| 0.4 | 0.2 | 108 | 257 | 206 |
| 0.4 | 0.3 | 3.32E+05 | 2.96E+05 | $3.21 \times 10^6$ |
| 0.4 | 0.4 | 93 | 260 | 106 |

## 4.2. Electrochemical Study in Eutectic Carbonate Salt

### 4.2.1. Electrochemical Study of Stainless Steel 304 in Eutectic salt

#### 4.2.1.2. LPR analysis for stainless steel in eutectic

The true $R_p$ [40] were obtained by calculating the slope from the current-potential plot at the zero current region, and multiplying the result by the immersed surface area of stainless steel at various temperatures (Figure 4.4 and Table 4.3). As the temperature decreased from 600 °C to 502 °C, $R_p$ increased from 182 Ohms.cm$^2$ to 4862 Ohms.cm$^2$, suggesting an increasing resistance of the SS 304 to the salt [20]. The OCP values shifted from cathodic (more negative) values at 600 °C to more anodic values at 503 °C (Figure 4.4), indicating the formation of an oxide layer at lower temperatures and dissolution of the oxide layer at higher temperatures [41]. Choudhary et al. also studied the relationship between OCP and $R_p$ [42]. They reported that as OCP increased, $R_p$ also increased, and was proportional to the different phases of rust constituents on the electrode surface. The increase in OCP and $R_p$ simultaneously, indicated a growing oxide layer on the metal surface [42]. However, the shift in OCP is significant from 600 °C to 577 °C and consistent from 551 °C to 503 °C, suggesting an indication of a steady corrosion. A trend can be seen for the OCP and $R_p$. Generally, as $R_p$ increased OCP increased as well as seen in Figure 4.5.

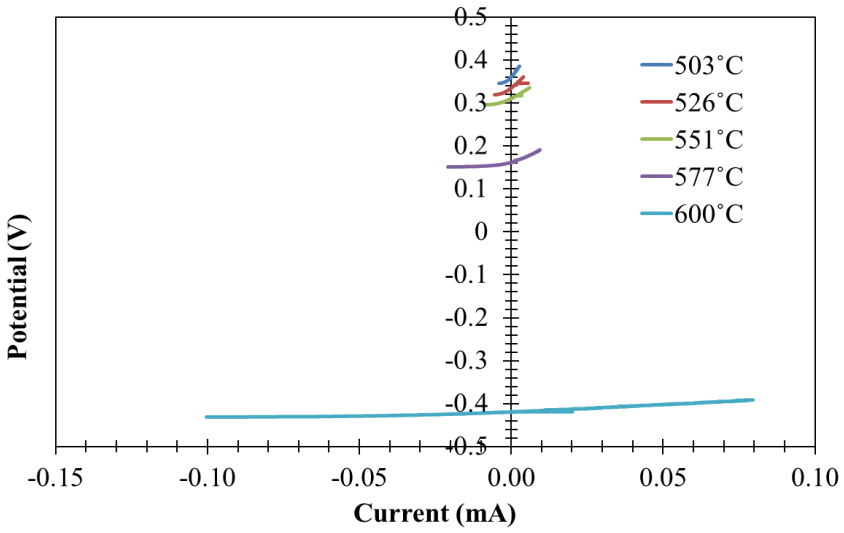


Figure 4.4. LPR measurements for stainless steel 304 conducted with a potential range of -20mV to 20mV at various temperatures in $Li_2CO_3$-$K_2CO_3$ salt at several temperatures to determine the polarization resistance.

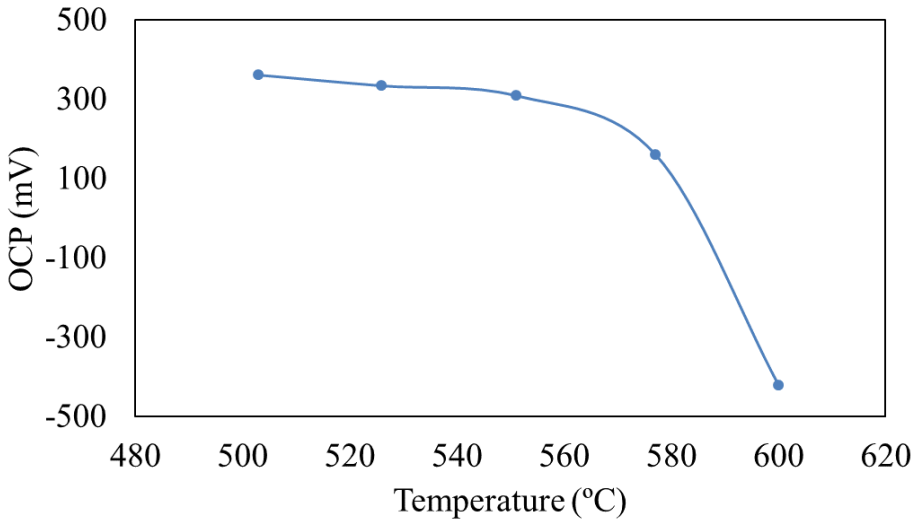


Figure 4.5. Open circuit potential versus temperature trend for stainless steel 304 during LPR measurement run in $Li_2CO_3$-$K_2CO_3$ salt at 503 °C, 526 °C, 551 °C, 577°C and 600 °C.

Table 4.3. Polarization resistance ($R_p$) and open circuit potential for stainless steel 304 with surface area of 61.38 $mm^2$ in $Li_2CO_3$-$K_2CO_3$ salt at 503 °C, 526 °C, 551 °C, 577°C and 600 °C, respectively.

| **Temperature (˚C)** | **Rp (Ω.cm$^2$)** | **OCP (mV)** |
|---|---|---|
| 503 | 4862 | 362 |
| 526 | 3597 | 335 |
| 551 | 2277 | 310 |
| 577 | 964 | 162 |
| 600 | 182 | -420 |

### 4.2.1.2. Tafel analysis for stainless steel in the eutectic salt

Figure 4.6 shows the potentiodynamic polarization curves for stainless steel 304 in $Li_2CO_3$-$K_2CO_3$ at 503 °C, 526 °C, 551 °C, 577°C and 600 °C, respectively. At 600 °C, there is a sharp deviation on the anodic curve from the passivation region at 1 mA. This suggests the formation of a thick oxide layer driven mainly at that point by the potential. Further on, the current range under this section is very minimal compared to the potential rise, hence the suggestion of an increase in

resistance of the metal to corrosion. The oxide layer remains relatively stable as seen by a rise in OCP at 577 °C. Looking closely at the passivation zone at 577 °C, there are little spikes on the anodic curve at approximately 0.01 mA, suggesting a partial breakdown of the oxide layer [19]. This is also indicated by the sudden rise in slope of the anodic curve suggesting further resistance to corrosion. The oxide layer continues to form as there is a rise in OCP at 551 °C. The passivation region at 551 °C experiences some breakdown in oxide layer at 0.01mA indicated by a spike, but not as dramatic as that seen in 577 °C. The slope of the anodic curve is less steep and is an indication of the continuation of corrosion but at a much slower rate. The OCP at 551 °C, 526 °C and 503 °C are very close in proximity which is a strong indication of a stable oxide. As the temperature progresses from 551 °C to 503 °C, the slope of the anodic curves are very similar. At approximately 0.1 mA, the anodic slopes get steeper with rise in temperature, suggesting an increase in resistance of the metal alloy. This is seen shortly after the appearance of spikes at that point. This could indicate the breakdown of the oxide layer, and the immediate formation of an oxide layer, thus corroborating the increase in anodic slope after this point.

The calculated data including are summarized in Table 4.4. From 503 °C to 600 °C, the value of $b_a$ controlled by the oxidation reaction increases from 142 mV to 220 mV, showing that higher temperatures promote anodic reactions. As temperature increases, the anodic reactions are promoted significantly, which suggest that at higher temperatures, corrosion or dissolution rate is accelerated [43].This can be seen from the values of the Tafel slope, $b_a$ in Table 4.4. The OCP potential for stainless steel 304 at 503 °C, 526 °C, 551°C, 577 °C and 600 °C are 309 mV, 306 mV, 300 mV, 61.6 mV and -470.3 mV vs Ni/NiO (Table 5) respectively. The significant shift of OCP, indicated by the tails of the Tafel curves , from more cathodic to anodic values from 600 °C to 502 °C, represent the formation of an oxide layer on the surface of the stainless steel 304 electrode [44] [19]. This could also indicates the improvement of the anodic reaction, the creation of a semi protective film, or the disintegration and passivation of the oxide layers that alternatively occurred on the surface of the stainless steel 304 [19].

The value of $i_{corr}$ at 600 °C is significantly higher than at 557 °C and decreases as temperature decreases. This is an indication of the significant acceleration of the oxidation of stainless steel 304 at higher temperatures as compared to lower temperatures [43]. At 551 °C, 526 °C and 503 °C, the values of $i_{corr}$ are relatively stable, indicating the passivation of the metal and the slowing down of the corrosion of the alloy[19]. It is therefore clear that at higher temperatures, the corrosion of stainless steel 304 is accelerated. Sarvghad et al. conducted a corrosion test for stainless steel 316 (SS 316) in molten chloride sulfate (2.65 NaCl + 73.5 $Na_2SO_4$), chloride carbonate (40 NaCl + 60

$Na_2CO_3$), and ternary carbonate (33.4 $Na_2CO_3$ +32.1 $Li_2CO_3$ + 34.5 $K_2CO_3$) at 700 ˚C for the chloride salts, and 430 ˚C for the ternary salts [45]. They reported a very low $I_{corr}$ of of 6 uA-$cm^{-2}$ for the SS 316 in the ternary salt. The chloride sulfate and carbonate had $I_{corr}$ values of 74 uA/$cm^2$ and 247 uA/$cm^2$ respectively. The almost fourfold increase between the chloride sulfate and carbonate was attributed to the high solubility of Cr and other alloying elements in the molten salt, and the dissolution of the oxide layer into the salt. These values suggest that at higher $I_{corr}$, the solubility of the Cr layer and the breaking down of the oxide layer is more aggressive. Table 4.4 shows a value of 6.7 uA/$cm^2$ for $I_{corr}$ at 503 ˚C, which is close to Sarvghad et al. value of 6uA/$cm^2$ at 450 ˚C. Table 3 also shows a general rise in $I_{corr}$ values as temperature increases. However, a more significant rise is seen at 600 ˚C. This suggests that at high temperatures Cr and other alloying elements are more soluble in the salt and hence the subsequent dissolution of the oxide layer in the salt. This is corroborated by the decreasing $R_p$ values (see Table 4.3) as temperatures increases. At lower temperatures, molten salt becomes less corrosive. As a result of their ionic nature, the interaction of molten salts with metals leads to redox reactions. The corrosion of these metals is highly dependent on the solubility of their oxide layers in the liquid salt. Iron oxides such as FeO, $Fe_2O_3$ and $Fe_3O_4$ formation is the result of interaction between the molten carbonate and steel alloys [45].

Furthermore, as temperature increases, the corrosion rate (Table 4.4) also increases. In other words, the increase in temperature promotes or enhances the corrosion rate of the stainless steel 304 alloy.

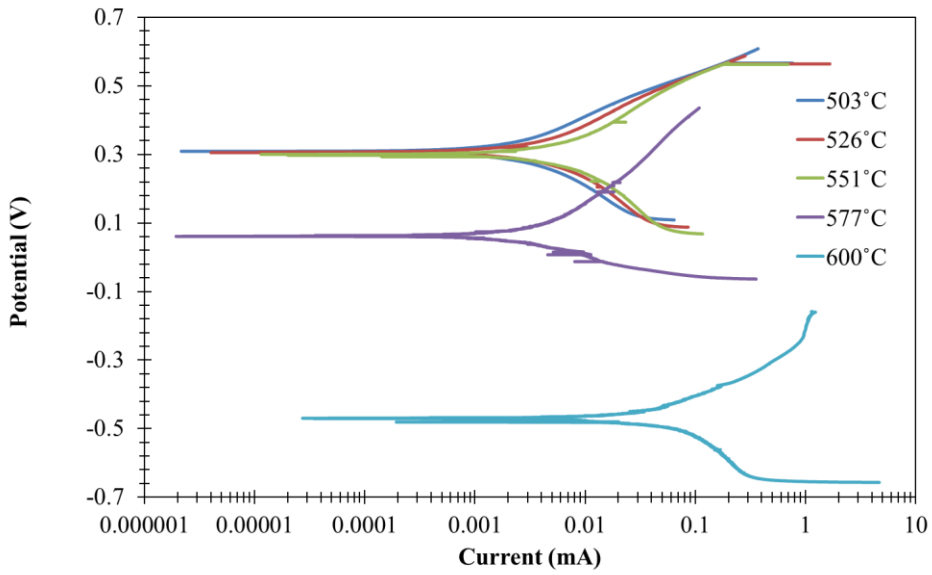


Figure 4.6. Potentiodynamic polarization curves for stainless steel 304 in $Li_2CO_3$-$K_2CO_3$ at 503 °C, 526 °C, 551 °C, 577°C and 600 °C, respectively, conducted at a potential range of -0.25V to 0.25V vs OCP.

Table 4.4. Cathodic beta ($b_c$) and anodic beta ($b_a$) constants from Tafel measurements for stainless steel 304 and calculated corrosion current density ($i_{corr}$) and corrosion rate (CR) for stainless steel using the $R_p$, $b_a$, and $b_c$, in $Li_2CO_3$-$K_2CO_3$ salt at 503 °C, 526 °C, 551 °C, 577°C and 600 °C, respectively.

| **Temperature (˚C)** | ***$b_c$*** **(mV)** | ***$b_a$*** **(mV)** | **OCP (mV)** | **$i_{corr}$ (µA/cm$^2$)** | **CR (mm/yr)** |
|---|---|---|---|---|---|
| 503 | 159 | 142 | 309 | 6.70 | 0.070 |
| 526 | 148 | 146 | 306 | 8.87 | 0.0927 |
| 551 | 266 | 166 | 300 | 19.5 | 0.204 |
| 577 | 94 | 244 | 62 | 30.6 | 0.319 |
| 600 | 295 | 220 | -470 | 300 | 3.14 |

#### 4.2.1.3. EIS measurement and modelling for Stainless Steel 304 in the eutectic salt.

The equivalent circuit models used to fit the EIS data is shown in Figure 4.7. Figure 4.8 to Figure 4.12 display the impedance spectra for 503 °C, 526 °C, 551 °C, 577 °C, and 600 °C. Figure 5a is a Voigts circuit with two time constants (two constant phase elements) in series with an inductor. Figure 5b is a Voigts circuit with two time constants (one constant phase element and one capacitor) in series with an inductor. $R_s$ represents the solution or electrolyte resistance, which happens as a result of the ohmic drop that takes place in the solution, $C_{co}$ is the outer oxide layer capacitance, $R_{co}$ is the resistance of the outer oxide layer, $C_{dl}$ is the double layer capacitance and $R_{ct}$ is the charge resistance, which is the resistance between the transfer of electrons from the solution to the metal, and the transfer of ion from the metal to the solution, and L represent high frequency inductive behavior. Each constant phase element represents a depression on the phase –frequency plot. The double parallel circuits also represent that formation passive films as bilayers on the surface of the stainless steel 304 [46]. A parallel circuit of a resistor is used to model each layer formed on the stainless steel 304 surface, with the resistor representing the conductivity of the film and the capacitor representing the dielectric properties of the  of the film [47] [48]. Figure 14 is a physical representation of the electrode in the molten salt. For corroding systems with frequency dependence and non-ideal capacitive behavior, CPE is used [19] and its impedance representation is given as

$$Z = \frac{1}{T(j\omega)^P} \tag{4}$$

where *T* is a fit parameter. When $P = 1$, the CPE acts as a capacitor with *T* equal to the capacitance. In practice, *P* is less than 1 [19]. Due to microscopic  material properties that can exhibit distribution, CPE behavior arises and the *P* value gives information about the nature of the material surface or the passive layer [19]. The impedance of a capacitor is given by

$$Z = \frac{1}{j\omega C} \tag{5}$$

where *C* is the capacitance. The impedance of the inductance can be represented as

$$Z = j\omega L \tag{6}$$

where *L* is the inductance.

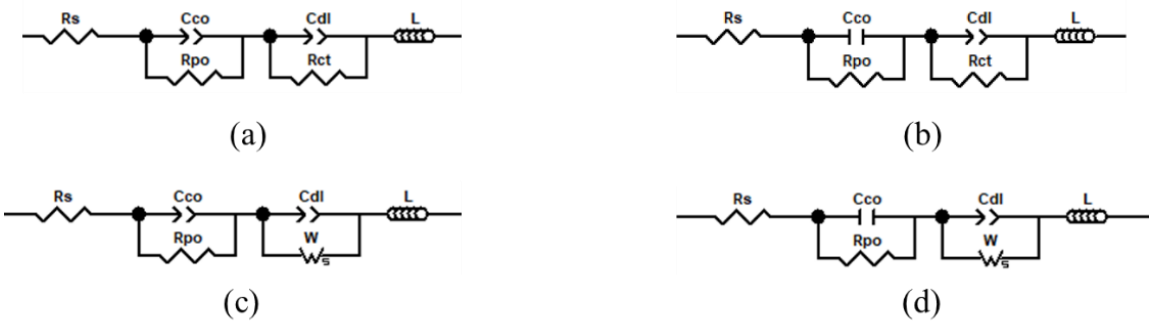


Figure 4.7. Equivalent models with two time constants in series with an inductor for fitting Bode and Nyquist data of stainless steel for 503˚C, 526˚C, 551˚C, 577˚C and 600˚C. (a) Voigts circuit with two constant phase elements (CPE) for fitting503˚C, 526˚C, 551˚C, and 577˚C. (b) Voigts circuit with one constant phase element and a capacitor for fitting 600˚C.

The Total impedance of Figure 5a and b can be expressed as

$$Z_{5a} = R_s + \frac{1}{T_{co}(j\omega)^{Pco}+(1/R_{po})} + \frac{1}{T_{dl}(j\omega)^{Pdl}+(1/R_{ct})} + j\omega L \qquad (7)$$

$$Z_{5b} = R_s + \frac{1}{T_{co}(j\omega)^{Pco}+(1/R_{po})} + \frac{1}{j\omega C+(1/R_{ct})} + j\omega L \quad (8)$$

The values for Figure 4.7a and Figure 4.7b are shown in Table 4.5 and Table 4.6. At low frequency (0.03 Hz ~ 2Hz), there is a depression loop except for 600 °C as well as a high frequency (800 Hz ~ 10kHz) a seen in Figures 9 to 13 on the plot of phase angle (theta vs log(f)). These two depressions represent time constants. Whiles in the salt, the stainless steel 304 forms a porous oxide layer on its surface. The voids of this layer are filled with molten $Li_2CO_3$-$K_2CO_3$ salt. Due to this phenomenon, the two time constants represented by loops on the impedance spectra, and induced by the molten carbonate salt, represent impedance responses from double layer capacitance at low frequency, in parallel with oxide capacitance at high frequency (See Figure 4.8- Figure 4.12).

The $T_{co}$ values in Table 4.5 undergo a cycle of increasing a decreasing with rising temperature when compared to the $C_{co}$ values in Table 4.6 which rise gradually with increasing temperature. This implies that Figure 4.7a and b suggest a simultaneous degradation and buildup of the outer oxide layer as the temperature increases. However, Figure 4.7c and d suggest a degradation of the outer oxide layer but as a slower rate same as to Figure 4.7a and b. In his book on "High-Temperature Corrosion and Materials Application", Lai [49] , reports that the corrosion of molten carbonates, when compared to molten chloride and fluoride salts is less. However, at lower temperatures, severity of molten carbonate corrosion is lessened, and varies based on corrosion mechanism and salt composition [49]. An increase in capacitance also suggest an increase in the roughness of the

electrode or the oxide layer on the electrode. Torabi et al. reported that the interface roughness of an electrode contributed to enhances electrical capacitance [50].

The values of $P_{co}$ in Table 4.5 deviate greatly from 1, and steadily decrease as temperature increases. The deviation of $P_{dl}$ and $P_{co}$ from 1 indicates a strong dispersion effect which is common with molten salt [51]. At 600 °C the values of $P_{co}$, $P_{dl}$ for both models is significantly small. On the other hand, the values of $P_{dl}$ at later temperatures is much more stable as temperature decreases. In a paper written by Ni et al. [51] studying the corrosion of stainless steel 310S, they report that a decrease in $P_{dl}$ was attributed to the partial loss of molten salt film and the roughness of the surface oxide layer.

The $R_{po}$ values which represent the resistance of the outer oxide layer show a similar trend in both types of fit in that, the resistance rises from 503 °C to 526 and then decrease at a rate of about half the previous value from 551°C to 603 °C. The decrease in resistance as temperature rises, suggest the oxide layer gets thinner and hence corrosion is enhanced. Xie at al report that a decrease in oxide resistance represents a decrease in size of the oxide layer and corroborate this finding with the anodic current density [19]. The decrease in outer resistance corresponds to an increase in $I_{corr}$ as shown in Table 4.4.

The values of $R_{ct}$ are magnitudes higher than that of $R_{po}$. This observation suggests a more stable inner oxide layer. However, when both models are compared, Figure 4.7b and 8d suggest a more stable inner oxide layer as they generally have the highest resistance values in Table 4.6. It is fascinating to see that as the resistance increases with rising temperature there is an exception at 577 °C for both models where resistance increases significantly from 3674 Ω cm2 to 5985 Ω cm2 (Table 4.5), and 3103 Ω cm2 to 6011 Ω cm2 (Table 4.6), and then drops significantly to a much lower resistance of 176 Ω cm2 (Table 4.5), and 170 Ω cm2 (Table 4.6). This huge drop suggests the drastic break down of the oxide layer at higher temperatures. this can be attributed to the formation of an oxide layer that formed from fast oxidation and prevented Faradaic current, showing that the blocking effect of the oxide layer is more profound as the temperature increases. The decrease in $R_{po}$ and $R_{ct}$ with rising temperature indicated that at higher temperatures the film is thin and thus a higher corrosion rate [3]. Another contributing factor to this is the presence of the Warburg element which suggesting an unstable oxide layer at 600 °C.

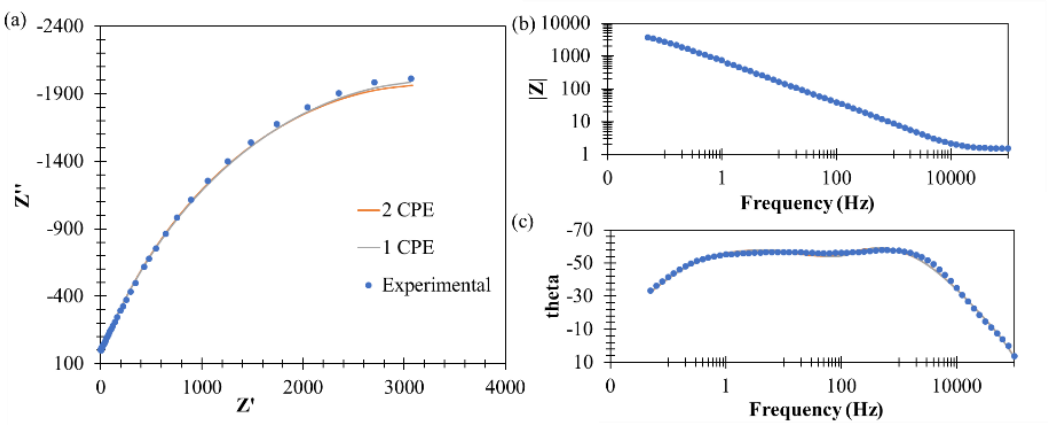


Figure 4.8. Nyquist (a) and Bode Plots (b,c) of type 304 stainless steel in $Li_2CO_3$-$K_2CO_3$ salt 503 ˚C after electrochemical impedance spectroscopy measurements. The orange line represent fitting with the equivalent model; figure 8a. The blue dots represent the experimental data. The grey line represents fitting with the equivalent model; figure 8b

.

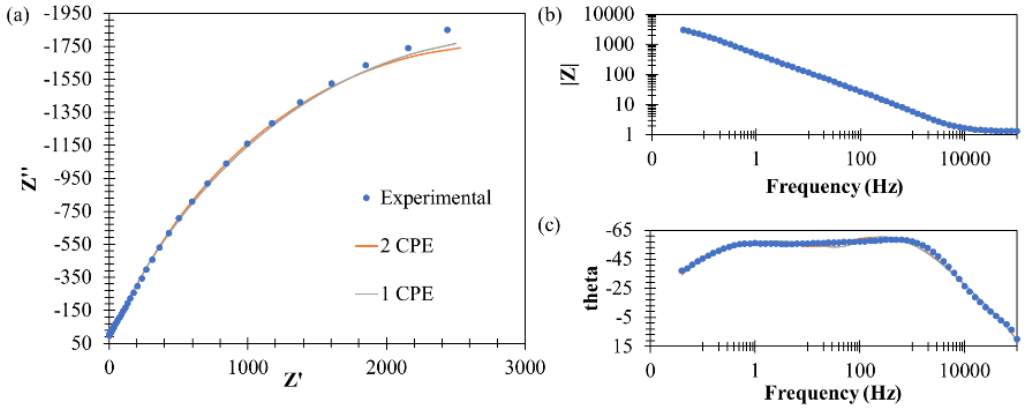


Figure 4.9. Nyquist (a) and Bode Plots (b,c) of type 304 stainless steel in $Li_2CO_3$-$K_2CO_3$ salt at 526 ˚C after electrochemical impedance spectroscopy measurements. The blue dots represent the experimental data. The orange line represent fitting with the equivalent model; figure 8a. The blue dots represent the experimental data. The grey line represents fitting with the equivalent model; figure 8b.

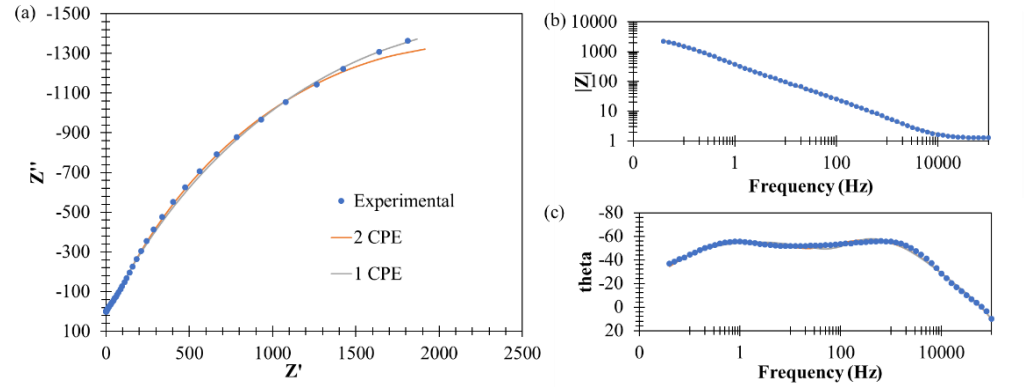


Figure 4.10. Nyquist (a) and Bode Plots (b,c) of type 304 stainless steel in $Li_2CO_3$-$K_2CO_3$ salt at 551 ˚C after electrochemical impedance spectroscopy measurements. The blue dots represent the experimental data. The orange line represent fitting with the equivalent model; figure 8a. The blue dots represent the experimental data. The grey line represents fitting with the equivalent model; figure 8b.

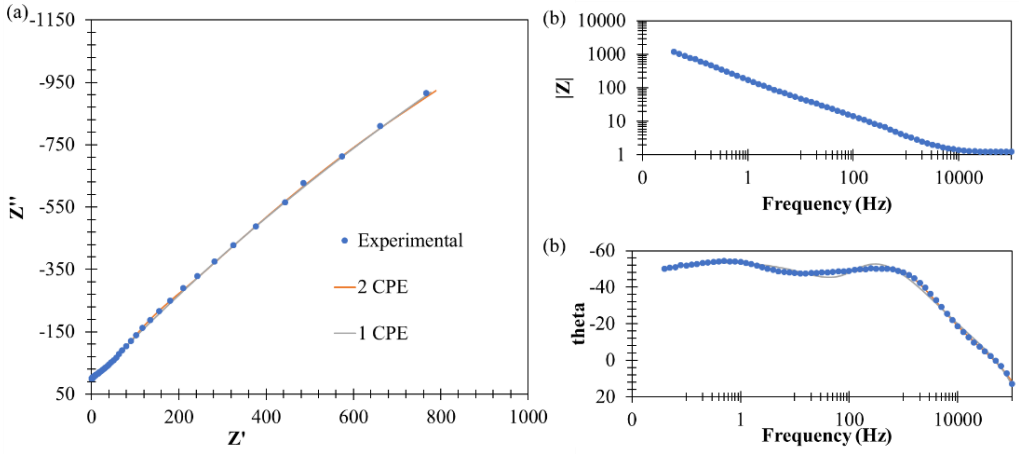


Figure 4.11. Nyquist (a) and Bode Plots (b,c) of type 304 stainless steel at 577 ˚C in $Li_2CO_3$-$K_2CO_3$ salt after electrochemical impedance spectroscopy measurements. The blue dots represent the experimental data. The orange line represent fitting with the equivalent model; figure 8a. The blue dots represent the experimental data. The grey line represents fitting with the equivalent model; figure 8b.

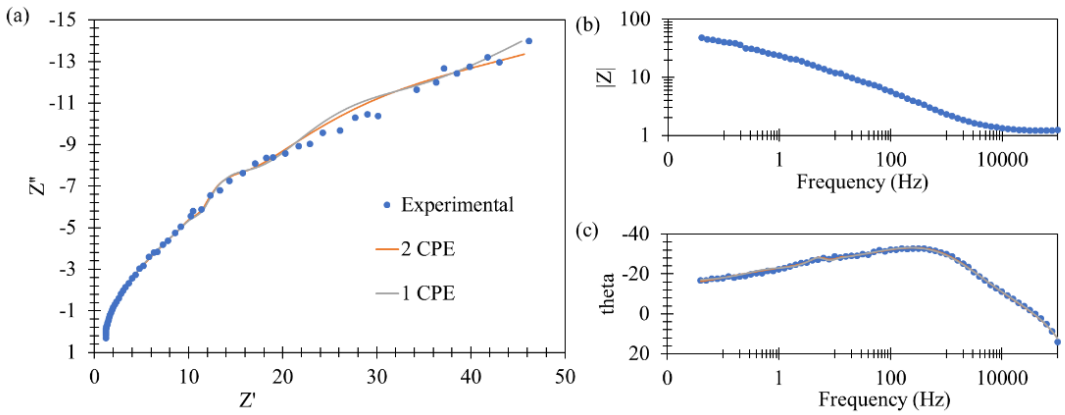


Figure 4.12. Nyquist (a) and Bode Plots (b,c) of type 304 stainless steel in $Li_2CO_3$-$K_2CO_3$ salt at 600 ˚C after electrochemical impedance spectroscopy measurements. The blue dots represent the experimental data. The orange line represent fitting with the equivalent model; figure 8c. The blue dots represent the experimental data. The grey line represents fitting with the equivalent model; figure 8d.

Table 4.5. EIS fit results using a Voigt circuit with two time constants (two constant phase elements) in series with an inductor for modeling the corrosion process of stainless steel 304 in molten Li2CO3-K2C03 salt at 503 °C, 526 °C, 551 °C, 577 °C and 600 °C based on Figure 8a and 8c.

| Temperature (°C) | $R_s$ (Ω $cm^2$) | $T_{co}$ (F $cm^{-2}$) | $P_{co}$ | $R_{po}$ (Ω $cm^2$) | $T_{dl}$ (F $cm^{-2}$) | $P_{dl}$ | W-R | W-T | W-P | L (H) | Chi Square | SS |
|---|---|---|---|---|---|---|---|---|---|---|---|---|
| 600 | 0.707±0.00976 | 0.0724±0.342 | 0.562±0.193 | 10.1±0.512 | 0.0601±0.185 | 0.232±0.0299 | 176±0.0796 | 0.204±0.0822 | 0.762±0.0436 | 5.067E-7±0.0328 | 0.000517 | 0.062 |

| Temperature (°C) | $R_s$ (Ω $cm^2$) | $T_{co}$ (F $cm^{-2}$) | $P_{co}$ | $R_{po}$ (Ω $cm^2$) | $T_{dl}$ (F $cm^{-2}$) | $P_{dl}$ | $R_{ct}$ (Ω $cm^2$) | L (H) | Chi Square | SS |
|---|---|---|---|---|---|---|---|---|---|---|
| 577 | 0.678±0.00880 | 1.29E-4±0.112 | 0.793±0.0266 | 7.86±0.108 | 2.92E-3±0.00915 | 0.652±0.005 | 5985±0.115 | 6.07E-7±0.0469 | 0.0014471 | 0.17654 |
| 551 | 0.694±0.012 | 7.07E-4±0.109 | 0.794±0.0258 | 15.3±0.127 | 1.20E-4±0.0115 | 0.698±0.0114 | 3674±0.0442 | 6.10E-7±0.0692 | 0.0020442 | 0.24939 |
| 526 | 0.724±0.0119 | 8.19E-4±0.132 | 0.807±0.0385 | 19.1±0.197 | 9.12E-4±0.0118 | 0.715±0.0135 | 3425±0.0465 | 6.090E-7±0.0659 | 0.0024172 | 0.2949 |
| 503 | 0.792 ± 0.0132 | 3.62E-4 ± 0.239 | 0.887 ± 0.0460 | 9.15 ± 0.178 | 6.08E-4 ± 0.0119 | 0.696 ± 0.814 | 3968 ± 0.0341 | 6.67E-7 ± 0.0633 | 0.00189 | 0.0226 |

Table 4.6. EIS fit results using a Voigt circuit with two time constants (one constant phase element and one capacitor) in series with an inductor for modeling the corrosion process of stainless steel 304 in molten $Li_2CO_3$-$K_2CO_3$ salt at at 503 °C, 526 °C, 551 °C, 577 °C and 600 °C based on Figure 8b and 8d

| Temperature (°C) | $R_s$ (Ω $cm^2$) | $C_{co}$ (F $cm^{-2}$) | $R_{po}$ (Ω $cm^2$) | $T_{dl}$ (F $cm^{-2}$) | $P_{dl}$ | W-R | W-T | W-P | L (H) | Chi Square | SS |
|---|---|---|---|---|---|---|---|---|---|---|---|
| 600 | 0.704±0.00521 | 0.157±0.121 | 2.34±0.108 | 0.0457±0.0103 | 0.243±0.02 | 170±0.0436 | 0.223±0.06 | 0.731±0.00898 | 5.15±0.0312 | 0.000586 | 0.0709 |

| Temperature (°C) | $R_s$ (Ω $cm^2$) | $C_{co}$ (F $cm^{-2}$) | $R_{po}$ (Ω $cm^2$) | $T_{dl}$ (F $cm^{-2}$) | $P_{dl}$ | $R_{ct}$ (Ω $cm^2$) | L (H) | Chi Square | SS |
|---|---|---|---|---|---|---|---|---|---|
| 577 | 0.657±0.0116 | 3.86E-4±0.0550 | 3.54±0.0528 | 2.97E-3±0.00941 | 0.621±0.00421 | 6011±0.163 | 6.37E-7± 0.0563 | 0.00231 | 0.285 |
| 551 | 0.669±0.0145 | 2.12E-4±0.0608 | 6.00±0.0620 | 1.22E-3±0.0112 | 0.663±0.00422 | 3103±0.0440 | 6.42E-7±0.0688 | 0.00307 | 0.375 |
| 526 | 0.958 ± 0.0135 | 2.85E-4 ± 0.0711 | 7.19 ± 0.0751 | 9.09E-4 ± 0.0110 | 0.690±0.0038 | 3679±0.0377 | 6.37E-7± 0.0713 | 0.00312 | 0.384 |
| 503 | 0.780 ± 0.0126 | 1.73E-4 ± 0.0680 | 5.73 ± 0.0711 | 6.11E-4 ± 0.00948 | 0.687 ± 0.00325 | 4090 ± 0.0283 | 6.83E-7 ± 0.0631 | 0.002 | 0.243 |

#### 4.2.3.4 Corrosion mechanism of Stainless Steel in the eutectic salt

EIS analysis and plots show that when stainless steel 304 is immersed into the salt, a porous oxide layer ($C_{dl}$) is formed on the surface of the electrode. The formation of the oxide layer creates some resistance between the oxide layer and the salt. However, the porosity of the oxide layer allows for the exchange of ions between the electrode and the salt. With time a new oxide layer ($C_{co}$) is formed as added protection to stainless steel 304. This formation protects the underlying oxide layer and is created as a result of oxide layer ($C_{dl}$) interaction between the salt and the first oxide layer. However, from analysis made above and data collected, $C_{co}$ is less resistive compared to $C_{dl}$ and dissociates almost completely at 600 °C Figure 4.13 shows a physical representation of the kinetics which take place when the stainless steel 304 alloy is placed in the molten carbonate salt. Where $R_s$ is the electrolyte resistance, ($R_{co}$ $C_{co}$) and ($R_{ct,}$ $C_{dl}$) represent time constants.

Ni and Lu [20] reported the formation of three oxide layers on the stainless steel 304 after an immersion time of 120 hours, with a combined thickness of 40 µm. The outermost and innermost layers was separated by a dark region. They further report spallation of the outermost layer. Using XRD, Ni and Lu confirmed that the outermost layer consisted mostly of $LiFeO_2$. The intermediate layer was a mixture of $LiFeO_2$, $LiCrO_2$, $(Fe,Ni)Cr_2O_4$ and Ni. The innermost layer was $(Fe,Ni)Cr_2O_4$. Judging by the study conducted by Ni and Lu, the two oxide layers (inner and outer layers) seen in figure 11 consist of $LiFeO_2$, $LiCrO_2$, $(Fe,Ni)Cr_2O_4$ and Ni for the outer layer, and $(Fe,Ni)Cr_2O_4$ for the inner layer. Ni and Lu further report that the oxidation of stainless steel in carbonate salts can be separated into two reactions; the reaction on the anode side, and the reaction on the cathode side. At the cathode, oxygen is reduced. Creating $O^{-}_2$ or $O^{2-}_2$ based on reaction 9 and 10 respectively, and subsequently to oxygen ion by the provision of electrons from the anode as shown by reactions 11 and 12.

$$3O_2 + 2CO_3^{2-} \rightarrow 4O_2^{-} + 2CO_2 \quad (9)$$

$$O_2 + 2CO_3^{2-} \rightarrow 2O_2^{2-} + 2CO_2 \quad (10)$$

$$O_2^{2-} + 2e^{-} \rightarrow 2O^{2-} \quad (11)$$

$$O_2^{-} + 3e^{-} \rightarrow 2O^{2-} \quad (12)$$

At the anode, a sample metal (M) will be oxidized as

$$M + ne^{-} \rightarrow M^{+} \quad (13)$$

where *n* is the number of electrons. In the case of stainless steel in $Li_2CO_3$-$K_2CO_3$, the metal ions combine with one of the carbonate salts, after reacting with oxygen to form an oxide. Cr in Fe-Cr alloys oxidize faster than Fe when immersed into molten salt. The formed Cr oxide dissolves faster in the salt than its iron oxide counterpart. When this occurs, the iron oxide layer is left on the surface of the electrode and lithiated to form lithium ferrite [20].

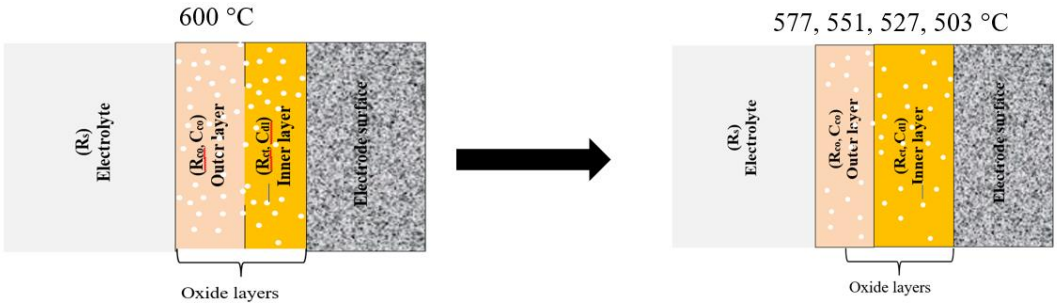


Figure 4.13. Corrosion mechanism for stainless steel 304 in molten carbonate $Li_2CO_3$-$K_2CO_3$ salts with varying temperatures of 503 °C, 526 °C, 551 °C, 577 °C and 600 °C, displaying the number of oxide layers formed of the surface f the electrode as modelled by Figure 4.7.

### 4.2.4.Electrochemical study of Nickel in molten Eutectic Carbonate Salt

#### 4.2.3.4 Linear Polarization measurements of Nickel in molten Eutectic Carbonate salts.

Figure 4.14 shows a general increase in potential as temperature decreases. The LPR analysis for 527 °C takes place at a much higher potential than that of 502 °C, and the current range for 502 °C and 604 °C is much larger compared to the rest of the other temperatures. Parts of the reaction for 527 °C and 542 °C, at approximately 0.025 mA, are solely driven by current, and could be responsible for the decrease in $R_p$ at these values as shown in Table 4.7. The true $R_p$ [40] were obtained by calculating the slope from the current-potential plot at the zero current region, and multiplying the result by the nickel surface area at various temperatures (Figure 15 and Table 9). As the temperature decreased from 604 °C to 502 °C, Rp increased from 129 Ohms.cm$^2$ to 1876.6 Ohms.cm$^2$, suggesting an increasing resistance of the nickel to the salt [20]. The sudden increase in $R_p$ at 573 °C, suggests the formation of soluble oxide layer which provides protection to the elctrode for a short while. However, this oxide layer dissolves at 604 °C, as indicated by the sudden decrease in $R_p$. The OCP values shifted from cathodic (more negative) values at 604 °C to more anodic values at 503 °C (Figure 4.14), indicating the formation of an oxide layer at lower temperatures and dissolution of the oxide layer at higher temperatures [41], conforming with a study carried out by Choudhary et al., on the relationship between OCP and Rp [42]. Generally, as $R_p$ increases OCP increased as well as seen in Table 4.7.

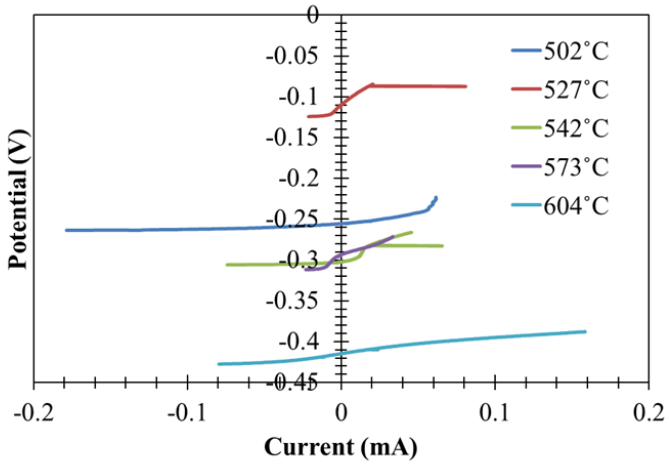


Figure 4.14. LPR measurements for nickel conducted with a potential range of -20mV to 20mV at various temperatures in $Li_2CO_3$-$K_2CO_3$ salt at 502 °C, 527 °C, 542 °C, 573°C and 604 °C to determine the linear polarization resistance, $R_p$.

Table 4.7. Polarization resistance ($R_p$) for Ni with surface area of 52.42 $mm^2$ in Li2CO3-K2CO3 salt at 502 °C, 527 °C, 542 °C, 573°C and 604 °C.

| Temperature (˚C) | Rp (Ohms.$cm^2$) | OCP (mV) |
|---|---|---|
| 502 | 1876.6 | -369 |
| 527 | 880.7 | -370 |
| 542 | 186.6 | -428 |
| 573 | 1106.1 | -409 |
| 604 | 129.0 | -576 |

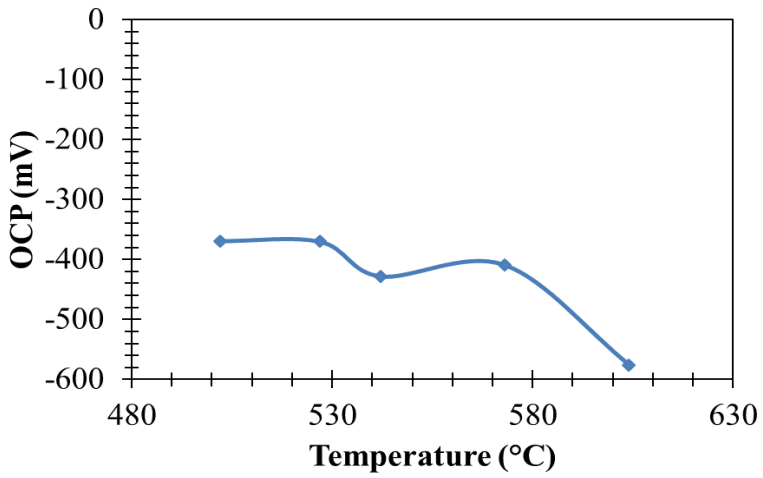


Figure 4.15. Open circuit potential versus temperature for nickel during LPR measurement run in $Li_2CO_3$-$K_2CO_3$ salt at 502 °C, 527 °C, 542 °C, 573°C and 604 °C.

### 4.2.3.4 Tafel Measurements of Nickel in the Eutectic Salt

Figure 4.16 shows the potentiodynamic polarization curves for nickel in $Li_2CO_3$-$K_2CO_3$ at 502 °C, 527 °C, 542 °C, 573°C and 604 °C, respectively. The potentiodynamic curves show a constant cycle of active dissolution, passivation, trans-passivation of the nickel electrode indicated by the curves on anodic slopes. However, it is interesting to note that the OCP shifts from more cathodic values to less cathodic values as the temperature decreases. Nickel performs better at lower temperatures based on the experimental conditions described (See Figure 4.17). The cycle of active, passivation and trans passive is corroborated by the lack of a trend displayed by the $i_{corr}$ values in Table 4.8. There is no trend in the $i_{corr}$ values. At 600 °C, the high $i_{corr}$ value 198.4 μA/cm$^2$, suggests an aggressive breakdown of the protective oxide layer. However, this value is decreased at 573 °C to 34.9 μA/cm$^2$ owing to the increase in the slope of the cathodic curve, suggesting a delay in anodic reaction, hence a hindrance in the oxidation of the metal. However, this oxide layer is short lived as the $i_{corr}$ value at 542 °C increases significantly by more than fourfold to 147 .5 μA/cm$^2$, suggesting an active corrosion state. The anodic and cathodic slopes for 542 °C in Table 4.8, are the same, indicating an ongoing active process of equal rate of reactants versus products formation. A decrease in $i_{corr}$ at 527 as seen in Table 4.8 can be attributed to the slightly higher cathodic slope, which is also seen at 502 °C.

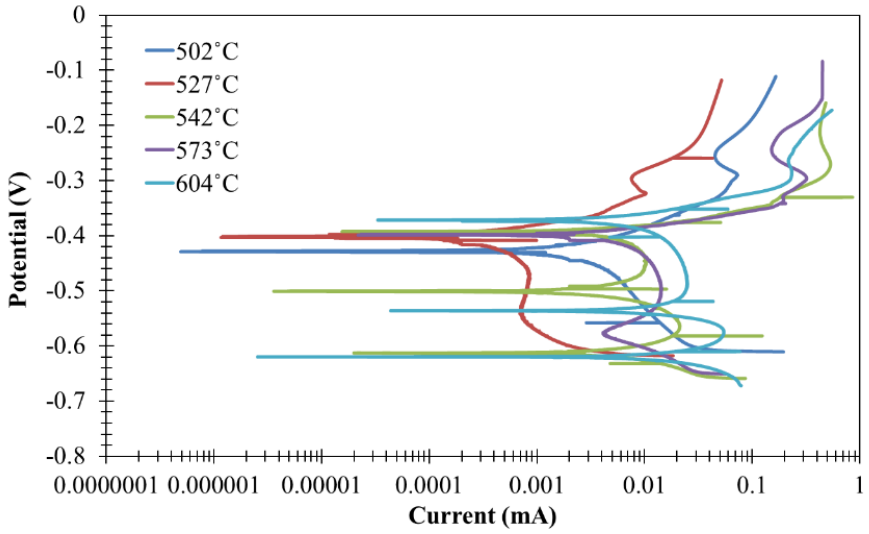


Figure 4.16. Potentiodynamic polarization curves for nickel in $Li_2CO_3$-$K_2CO_3$ at 502 °C, 527 °C, 542 °C, 573°C and 604 °C, respectively, conducted at a potential range of -0.25V to 0.25V vs OCP.

Table 4.8. Cathodic beta ($b_c$) and anodic beta ($b_a$) constants from Tafel measurements for nickel and calculated corrosion current density ($i_{corr}$) and corrosion rate (CR) for nickel using the $R_p$, $b_a$, and $b_c$, in $Li_2CO_3$-$K_2CO_3$ salt at 502 °C, 527 °C, 542 °C, 573°C and 604 °C, respectively.

| Temperature (˚C) | bc (mV) | ba (mV) | OCP (mV) | $i_{corr}$ (μA/cm$^2$) | CR(mm/yr) |
|---|---|---|---|---|---|
| 502 | 187 | 88.4 | -429 | 13.9 | 0.003 |
| 527 | 538 | 54.4 | -403 | 24.4 | 0.01 |
| 542 | 262 | 83.7 | -393 | 148 | 0.03 |
| 573 | 253 | 136 | -399 | 34.9 | 0.01 |
| 604 | 315 | 73.1 | -371 | 198 | 0.04 |

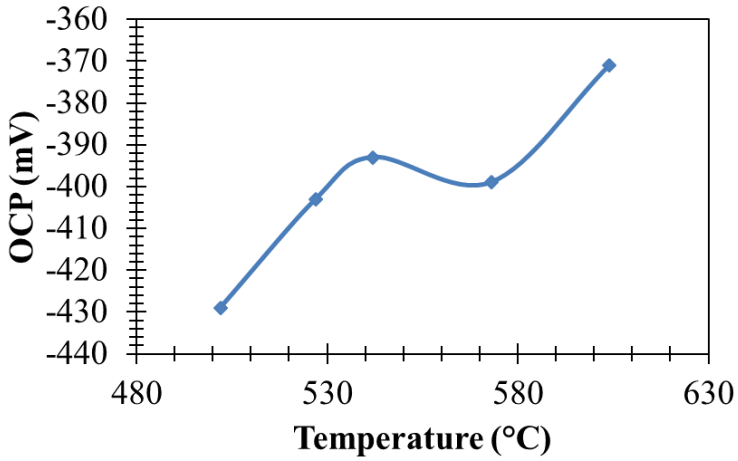


Figure 4.17. Open circuit potential versus temperature for nickel during Tafel measurement run in $Li_2CO_3$-$K_2CO_3$ salt at 502 °C, 527 °C, 542 °C, 573°C and 604 °C, respectively.

#### 4.2.3.4 EIS measurements for Nickel in the eutectic salt

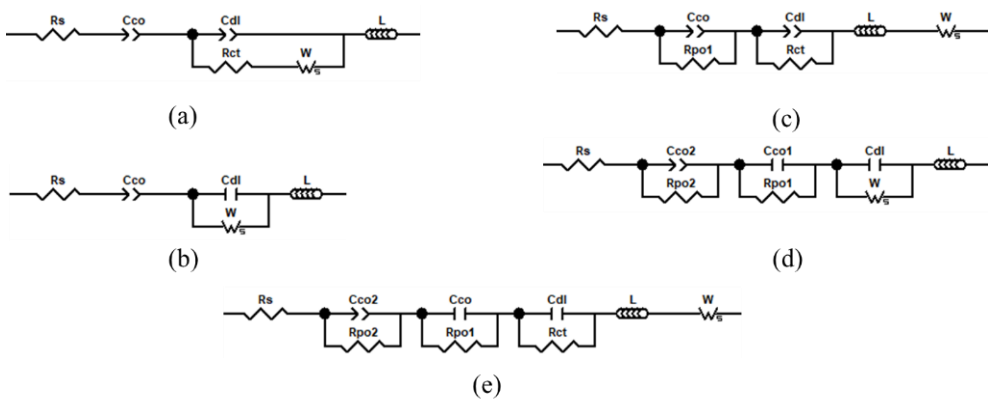


Figure 4.18. Equivalent circuits for fitting bode and Nyquist data for 502˚C, 527˚C, 542˚C, 573˚C and 604˚C.(a) equivalent circuit for fitting of 502˚C,(b) equivalent circuit for fitting of 527˚C. (c) equivalent circuit for fitting of 542˚C. (d) equivalent circuit for fitting of 573˚C and, (e) equivalent circuit for fitting of 604˚C

Figure 4.18 shows the equivalent circuits used to model the EIS data for nickel. The Nyquist plot for all the temperatures show characteristics of diffusion at low frequency. 502 °C was modelled with a resistor in series with a constant phase element, which is in series with a parallel combination of a constant phase element, a resistor and Warburg element, altogether in series with an inductor. A resistor in series with a capacitor forms a vertical line. However, the modeling shows that in some cases, when modeled a resistor is combined with a constant phase element, a slanted line can be achieved as seen for 502 °C in Figure 4.19. There is one distinct peak at high frequency for 502 °C. However, at 527 °C and 542 °C there are two distinct peaks, one at low frequency and the other at high frequency. At 573 °C and 604 °C, there appears to be a tiny peak at approximately 8 Hz. Each peak is modeled by a constant phase element, which is a parallel combination of a resistor and a capacitor or constant phase element. The presence of the Warburg element suggests an instability of the oxide layer. This can be seen by the fluctuations of $R_{ct}$, $R_{po1}$, and $R_{po2}$, as temperature decreases. As temperature decreases, the value of $R_{ct}$ increases. However, $R_{po1}$ is significantly larger than $R_{ct}$, suggesting a more stable second layer. A third layer forms at higher temperatures but is short-lived as it does not appear at 542 °C, 527 °C and 502 °C. The $P_{dl}$ value for 604 °C is very close to 1, suggesting a more stable inner oxide layer. Hence higher $R_{dl}$ values at 542 °C and 502 °C. The values of $R_{po1}$ are significantly larger at 604 °C, 573 °C, and 542 °C, representing an initial resilient second oxide layer. However, with time the oxide layer is dissolved

and is evident from the appearance of the Warburg element in Figure 4.18 a and b, resulting in a short lives outermost oxide layer.

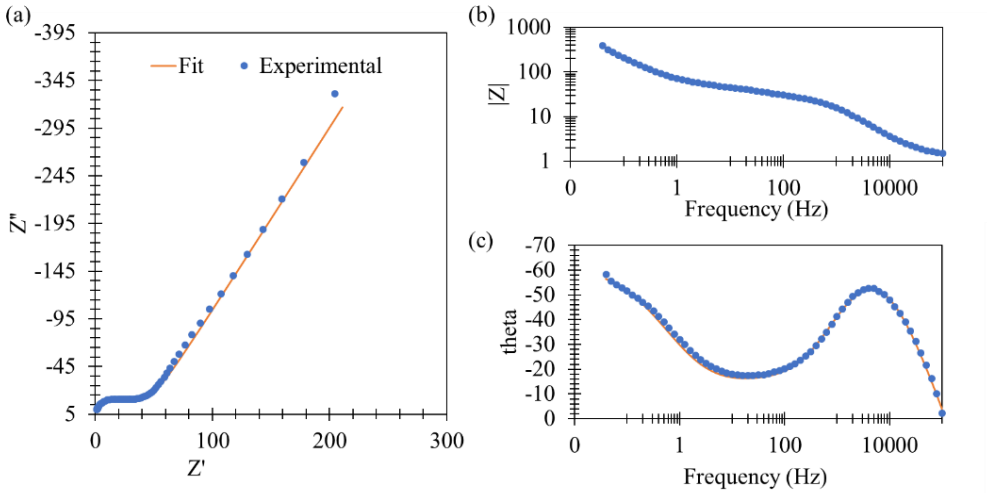


Figure 4.19. Nyquist (a) and Bode Plots (b,c) of nickel in $Li_2CO_3$-$K_2CO_3$ salt at 502 ˚C after electrochemical impedance spectroscopy measurements. The blue dots represent the experimental data. The orange line represents fitting with the equivalent model; figure 19a.

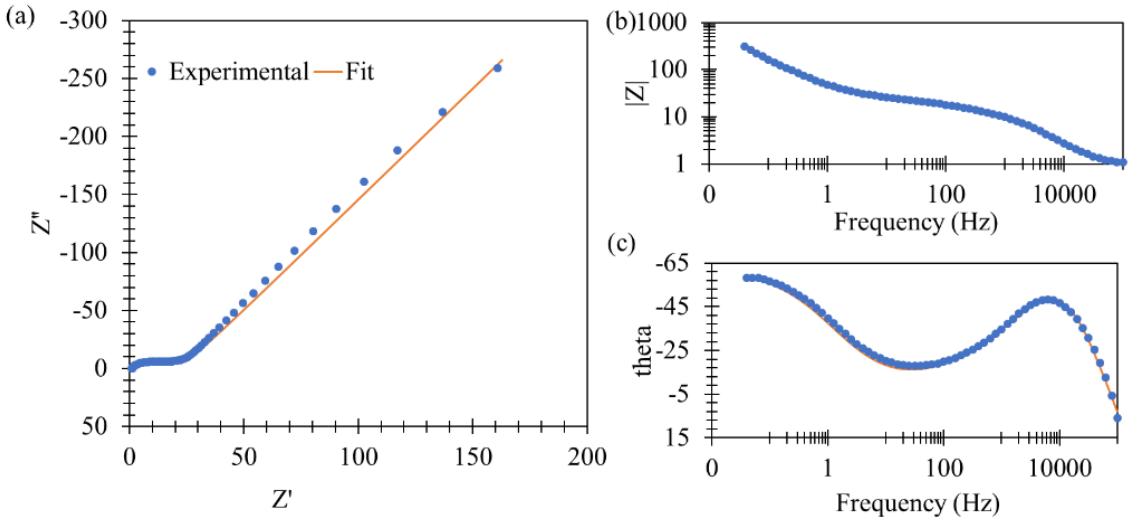


Figure 4.20. Nyquist (a) and Bode Plots (b,c) of nickel in $Li_2CO_3$-K2CO3 salt at 527 ˚C after electrochemical impedance spectroscopy measurements. The blue dots represent the experimental data. The orange line represents fitting with the equivalent model; figure 19b.

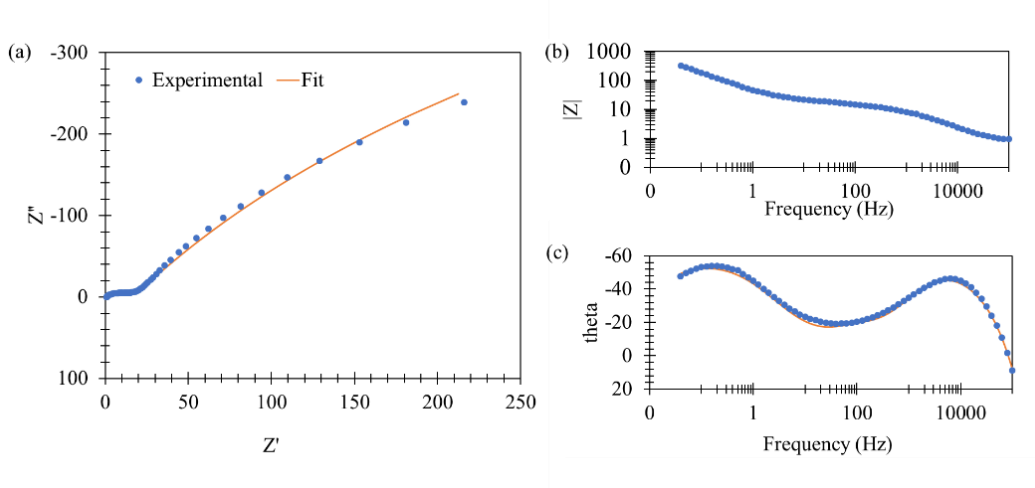


Figure 4.21. Nyquist (a) and Bode Plots (b,c) of nickel in $Li_2CO_3$-$K_2CO_3$ salt at 542 ˚C after electrochemical impedance spectroscopy measurements. The blue dots represent the experimental data. The orange line represents fitting with the equivalent model; figure 19c.

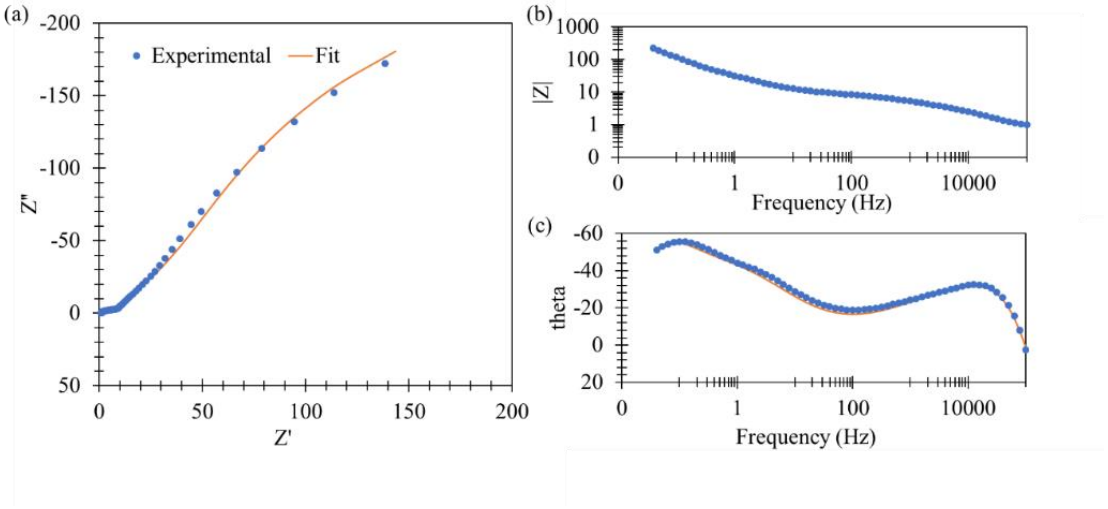


Figure 4.22. Nyquist (a) and Bode Plots (b,c) of nickel in $Li_2CO_3$-$K_2CO_3$ salt at 573 ˚C after electrochemical impedance spectroscopy measurements. The blue dots represent the experimental data. The orange line represents fitting with the equivalent model; figure 19d.

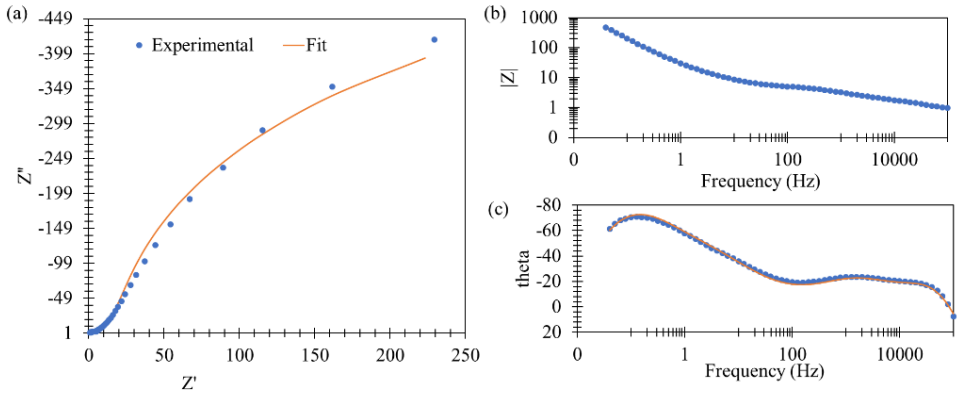


Figure 4.23. Nyquist (a) and Bode Plots (b,c) of nickel in $Li_2CO_3$-$K_2CO_3$ salt at 604 ˚C after electrochemical impedance spectroscopy measurements. The blue dots represent the experimental data. The orange line represents fitting with the equivalent model; figure 19e.

Table 4.9. EIS fit results of nickel in molten $Li_2CO_3$-$K_2CO_3$ salt at 502 °C, 527 °C, 542 °C, 573°C and 604 °C, respectively, based on figure 19.

| Temperature (°C) | $R_s$ ($\Omega$ cm$^2$) | $T_{co}$ ($F.cm^{-2}$)-2 | $P_{co}$-2 | $R_{po}$-2 ($\Omega$ cm$^2$) | $T_{co}$ ($F.cm^{-2}$)-1 | $P_{co}$-1 | $R_{po}$-1 ($\Omega$ cm$^2$) | $T_{dl}$ ($F.cm^{-2}$) | $P_{dl}$ | $R_{ct}$ ($\Omega$ cm$^2$) | L (H) | W-R | W-T | W-P | Chi Square | SS |
|---|---|---|---|---|---|---|---|---|---|---|---|---|---|---|---|---|
| 604 | 0.336 ± 0.083 | 0.0312 ± 0.086 | 0.620 ± 0.045 | 13.5± 0.12 | 0.0156 ± 0.012 | n/a | 509 ± 0.030 | 3.20E-5 ± .15 | n/a | 0.178 ±0.14 | 6.18E-7 ± 0.061 | 1.84 ± 0.080 | 1.37E-3 ± 0.13 | 0.374 ± 0.13 | 0.00129 | 0.153 |
| 573 | 0.452 ± 0.029 | 0.0246 ± 0.056 | 0.620± 0.038 | 37.5± 0.17 | 0.0372± 0.049 | n/a | 222 ± 0.048 | 6.95E-6 ± 0.67 | n/a | n/a | 6.07E-7 ± 0.068 | 3.95 ± 0.048 | 2.15E-3 ± .22 | 0.279 ± 0.034 | 0.00154 | 0.183 |
| 542 | 0.365 ± 0.086 | n/a | n/a | n/a | 1.40E-2 ± 0.0088 | 0.701± 0.010 | 762 ± 0.11 | 1.82E-4 ± .22 | 0.795 ± 0.039 | 5.21 ± 0.13 | 7.66E-7 ± 0.048 | 3.46± 0.24 | 0.0118 ± 0.13 | 0.454± .10 | 0.00134 2 | 0.159 72 |
| 527 | 0.568 ± 0.010 | n/a | n/a | n/a | 1.66E-2 ± 0.0070 | 0.6941± 0.0067 | n/a | n/a | n/a | n/a | 5.31E-7 ± 0.055 | 12.2± 0.020 | 8.78E-3 ± 0.14 | 0.249± 0.025 | 0.00129 | 0.157 |
| 502 | 0.727 ± 0.013 | n/a | n/a | n/a | 0.0140 ± 0.0097 | 0.695 ± 0.0088 | n/a | 5.63E-5 ± .087 | 0.843 ± 0.0094 | 11.45 ± 0.072 | 5.16E-07 ± 0.066 | 12.3 ± 0.12 | 0.0621 ± 0.24 | 0.308 ± 0.097 | 0.00074 5 | 0.089 42 |

#### 4.2.3.4 Corrosion mechanism of Nickel in the eutectic salt

Figure 4.24 shows the corrosion mechanism for nickel in the molten eutectic salt in terms of oxide layer formation as temperatures decreases. At 604 °C and 573 °C there are three layers of oxide. However, as temperature decreases and diffusion takes place, the oxide layer is reduced to two at 542 °C and then to one oxide layer at 502°C and 527 °C. The possible formation of the oxide layer is primarily nickel oxide which performs better at higher temperatures

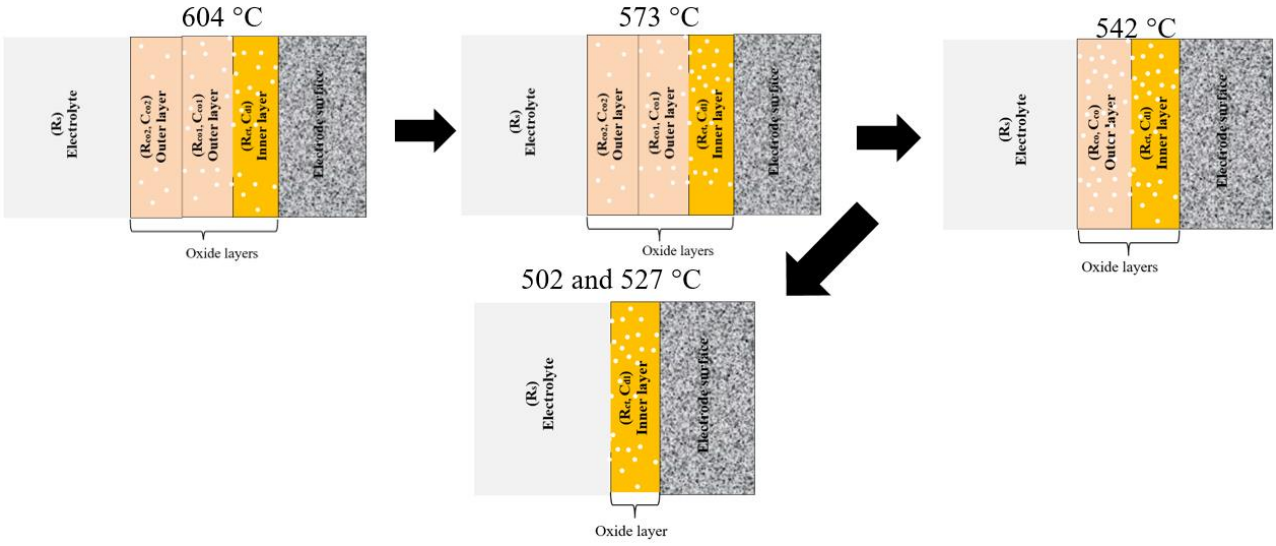


Figure 4.24. Corrosion mechanism for nickel in molten carbonate $Li_2CO_3$-$K_2CO_3$ salts with varying temperatures of 503 °C, 527 °C, 542 °C, 573 °C and 604 °C, displaying the number of oxide layers formed of the surface of the electrode as modelled by Figure 4.18

### 4.2.4. Electrochemical study of Inconel 600 in Eutectic Salt

#### 4.2.3.4 Linear Polarization measurement of Inconel 600 in Eutectic Molten Carbonate salt

Figure 4.25 shows the linear polarization measurements for Inconel in the eutectic salt. There is no correlation between the OCP and temperature for Inconel 600. However, at the start of the experiment, the OCP is very cathodic but at later temperatures OCP becomes significantly less cathodic as seen in Figure 4.25. Thus, the huge jump in $R_p$ from 600 °C to 501 °C. It is interesting to note that unlike the other metals that have been spoken of, at higher temperatures, Inconel 600 is able to withstand corrosion. However, even though there is a sudden decrease in $R_p$ at 573 °C, suggesting the formation of soluble oxide layer which provides protect for a short while, $R_p$ becomes stable with time. As temperature decreases, the oxide layer becomes more stable, as seen by the steady rise in $R_p$. The OCP values shifted from cathodic (more negative) values at 600 °C to more anodic values at 501 °C (Figure 4.25), indicating the formation of an stable oxide layer at lower temperatures and dissolution of the oxide layer at higher temperatures [41]. Generally, as $R_p$ increases OCP increased as well as seen in Table 4.10.

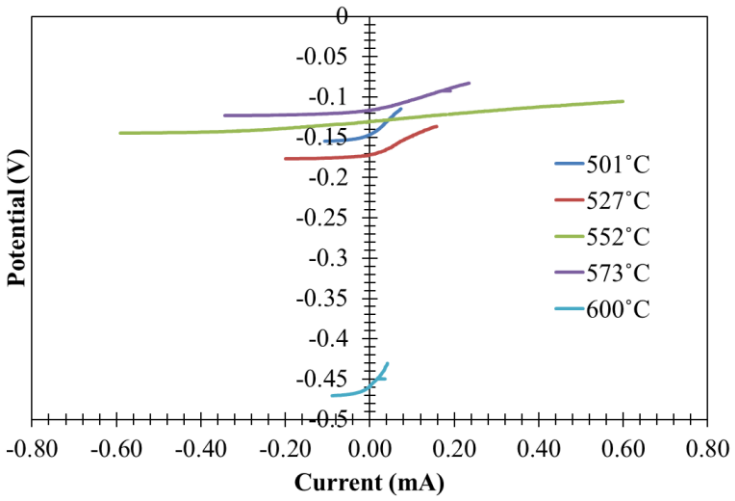


Figure 4.25. LPR measurements for Inconel 600 conducted with a potential range of -20mV to 20mV at various temperatures in $Li_2CO_3$-$K_2CO_3$ salt at 501 °C, 527 °C, 552 °C, 573°C and 600 °C to determine the polarization resistance, $R_p$.

Table 4.10. Polarization resistance ($R_p$) for Inconel with surface area of 100.24 $mm^2$ in $Li_2CO_3$-$K_2CO_3$ salt at 501 °C, 527 °C, 552 °C, 573°C and 600 °C.

| Temperature (˚C) | Rp (Ohms.$cm^2$) | OCP (mV) |
|---|---|---|
| 501 | 255.5 | -148 |
| 527 | 102.2 | -173 |
| 552 | 47.8 | -130 |
| 573 | 83.4 | -117 |
| 600 | 513.2 | -459 |

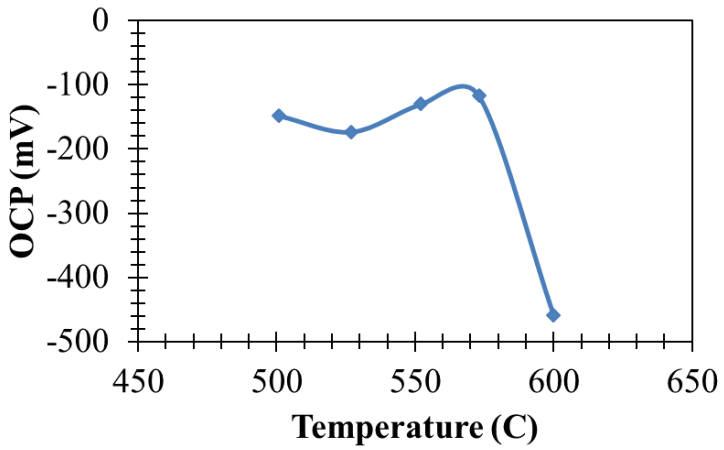


Figure 4.26. Open circuit potential versus temperature for Inconel 600 during LPR measurement run in in $Li_2CO_3$-$K_2CO_3$ salt at 501 °C, 527 °C, 552 °C, 573°C and 600 °C.

#### 4.2.3.4 Tafel measurements for Inconel 600 in molten eutectic carbonate salt

Figure 4.27 shows the potentiodynamic polarization curves for Inconel 600 in $Li_2CO_3$-$K_2CO_3$ at 501 °C, 527 °C, 552 °C, 573°C and 600 °C, respectively. The potentiodynamic curves show a constant cycle of active dissolution, passivation, trans-passivation of the Inconel 600 electrode. However, it is interesting to note that the OCP is rather more positive as 552 °C. A similar grouping as shown by the LPR measurements can be seen in Figure 27. On the anodic curves 552 °C and 527 °C, there appears to be little spikes, suggesting the formation of metal stable pits. However, the oxide layer the proves to be somewhat stable as the spikes are not seen at 600 °C. This is evident is the significant drop in $i_{corr}$ from 573 °C to 600 °C (see Table 4.11). The evidence of the spikes suggests the dissolution of the oxide layer and this is also evident at the rather large value of $i_{corr}$ for 552 °C, which is about a six-fold increase from 573 °C to 552 °C. However, there is a drop in $i_{corr}$ from 656.4 µA/cm$^2$ at 552 °C to 214 µA/cm$^2$ at 527 °C suggesting the recovery of the oxide layer as a result of insoluble corrosion products.

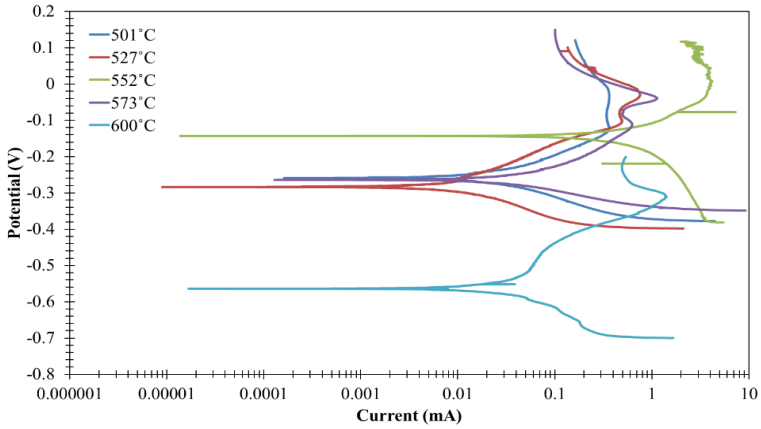


Figure 4.27. Polarization curves for Inconel 600 in $Li_2CO_3$-$K_2CO_3$ at 501 °C, 527 °C, 552 °C, 573°C and 600 °C, respectively, conducted at a potential range of -0.25V to 0.25V vs OCP.

Table 4.11. Cathodic beta ($b_c$) and anodic beta ($b_a$) constants from Tafel measurements for Inconel 600 and calculated corrosion current density ($i_{corr}$) and corrosion rate (CR) for Inconel 600 using the $R_p$, $b_a$, and $b_c$, in $Li_2CO_3$-$K_2CO_3$ salt at 501 °C, 527 °C, 552 °C, 573°C and 600 °C

| Temperature (˚C) | bc (mV) | ba (mV) | OCP (mV) | $i_{corr}$ (μA/cm$^2$) | CR (mm/yr) |
|---|---|---|---|---|---|
| 501 | 90 | 120 | -259 | 87.2 | 0.01 |
| 527 | 90 | 114 | -284 | 214.5 | 0.02 |
| 552 | 240 | 104 | -143 | 656.4 | 0.07 |
| 573 | 54 | 113 | -128 | 190.5 | 0.02 |
| 600 | 105 | 333 | -564 | 67.4 | 0.01 |

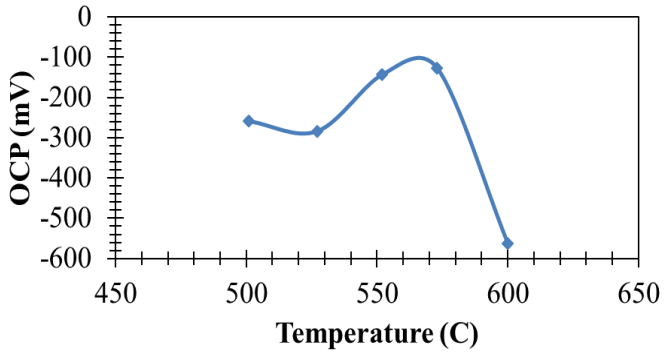


Figure 4.28. Open circuit potential versus temperature for Inconel 600 during Tafel measurement run in Li-$_2CO_3$-$K_2CO_3$ salt at 501 °C, 527 °C, 552 °C, 573°C and 600 °C.

#### 4.2.3.4 EIS measurements of Inconel 600 in molten Carbonate salt

Further tests were done to confirm the results reported by the LPR and Tafel measurements. Figure 4.29 show the equivalent circuit used to fit the EIS data for Inconel 600. Figure 4.29a is a Voigt circuit with two time constants. Figure 4.29b and e are Voigt circuits with two time constants in series with an inductor. Figure 4.29c is a Voigt circuit with two time constants in series with an inductor and a Warburg element. Lastly, Figure 4.29d is a Voigt circuit with three time constants in series with an inductor. $R_s$ represent the solution resistance, $C_{co2}$ represents the capacitance of the outermost oxide layer, $R_{po2}$ represents the resistance of the outermost oxide layer, $C_{co1}$ and $C_{co}$ are the capacitance of the intermediate oxide layer. $R_{po1}$ and $R_{po}$ are the resistance of the of the intermediate oxide layer. $C_{dl}$ is the double layer capacitance, $R_{ct}$ is the resistance of the double layer, L is an inductor and W is a Warburg element. ->>- represents a constant phase element and -||- represents a capacitor. At temperatures 501, 527, and 552 °C, there is a peak at low frequency and one at high frequency on the frequency-theta plot. Each peak represents a time constant which is the parallel combination of a capacitor and a resistor. However, at 577 °C, there is a third peak at approximately 100 Hz. At 600 °C, the peak at low frequency disappears, with a peak at approximately 100 Hz and high frequency. There is also a general increase in Rct as the temperature decreases from 600 to 501 °C. However, the resistances are significant at 527 and 501 °C suggesting the formation of a much stable oxide layer on the surface of the electrode. The increase in resistance could also be as a result of the buildup of corrosion products on the surface of as a result of the alloy trying to prevent further corrosion due to the dissolution of the oxide layer at 552 °C as shown by the presence of the Warburg element at 552 °C. Rpo1 shows the highest resistance at 600 °C with a drastic increase by about 350 times from 577 °C to 600 °C as seen in Table 4.12. This suggests the instability of the outside oxide layer at 577 °C and a very increase of corrosion products at 600 °C. However, at 577 °C there is an appearance of a third layer which is not present at the other temperatures, suggesting the breakdown of the short-lived oxide layer. The $P_{dl}$ value at 600 °C is close to one suggesting that the oxide layer is less permeable to the electrolyte. However, with time the oxide layer becomes less stable and is shown by the presence of the Warburg element at 552 °C as seen in Figure 4.29c.

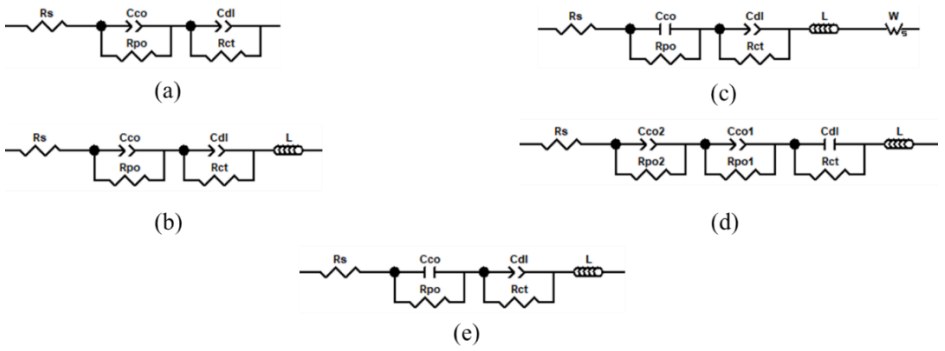


Figure 4.29. Equivalent circuits for fitting bode and Nyquist data for 501˚C, 527˚C, 552˚C, 577˚C and 600˚C.(a) Voigts circuit with two time for initial fitting of 501˚C. (b) Voigts circuit with two time constants (two constant phase elements) in series with an inductor for fitting 527˚C. (c) Voigts circuit with two time constants in series with an inductor and Warburg element for fitting 552˚C. (d) Voigts circuit with three time constants in series with an inductor for fitting of 577˚C (e) Voigts circuit with two time constants (one constant phase elements and one capacitor) in series with an inductor for fitting 600˚C.

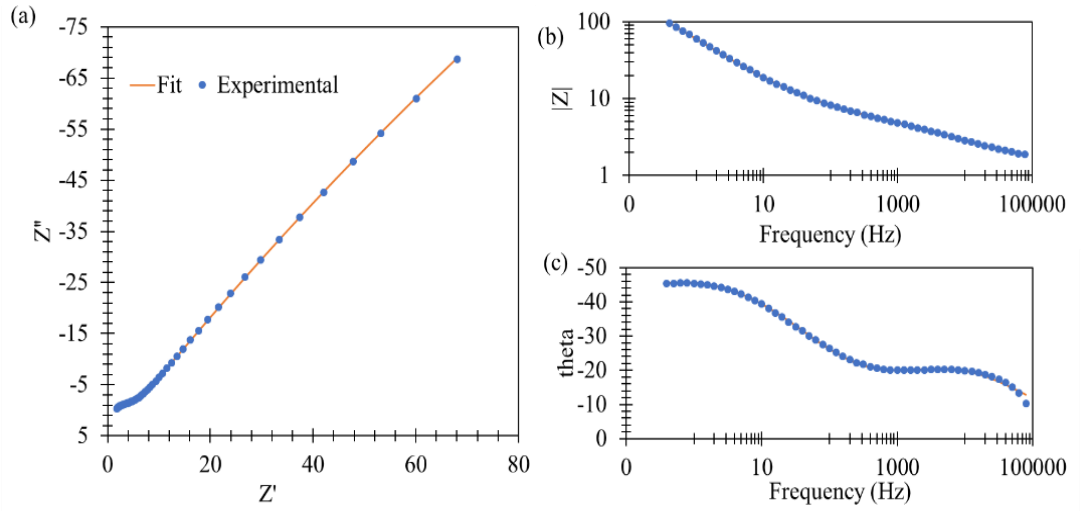


Figure 4.30. Nyquist (a) and Bode Plots (b,c) of Inconel 600 in $Li_2CO_3$-$K_2CO_3$ salt at 501 ˚C after electrochemical impedance spectroscopy measurements. The blue dots represent the experimental data. The orange line represents fitting with the equivalent model; figure 29a.

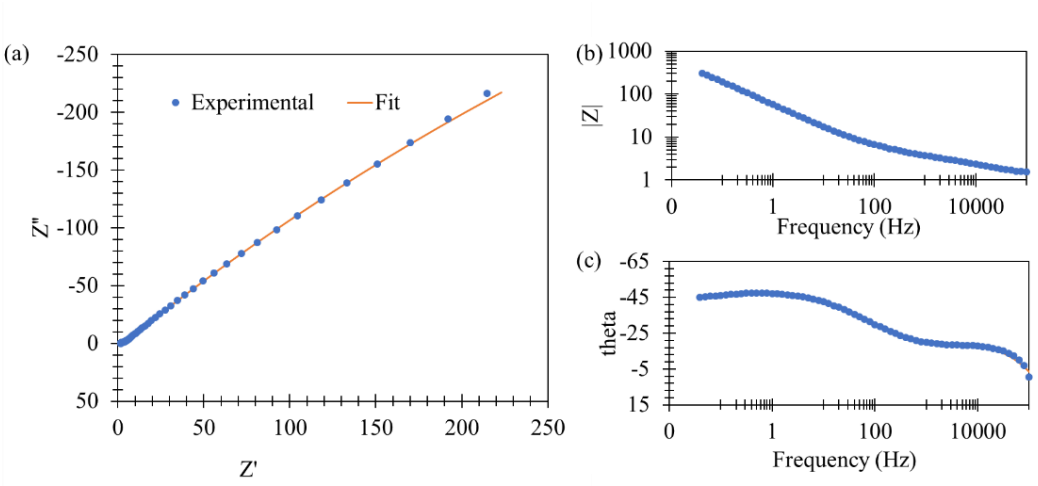


Figure 4.31. Nyquist (a) and Bode Plots (b,c) of Inconel 600 in $Li_2CO_3$-$K_2CO_3$ salt at 527 ˚C after electrochemical impedance spectroscopy measurements. The blue dots represent the experimental data. The orange line represents fitting with the equivalent model; figure 29b.

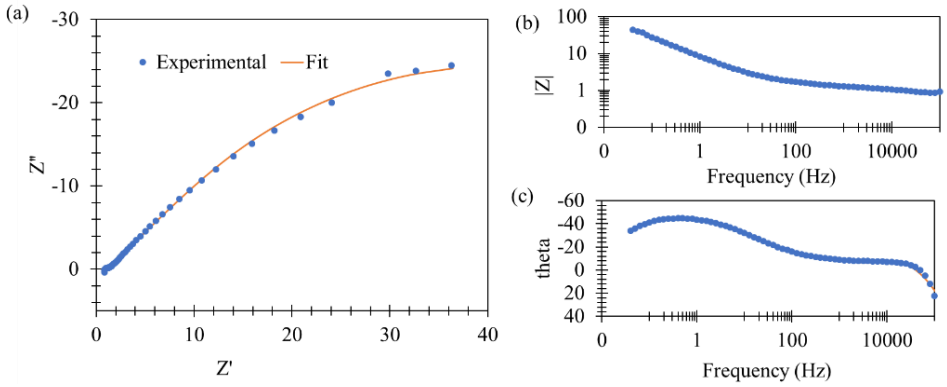


Figure 4.32. Nyquist (a) and Bode Plots (b,c) of Inconel in $Li_2CO_3$-$K_2CO_3$ salt at 552 ˚C after electrochemical impedance spectroscopy measurements. The blue dots represent the experimental data. The orange line represents fitting with the equivalent model; figure 29c.

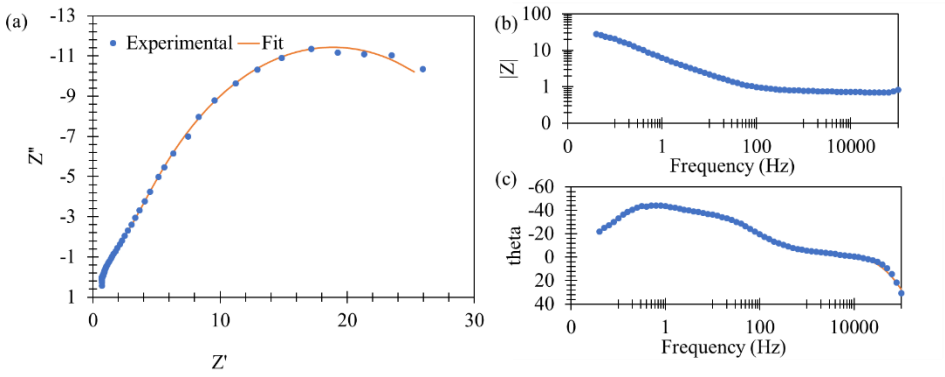


Figure 4.33. Nyquist (a) and Bode Plots (b,c) of Inconel in $Li_2CO_3$-$K_2CO_3$ salt at 577 ˚C after electrochemical impedance spectroscopy measurements. The blue dots represent the experimental data. The orange line represent fitting with the equivalent model; figure 29d.

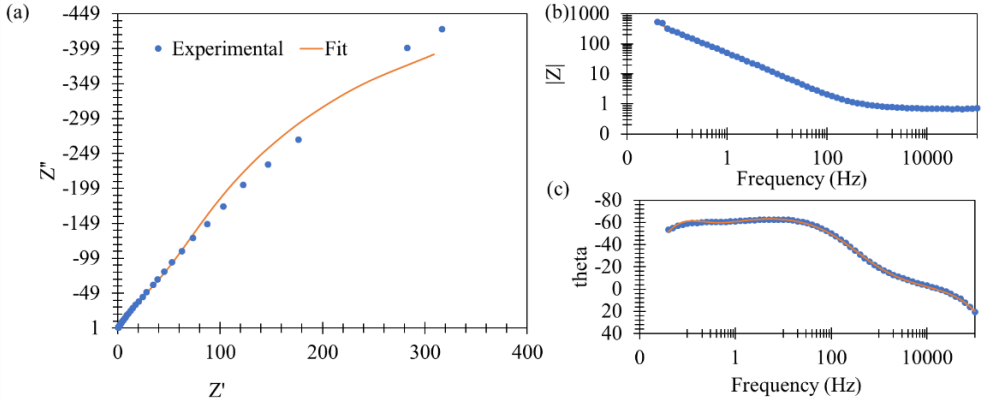


Figure 4.34. Nyquist (a) and Bode Plots (b,c) of Inconel in $Li_2CO_3$-$K_2CO_3$ salt at 600 ˚C after electrochemical impedance spectroscopy measurements. The blue dots represent the experimental data. The orange line represent fitting with the equivalent model; figure 29e.

Table 4.12. EIS fit results using a Voigt circuit with two time constants (one constant phase element and one capacitor) in series with an inductor for modeling the corrosion process of Inconel 600 in molten $Li_2CO_3$-$K_2CO_3$ salt at various temperatures.

| Temperature (°C) | $R_s$ ($\Omega$ $cm^2$) | $T_{co}$ (F $cm^{-2}$)-2 | $P_{co}$-2 | $R_{po}$-2 ($\Omega$ $cm^2$) | $T_{co}$ (F $cm^{-2}$)-1 | $P_{co}$-1 | $R_{po}$-1 ($\Omega$ $cm^2$) | $T_{dl}$ (F $cm^{-2}$) | $P_{dl}$ | $R_{ct}$ ($\Omega$ $cm^2$) | L (H) | W-R | W-T | W-P | Chi Square | SS |
|---|---|---|---|---|---|---|---|---|---|---|---|---|---|---|---|---|
| 600 | 0.671 ± 0.0055 | n/a | n/a | n/a | 7.78E-3 ± 0.019 | n/a | 856 ± 0.032 | 6.26E-3 ± 0.015 | 0.719 ± 0.0040 | 92.5 ± 0.412 | 4.00E-7 ± 0.038 | n/a | n/a | n/a | 0.00192 | 0.233 |
| 577 | 0.669 ± 0.012 | 0.0534 ± 0.022 | 0.784 ± 0.019 | 32.0 ± 0.031 | 0.0463 ± 0.060 | 0.6667 ± 0.021 | 2.43 ± 0.13 | 8.90E-5 ± 0.28 | n/a | 0.0707 ± 0.11 | 5.88E-7 ± 0.028 | n/a | n/a | n/a | 0.00132 | 0.159 |
| 552 | 0.781± 0.015 | n/a | n/a | n/a | 3.27e-5 ± 0.10 | n/a | 0.238 ± 0.048 | 0.0492 ± 0.046 | 0.759 ± 0.035 | 71.2 ± 0.065 | 5.51E-7 ± 0.036 | 5.31 ±0.16 | 0.639 ±0.19 | 0.350 ±0.058 | 0.00122 | 0.147 |
| 527 | 1.20 ± 0.025 | n/a | n/a | n/a | 1.03E-3 ± 0.16 | 0.584 ± 0.030 | 2.02 ± 0.034 | 6.40E-3 ± 0.004 | 0.561 ± 0.003 | 2350 ± 0.058 | 3.51E-7 ± 0.069 | n/a | n/a | n/a | 0.00021 | 0.0252 |
| 501 | 1.44 ± 0.11 | n/a | n/a | n/a | 1.14E-3 ± 0.077 | 0.561 ± 0.0145 | 3.69 ± 0.0221 | 5.97E-3 ± 0.00841 | 0.573 ± 0.00464 | 1059 ± 0.096 | n/a | n/a | n/a | n/a | 0.00011 | 0.0112 |

#### 4.2.3.4 Corrosion mechanism of Inconel 600 in the eutectic salt

Figure 4.35 shows the number of oxide layers on the surface of the Inconel 600 electrode. The white dots represent diffusion through the oxide layer. At 600 °C, there appears to be two oxide years on the surface of the Inconel electrode, which increase to three layers at 577 °C due to the formation of corrosion products. However, the oxide layer is dissolved into the salt at 552 °C. At 527 °C and 501 °C, the outer oxide layer grows thinner whiles the inner oxide layer grows thicker and less permeable to the salt. Oxide layer composition could primarily be $(Ni)Cr_2O_4$ and nickel oxide.

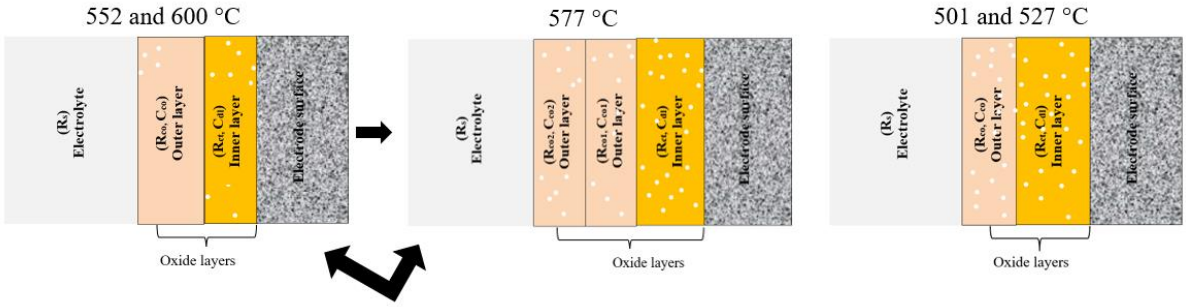


Figure 4.35. Corrosion mechanism for Inconel 600 in molten carbonate $Li_2CO_3$-$K_2CO_3$ salts with varying temperatures of 501 °C, 527 °C, 552 °C, 577 °C and 600 °C, displaying the number of oxide layers formed of the surface of the electrode as modelled by Figure 4.29

### 4.2.4. Summary of Electrochemical Measurements for electrodes in the Eutectic Salt

Stainless steel 304, nickel, and Inconel 600 were tested in $0.67Li_2CO_3$-$0.33K_2CO_3$ molten eutectic salt. Stainless steel 304 exhibited higher resistance to the salt due to the formation of a stable oxide layer, followed by nickel and Inconel 600. The values for the LPR measurements showed significantly higher resistance polarization values for stainless steel 304 in most cases than nickel and Inconel 600. However, at approximately 600 °C, Inconel 600 is more resistant than stainless steel 304 and nickel, suggesting the formation of a more stable oxide layer for Inconel 600. Tafel analysis in the eutectic salt showed much smaller values for the $i_{corr}$ for stainless steel 304 than nickel and Inconel 600. However, at approximately 600 °C, Inconel 600 has the lowest $i_{corr}$ value which is three times less than the values of nickel and five times less than the value of stainless steel 304, showing than Inconel 600 is least affected by the salt at higher temperatures. The

spontaneous decrease and increase of $i_{corr}$ values of nickel and Inconel 600 indicate a cycle of active, passive and transpassive corrosion. P values from the EIS run showed a much stable and less permeable oxide layer for stainless steel 304 except at 600 °C as a result of diffusion of charge carries through the oxide layer. Inconel performed better at 600 °C temperature with high $P_{dl}$ values, as well as nickel. Overall, stainless steel 304 performed generally well in the salt than nickel and Inconel 600. However, at high temperatures, Inconel 600 does a better job.

## 4.3. Electrochemical Study in Eutectic Carbonate-GDC Composite Salt

### 4.3.1. Electrochemical Study of Stainless Steel in molten Eutectic Carbonate Salts

#### 4.3.1.1. LPR measurement fr stainless steel 304 in the eutectic salt

Figure 4.36 shows temperature measurements at 600 ˚C, 576 ˚C and 552 ˚C grouped towards the bottom of the plot, and 528 ˚C and 502 ˚C grouped towards the top of the plot, showing a huge difference in potential difference between the two groups. The slope for 502 ˚C and 528 ˚C at the point where the current is zero is much steeper than at 522 ˚C, 576 ˚C, and 603 ˚C. The values for $R_p$ at 603 ˚C, 576 ˚C and 552 are in proximity. However, at 528 ˚C and 502 ˚C, the values of $R_p$ are significantly larger. As temperature increases, the $R_p$ value reduces, and at lower temperatures $R_p$ is very high as seen in Table 4.13. At 603 ˚C; when the electrode is first introduced into the salt, an oxide layer is formed on the surface of the electrode. The oxide layer is thin and begins to show dissolution in the salt. Thus, a decrease in $R_p$ values at 576 ˚C. However, the $R_p$ increases at 576 ˚C and then very rapidly at 552 ˚C, and more rapidly at 502 ˚C. This suggests that as the temperature decreases, the protective oxide layer is more stable and the electrode is more resistive to the salt. The OCP values shift from more cathodic values to less cathodic values as $R_p$ increases, with a very significant increase in OCP from 552 ˚C to 528 ˚C.

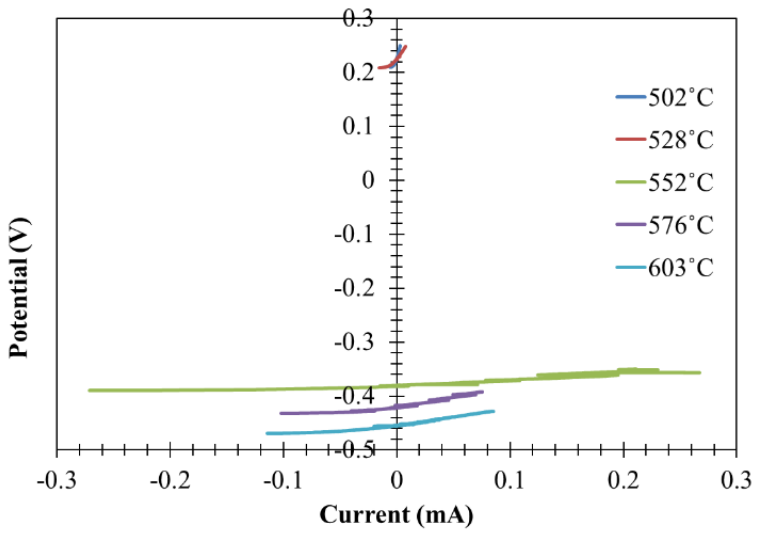


Figure 4.36. Linear polarization resistance of stainless steel 304 in composite salt showing a scanning potential range of -20mV to 20mV respectively at various temperatures.

Table 4.13. Polarization resistance ($R_p$) for stainless steel 304 with surface area of 54.5 $mm^2$ in $Li_2CO_3$-$K_2CO_3$ salt at 502 °C, 528 °C, 552 °C, 576°C and 603 °C to determine polarization resistance.

| Temperature (˚C) | Rp (Ohms.$cm^2$) | OCP (mV) |
|---|---|---|
| 502 | 3871.7 | 226.4 |
| 528 | 1354.9 | 224.8 |
| 552 | 180.4 | -381.1 |
| 576 | 115.0 | -422.2 |
| 603 | 155.9 | -454.9 |

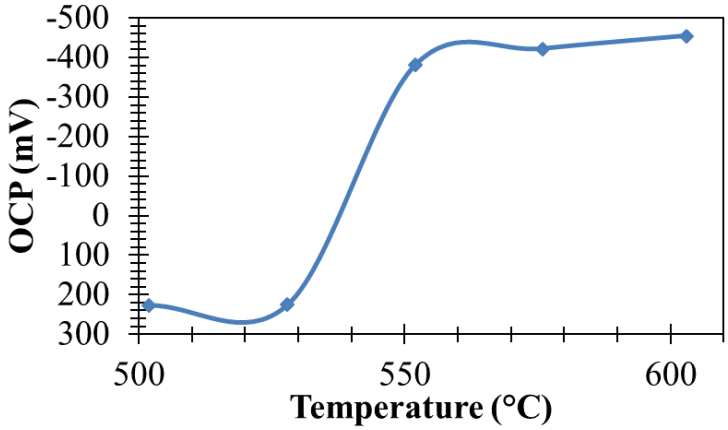


Figure 4.37. Open circuit potential versus temperature for stainless steel for LPR measurement 502 °C, 528 °C, 552 °C, 576°C and 603 °C

#### 4.3.1.2. Tafel measurements of Stainless steel 304 in GDC composite salt

Figure 4.38 show a separation of Tafel plots into two groups, one set towards the top portion of the plot area and the other group towards the bottom of the plot area. This same trend is seen on the LPR plot (see Figure 4.36). An interesting pattern can be seen in the values of the anodic slope. As temperature decreases, there is an alternating increase and decrease in the $b_a$ values. This suggests the simultaneous breakdown and formation of the oxide layer. However, the dissolution of the oxide layer is accelerated at 603 ˚C, 576 ˚C and 552 ˚C as corroborated by the more cathodic

values of the OCP at these temperatures (see Table 4.14). There are prominent spikes on the anodic curves, suggesting a vigorous break down at 604 ˚C. This pattern continues for 576 ˚C and 552 ˚C. At 528 ˚C and 502 ˚C, the spikes are less prominent with more anodic OCP values (see Table 4.14), suggesting the formation of a stable oxide layer on the electrode.

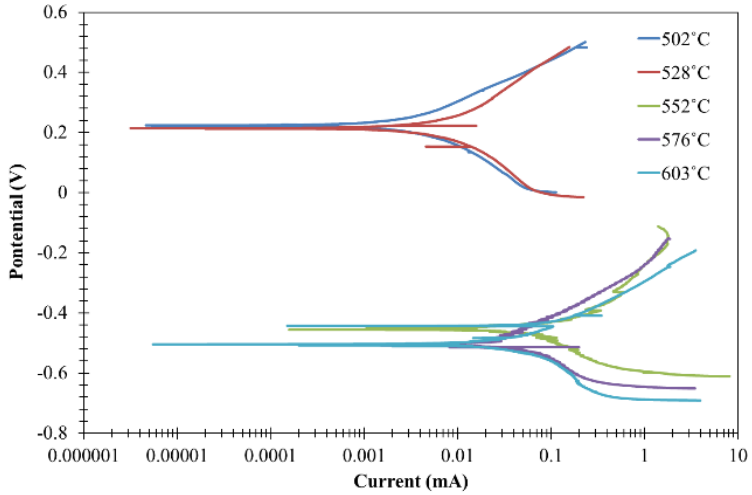


Figure 4.38. Polarization curves for stainless steel 304 in composite $Li_2CO_3$-$K_2CO_3$ at 502 °C, 528 °C, 552 °C, 576°C and 603 °C, respectively, conducted at a potential range of -0.25V to 0.25V vs OCP.

Table 4.14. Cathodic beta ($b_c$) and anodic beta ($b_a$) constants from Tafel plots for stainless steel 304 and calculated corrosion current density ($i_{corr}$) and corrosion rate (CR) for stainless steel 304 using the $R_p$, $b_a$, and $b_c$, 502 °C, 528 °C, 552 °C, 576°C and 603 °C

| Temperature (˚C) | bc (mV) | ba (mV) | OCP (mV) | $i_{corr}$ ($\mu A/cm^2$) | CR (mm/yr) |
|---|---|---|---|---|---|
| 502 | 179 | 162 | 224 | 9.52 | 0.0994 |
| 528 | 270 | 255 | 214 | 42 | 0.439 |
| 552 | 216 | 158 | -453 | 220.2 | 2.29 |
| 576 | 130 | 205 | -507 | 300.9 | 3.14 |
| 603 | 183 | 143 | -500 | 223.9 | 2.34 |

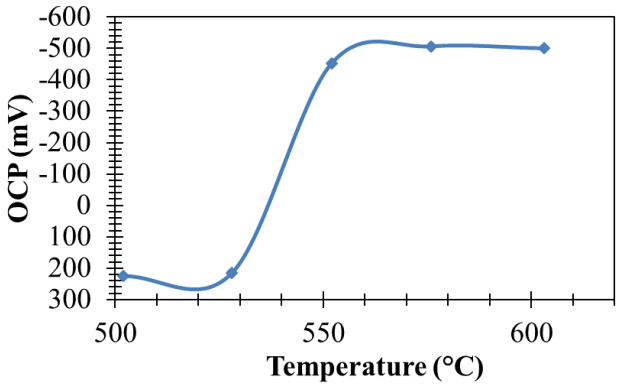


Figure 4.39. Open circuit potential versus temperature for stainless steel 304 for Tafel measurement 502 °C, 528 °C, 552 °C, 576°C and 603 °C

#### 4.3.1.3. EIS Measurements of Stainless Steel 304 in the composite salt

Figure 4.40 shows the equivalent circuits for fitting the experimental data of stainless steel in the molten salt shown in Figure 4.41 to Figure 4.44. Figure 4.40 is a Voigt circuit with two time constants. Figure 4.40 a however, is in series with and inductor and a Warburg element. Figure 4.40 b is in series with just an inductor. There is a peak at low frequency and a peak at high frequency, representing time constants. However, the peak at high frequency migrates from high frequency to midrange frequency as the temperature decreases. At 502 ˚C, there is a 45 degree line at high frequency on the Nyquist plot, suggesting a diffusing controlled process and hence the presence of a Warburg element. The impedance on the impedance frequency plot increases as temperature decreases. The $P_{dl}$ value in Table 4.15 are close to 1 as the temperature decreases, suggesting an impermeable oxide layer to the electrolyte, thus, corroborating the $R_{ct}$ vales. As temperature increases, $R_{ct}$ increases but $R_{po}$ increases. At higher temperatures, the outer layer of the oxide is less resilient than the inner layer of the oxide as seen by the trend of $R_{po}$ and $R_{ct}$.

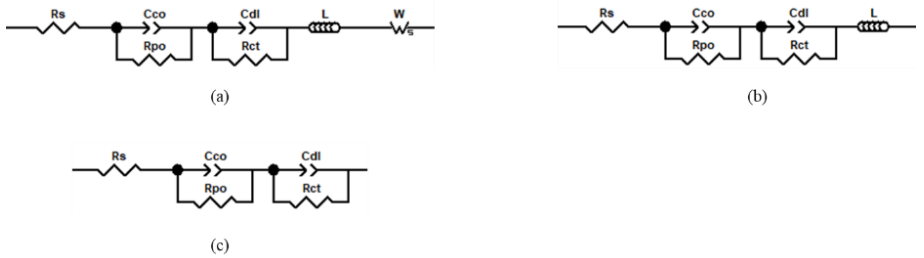


Figure 4.40. Equivalent circuits for fitting bode and Nyquist data of stainless steel for 502˚C, 528˚C, 552˚C, 576˚C and 603˚C.(a) Voigts circuit with two time constants in series with an inductor and a finite length Warburg for fitting of 502˚C. (b) Voigts circuit with two time constants in series with an inductor for fitting 528˚C, 575˚C and 603˚C (c) Voigts circuit with two time constants

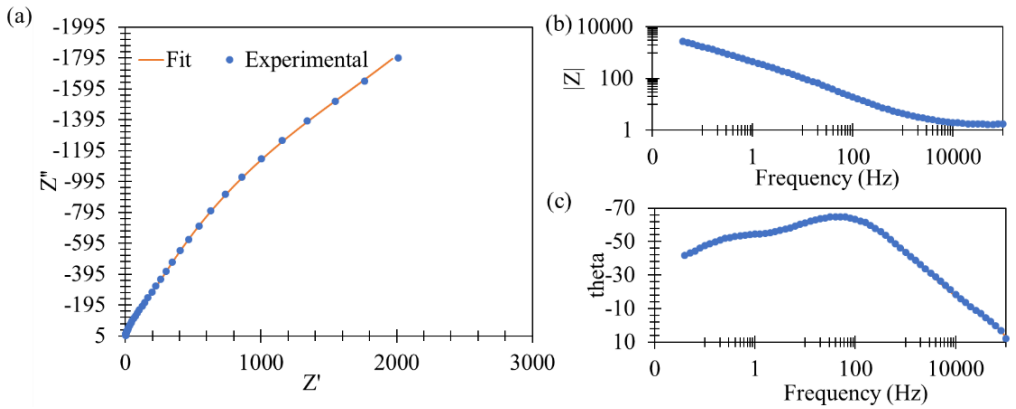


Figure 4.41. Nyquist (a) and Bode Plots (b,c) of stainless steel in composite $Li_2CO_3$-$K_2CO_3$ salt at 502 ˚C after electrochemical impedance spectroscopy measurements. The blue dots represent the experimental data. The orange line represent fitting with the equivalent model; figure 39a.

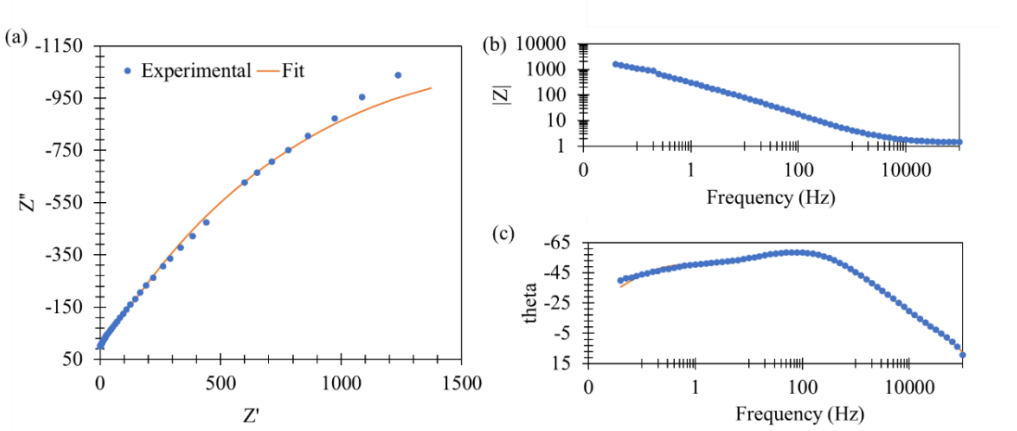


Figure 4.42. Nyquist (a) and Bode Plots (b,c) of stainless steel in composite $Li_2CO_3$-$K_2CO_3$ salt at 528 ˚C after electrochemical impedance spectroscopy measurements The blue dots represent the experimental data. The orange line represents fitting with the equivalent model; figure 39b.

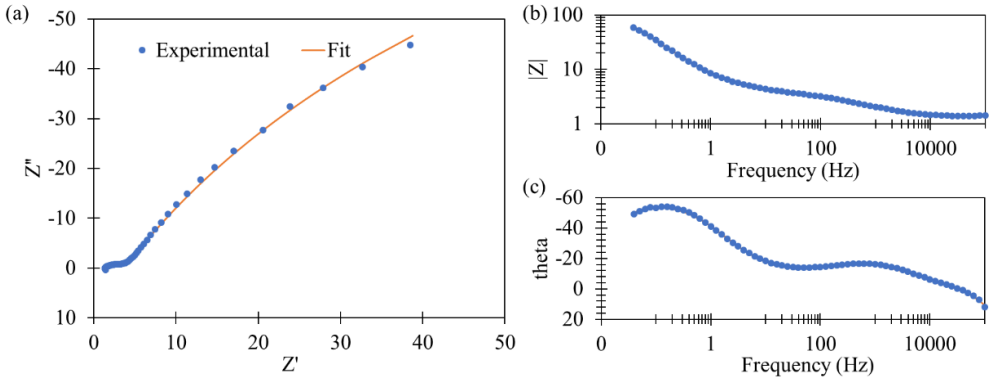


Figure 4.43. Nyquist (a) and Bode Plots (b,c) of stainless steel in composite $Li_2CO_3$-$K_2CO_3$ salt at 576 ˚C after electrochemical impedance spectroscopy measurements. The blue dots represent the experimental data. The orange line represents fitting with the equivalent model; figure 39b.

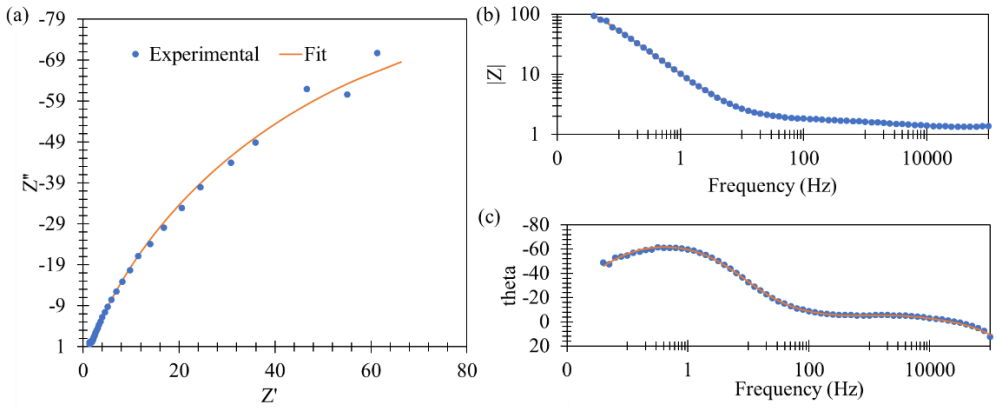


Figure 4.44. Nyquist (a) and Bode Plots (b,c) of stainless steel in composite $Li_2CO_3$-$K_2CO_3$ salt at 603 ˚C after electrochemical impedance spectroscopy measurements. The blue dots represent the experimental data. The orange line represents fitting with the equivalent model; figure 39b.

Table 4.15. Best fit values for various temperatures using appropriate equivalent circuits for stainless steel in composite $Li_2CO_3$-$K_2CO_3$ salt at 502˚C, 528˚C, 552˚C, 576˚C and 603˚C.

| Temperature (°C) | $R_s$ (Ω $cm^2$) | $T_{co}$ ($\Omega^{-1}S^{-p}cm^{-2}$)-1 | $P_{co}$ -1 | $R_{po}$ -1 (Ω $cm^2$) | $T_{dl}$ ($\Omega^{-1}S^{-p}cm^{-2}$) | $P_{dl}$ | $R_{ct}$ (Ω $cm^2$) | L (H) | W-R | W-T | W-P | Chi Square | SS |
|---|---|---|---|---|---|---|---|---|---|---|---|---|---|
| 603 | 0.720±0.007 | 5.72E-3±0.3 | 0.692±0.05 | 0.270±0.04 | 0.448±0.004 | 0.790±0.002 | 118±0.0189 | 4.43E-7±0.04 | | n/a | n/a | 0.0008 | 0.1 |
| 576 | 0.720±0.005 | 8.56E-3±0.06 | 0.608±0.01 | 1.40±0.01 | 7.61E-2±0.004 | 0.732±0.004 | 132±0.0436 | 4.91E-7±0.03 | | n/a | n/a | 0.0005 | 0.06 |
| 528 | 0.739±0.01 | 2.31E-3±0.1 | 0.816±0.05 | 23.4±0.19 | 1.92E-3±0.01 | 0.667±0.009 | 1964±0.03 | 5.09E-7±0.07 | | n/a | n/a | 0.001 | 0.2 |
| 502 | 0.855±0.001 | 1.04E-3±0.06 | 0.926±0.05 | 50.5±0.241 | 1.48E-3±0.05 | 0.760±0.04 | 3120±0.08 | 5.07E-7±0.06 | 87.7±0.279 | 1.30± 0.121 | 0.562±0.0135 | 0.0009 | 0.1 |

#### 4.2.3.4 Corrosion mechanism of Stainless Steel 304 in the composite GDC salt

Figure 4.45 shows that at 600 to 528 °C, there are two oxide layers on the surface of the electrode. The outer layer appears thinner at the initial temperatures whereas the inner layer was thicker. However, at 502 °C, the inner layer is almost the same thickness as the outer layer indicating the breakdown or diffusion of corrosion products through the first layer into the second and then into the salt.

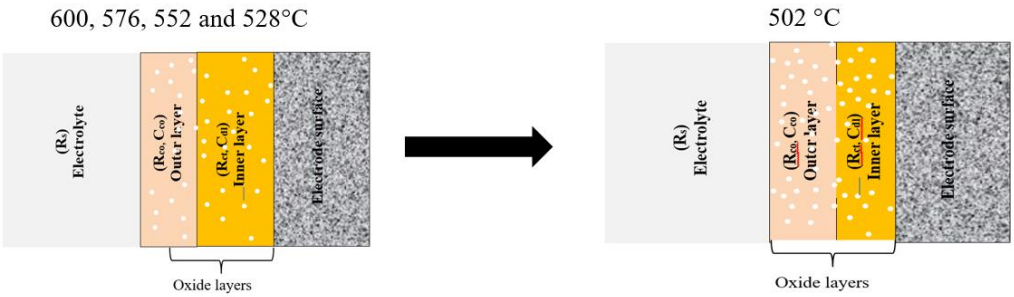


Figure 4.45. Corrosion mechanism for stainless steel 304 in molten carbonate 0.3 GDC – 0.7 ($0.67Li_2CO_3$-$0.33K_2CO_3$) salts with varying temperatures of 502 °C, 528 °C, 552 °C, 576 °C and 600 °C, displaying the number of oxide layers formed of the surface of the electrode as modelled by Figure 4.40

### 4.3.2. Electrochemical Study Nickel in molten Eutectic Carbonate Salts

#### 4.3.2.1. Linear Polarization Resistance measurement in the composite salt

Figure 4.46 shows the resistance polarization of Ni at various temperatures. The slopes at the at the near zero current region is less steep as the temperature decreases. This phenomenon corresponds to the resistance polarization of Ni in the composite salt (See Table 4.16). This implies that for Ni in composite salt under the conditions run, it is less resistant to the composite salt as the temperature increases shown by the $R_p$ values seen in Table 4.16. 497 ˚C has the steepest slope and hence the largest resistance. 597 ˚C has the least steep slope and hence the least resistance. The OCP decreases from less cathodic values to more cathodic values as the temperature increases. The current range associated with each potential sweep increases as the temperature increases, 497 ˚C with the least range and 597 ˚C with the most range. Looking at each LPR temperature plot, little spike can be seen on them. This is evidence of the breakdown and reformation of the protective layer formed during the corrosion process. At 575 ˚C the spikes are observed to be predominant meaning the corrosion of the material is aggressive, hence a vigorous breakdown of the protective layer. This is evident in the increase of OCP from a more cathodic to a less cathodic value at 597 ˚C. The deviation of OCP to a less cathodic value indicates the formation of a protective layer on the surface of the Ni. A visual representation of this can be seen in Figure 4.47.

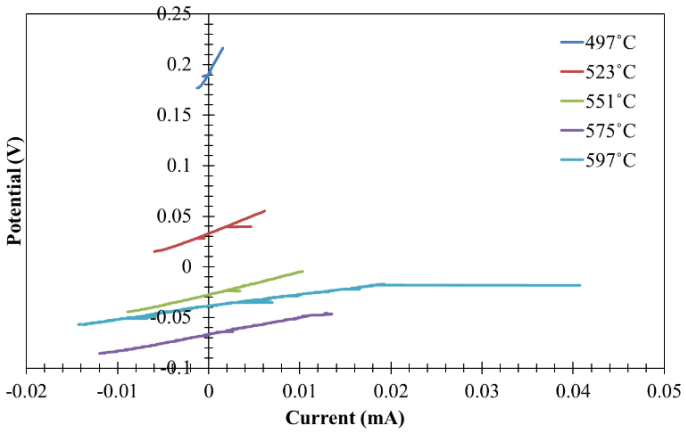


Figure 4.46. Linear polarization resistance of Ni in $Li_2CO_3$-$K_2CO_3$ showing a scanning potential range of -20mV to 20mV at 497 °C, 523 °C, 551 °C, 575°C and 597 °C, to determine the polarization resistance, $R_p$.

Table 4.16. Polarization resistance ($R_p$) for Ni with surface area of 52.04 $mm^2$ in composite $Li_2CO_3$-$K_2CO_3$ salt at 497 °C, 523 °C, 551 °C, 575°C and 597 °C.

| Temperature (˚C) | Rp (Ohms.$cm^2$) | OCP (mV) |
|---|---|---|
| 497 | 9209.5 | 191.00 |
| 523 | 1840.7 | 33.20 |
| 551 | 1199 | -27.00 |
| 575 | 1129.3 | -66.70 |
| 597 | 590.7 | -38.40 |

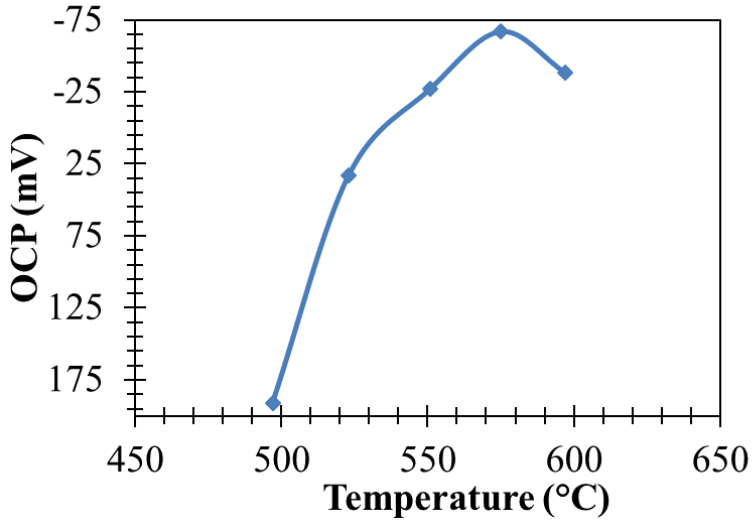


Figure 4.47. Open circuit potential versus temperature for Ni for LPR measurement in composite $Li_2CO_3$-$K_2CO_3$ salt at 497 °C, 523 °C, 551 °C, 575°C and 597 °C.

#### 4.3.2.2. Tafel measurements for nickel in molten composite salt

The Tafel plots in Figure 4.48 gives an in-depth view of the corrosion mechanisms that take place when the electrode is introduced into the salt. From Figure 4.48, there is a decrease in the anodic slope from 597 ˚C to 551 ˚C, and an increase from 551 ˚C to 497 ˚C. This suggest that after the electrode was introduced to the salt at 597 ˚C, a protective scale was quickly formed to prevent the material from corroding. However, the reduction of the anodic slope values indicates that the dissolution of the protective into the salt, and this is evident by the spikes shown in the anodic curves of the 575 ˚C and 551 ˚C. More evident spikes are seen at 523 ˚C, and an increase in anodic slope value suggest the continuous formation of a more stable oxide layer of the Ni electrode. At 497 ˚C the spikes seen are not profound and this indicates a stable layer or oxide and a decreased rate of dissolution of the oxide layer into the salt. This is corroborated by the shift of OCP values from more cathodic values to less cathodic values as temperature decreases (Table 4.17 and Figure 4.49). The $i_{corr}$ correlates closely with the corrosion rate. As it can be seen from the values in table 2, the larger the $i_{corr}$, the more profound the corrosion rate. 597 ˚C has the largest corrosion rate. For Ni, the corrosion rate generally increases as temperature increases. The significant change in $i_{corr}$ and the corrosion rate from 597 ˚C to 575 ˚C suggests that at 597 ˚C corrosion is very aggressive, and then slows down at 575 ˚C. The reduction in corrosion rate suggest the formation or an oxide layer on the surface of the nickel. The oxide layer becomes somewhat stable as observed in the decrease in the corrosion rate at 551 ˚C. However, at 523 ˚C, there appears to be a dissolution of the oxide layer in the salt as seen with the increase in corrosion rate. This is however hindered by the formation of a stable layer and hence the reduction of the corrosion rate at 497 ˚C.

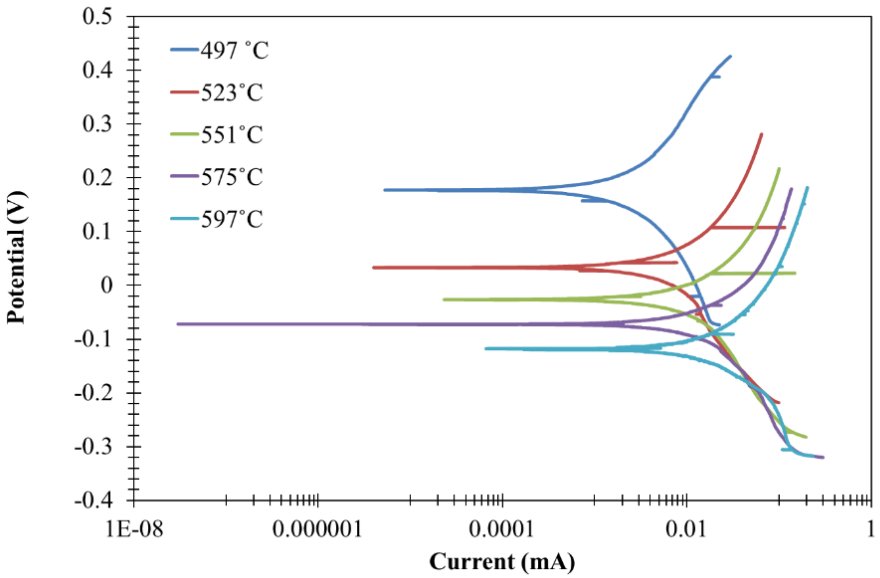


Figure 4.48. Polarization curves for nickel in composite $Li_2CO_3$-$K_2CO_3$ at 497 °C, 523 °C, 551 °C, 575°C and 597 °C, respectively, conducted at a potential range of -0.25V to 0.25V vs OCP.

Table 4.17. Cathodic beta ($b_c$) and anodic beta ($b_a$) constants from Tafel plots for nickel and calculated corrosion current density ($i_{corr}$) and corrosion rate (CR) for nickel using the $R_p$, $b_a$, and $b_c$ in composite $Li_2CO_3$-$K_2CO_3$ salt at 497 °C, 523 °C, 551 °C, 575°C and 597 °C.

| Temperature (˚C) | bc (mV) | ba (mV) | OCP (mV) | $i_{corr}$ ($\mu A/cm^2$) | CR (mm/yr) |
|---|---|---|---|---|---|
| 497 | 486 | 437 | 177 | 20.6 | 0.22 |
| 523 | 561 | 408 | 33.2 | 55.7 | 0.6 |
| 551 | 309 | 215 | -23.2 | 45.9 | 0.49 |
| 575 | 351 | 242 | -69.6 | 55 | 0.59 |
| 597 | 492 | 506 | -111 | 183.3 | 1.96 |

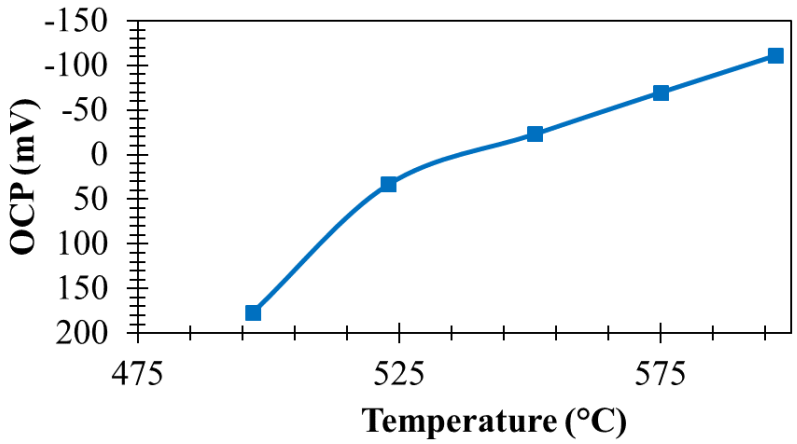


Figure 4.49. Open circuit potential versus temperature for nickel during Tafel measurement run in composite $Li_2CO_3$-$K_2CO_3$ salt at 497 °C, 523 °C, 551 °C, 575°C and 597 °C.

#### 4.3.2.3. EIS measurements for Nickel in composite salt

Figure 4.50 shows the equivalent circuit for fitting the experimental data found in Figure 4.51 to Figure 4.55. Figure 4.50 comprises of a resistor in series with a a parallel combination of a capacitor and resistor; which is in series with a parallel combination of a capacitor and resistor, altogether in series with an inductor. There's a peak at peak at mid frequency on the frequency-theta plot. Both $R_{ct}$ and $R_{po}$ decrease with increasing temperature (see Table 4.18). However, the high values of these resistance suggest that the oxide layer is more stable oxide layer. The capacitance also follows a similar trend of decreasing as the temperature decreases. However, the capacitance do not differ significantly from each other, suggesting a more gradual break down of the oxide layer. Nevertheless, the resistance are pretty high at all temperatures owing to the excellent ability of nickel to prevent corrosion.

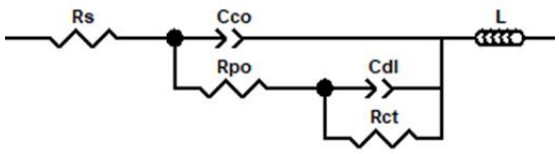


Figure 4.50. Equivalent circuits for fitting bode and Nyquist data of Ni for 501˚C, 527˚C, 552˚C, 577˚C and 600˚C. in composite $Li_2CO_3$-$K_2CO_3$ salt at various temperatures.

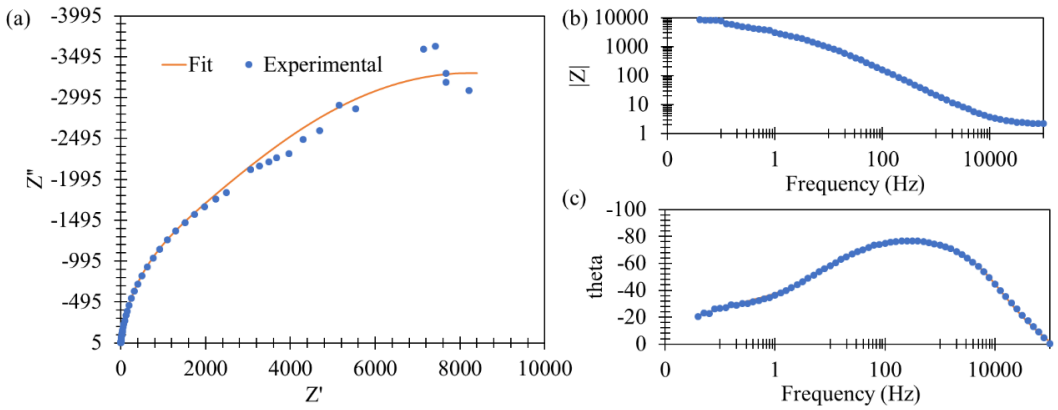


Figure 4.51. Nyquist (a) and Bode Plots (b,c) of nickel in composite Li2CO3-K2CO3 salt at 497 ˚C after electrochemical impedance spectroscopy measurements. The blue dots represent the experimental data. The orange line represent fitting with the equivalent model; figure 48.

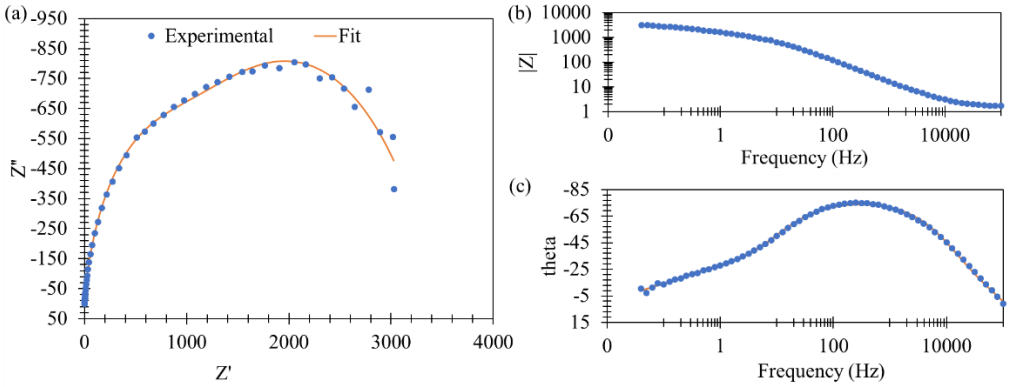


Figure 4.52. Nyquist (a) and Bode Plots (b,c) of nickel in composite $Li_2CO_3$-$K_2CO_3$ salt at 523 ˚C after electrochemical impedance spectroscopy measurements. The blue dots represent the experimental data. The orange line represent fitting with the equivalent model; figure 48.

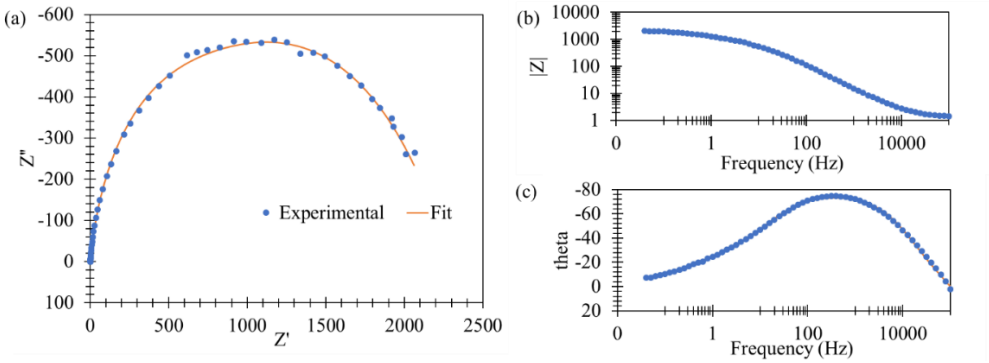


Figure 4.53. Nyquist (a) and Bode Plots (b,c) of nickel in composite $Li_2CO_3$-$K_2CO_3$ salt at 551 ˚C after electrochemical impedance spectroscopy measurements. The blue dots represent the experimental data. The orange line represent fitting with the equivalent model; figure 48.

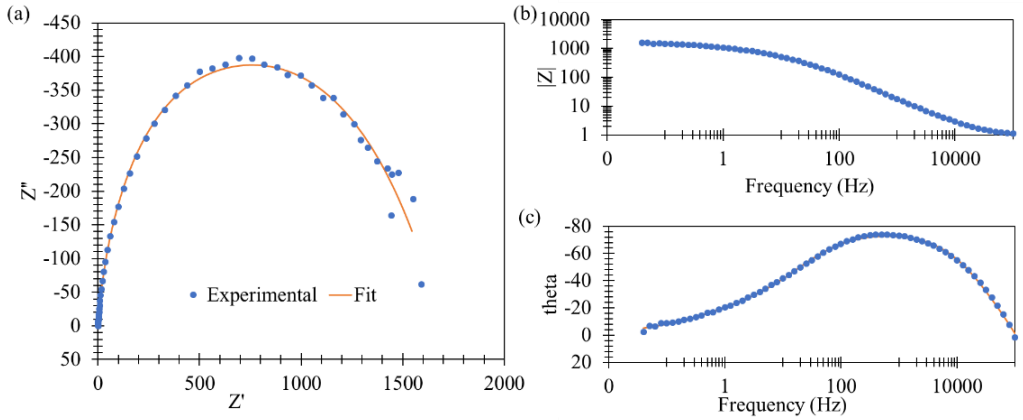


Figure 4.54. Nyquist (a) and Bode Plots (b,c) of nickel in composite $Li_2CO_3$-$K_2CO_3$ salt at 575 ˚C after electrochemical impedance spectroscopy measurements. The blue dots represent the experimental data. The orange line represent fitting with the equivalent model; figure 48.

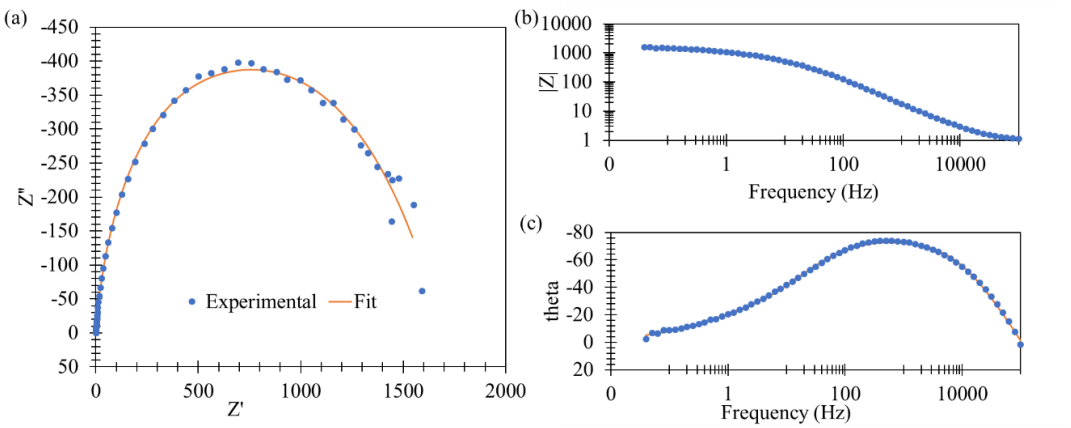


Figure 4.55. Nyquist (a) and Bode Plots (b,c) of nickel in composite $Li_2CO_3$-$K_2CO_3$ salt at 597 ˚C after electrochemical impedance spectroscopy measurements. The blue dots represent the experimental data. The orange line represent fitting with the equivalent model; figure 48.

Table 4.18. Best fit values for Nickel in composite $Li_2CO_3$-$K_2CO_3$ salt at 497 °C, 523 °C, 551 °C, 575°C and 597 °C using equivalent circuit (figure 49) to describe electrode kinetics during immersion in salt

| Temperature (°C) | $R_s$ ($\Omega$ cm$^2$) | $T_{co}$ ($\Omega^{-1}S^{-p}cm^{-2}$)-1 | $P_{co}$ -1 | $R_{po}$ -1 ($\Omega$ cm$^2$) | $T_{dl}$ ($\Omega^{-1}S^{-p}cm^{-2}$) | $P_{dl}$ | $R_{ct}$ ($\Omega$ cm$^2$) | L (H) | Chi Square | SS |
|---|---|---|---|---|---|---|---|---|---|---|
| 497 | 1.13 ± 0.009 | 3.97E-5 ± 0.02 | 0.886 ± 0.003 | 990 ± 0.08 | 2.87E-4 ± 0.03 | 0.507 ± 0.05 | 7356 ± 0.10 | 4.47E-7 ± 0.13 | 0.002 | 0.2 |
| 523 | 0.869 ± 0.006 | 5.98E-5 ± 0.01 | 0.866 ± 0.002 | 629 ± 0.03 | 6.10E-4 ± 0.03 | 0.640 ± 0.03 | 1171 ± 0.03 | 4.36E-7 ± 0.06 | 0.0008 | 0.09 |
| 551 | 0.746 ± 0.007 | 6.33E-5 ± 0.02 | 0.866 ± 0.002 | 428± 0.04 | 6.52E-4 ± 0.03 | 0.575 ± 0.04 | 762± 0.05 | 4.37E-7 ± 0.06 | 0.0009 | 0.1 |
| 575 | 0.835 ± 0.007 | 5.83E-5 ± 0.02 | 0.861 ± 0.002 | 312 ± 0.05 | 7.06E-4 ± 0.04 | 0.537 ± 0.04 | 567± 0.04 | 4.94E-7 ± 0.04 | 0.0008 | 0.09 |
| 597 | 0.374 ± 0.01 | 5.68E-5 ± 0.02 | 0.819 ± 0.003 | 89.7 ± 0.02 | 1.06E-3 ± 0.02 | 0.647 ± 0.02 | 527 ± 0.01 | 7.15E-7 ± 0.03 | 0.0008 | 0.09 |

### 4.2.3.4 Corrosion mechanism of Nickel in the composite GDC salt

Figure 4.56 shows the corrosion mechanism for the nickel electrode in the GDC composite salts in terms on oxide layer versus change in temperature. It can be seen that the oxide layer on the nickel electrode remains the same throughout the experiment indication a very resistant impermeable oxide layer.

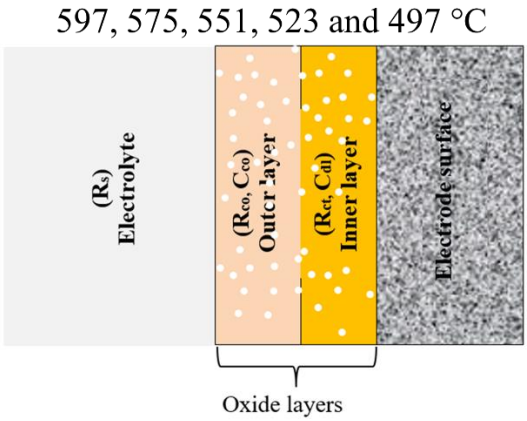


Figure 4.56. Corrosion mechanism for nickel in molten carbonate 0.3 GDC – 0.7 ($0.67Li_2CO_3$-$0.33K_2CO_3$) salts with varying temperatures of 497 °C, 523 °C, 551 °C, 575 °C and 597 °C, displaying the number of oxide layers formed of the surface f the electrode as modelled by Figure 4.50.

### 4.3.3. Electrochemical Study Inconel 600 in molten Eutectic Carbonate Salts

#### 4.3.3.1. Linear polarization resistance of Inconel 600 in composite salt

Figure 4.57 shows the linear polarization measurements for Inconel in the composite salt. 600 ˚C is more cathodic with regards to OCP (Figure 4.58) in comparison with the other temperatures. As temperature increases, the slope at the zero current regions gets steeper (see Figure 4.57). There is a general increase in $R_p$ as temperature increases which is a opposite of the trend shown by the stainless steel. Suggesting an increase in resistance to the molten salt as temperature increases. This is corroborated with the current range during the potential sweep from low temperatures to high temperature. However, at 523 ˚C there is a dramatic decrease in $R_p$ and then an increase in at 502 ˚C. This is attributed to the breakdown and formation of the oxide layer during the temperature transition from 523 ˚C to 502 ˚C (see Table 4.19). The OCP values approach higher cathodic values as temperature increases. The presence of the GDC in the salt and the high Cr content in Inconel 600 plays a role in inhibiting corrosion.

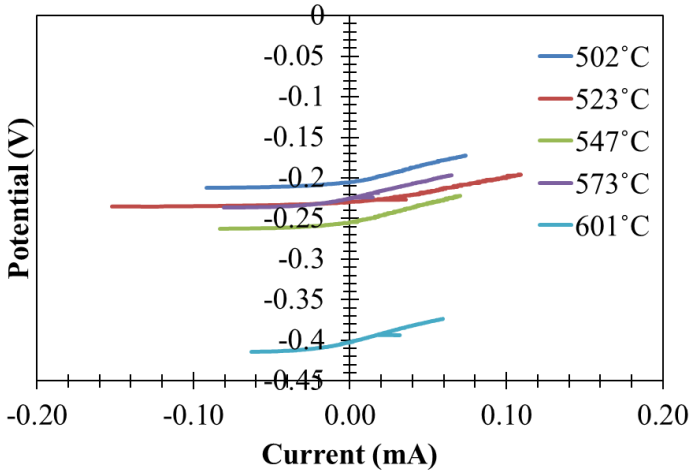


Figure 4.57. Linear polarization resistance of Inconel in composite salt showing a scanning potential range of -20mV to 20mV respectively at 502 °C, 528 °C, 543 °C, 573°C and 601 °C in composite $Li_2CO_3$-$K_2CO_3$.

Table 4.19. Polarization resistance ($R_p$) for Inconel with surface area of 100.4 $mm^2$ in composite $Li_2CO_3$-$K_2CO_3$ salt at 502 °C, 528 °C, 543 °C, 573°C and 601 °C

| Temperature (˚C) | Rp (Ohms.$cm^2$) | OCP(mV) |
|---|---|---|
| 502 | 250.1 | -205.00 |
| 523 | 158.2 | -230.00 |
| 547 | 353.4 | -245.00 |
| 573 | 418.5 | -225.00 |
| 601 | 457.1 | -402.00 |

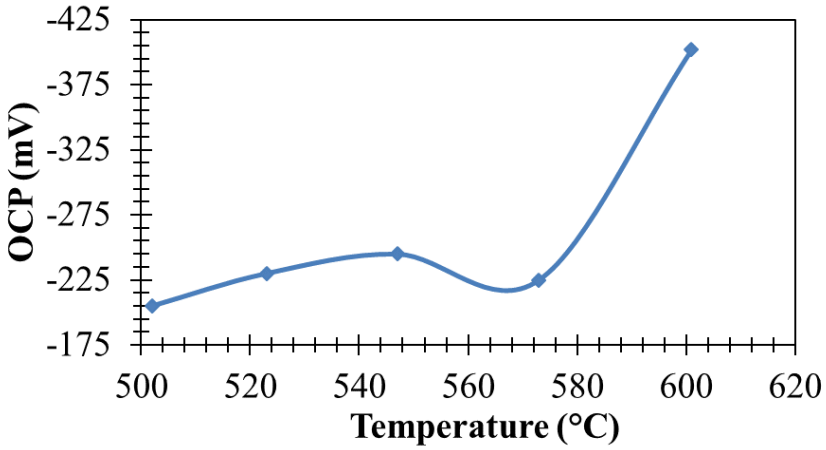


Figure 4.58. Open circuit potential versus temperature for Inconel 600 during LPR measurement run in in $Li_2CO_3$-$K_2CO_3$ salt at 502 °C, 528 °C, 543 °C, 573°C and 601 °C.

### 4.3.3.2. Tafel measurements of Inconel 600 in composite salt

Figure 4.59 shows the Tafel measurements for Inconel at various temperatures in the composite salt. Looking at the anodic curves which correspond with the formation of the oxide layer, at 601 ˚C when the electrode is inserted into the melt, there is an immediate formation of oxide layer due to the Cr rich content in the salt. However, as the electrode remains in the salt, the thin film of oxide begins to breakdown and is evident on the anodic curve at 601 ˚C. The spikes and shift in the curve at about -300 mV suggest a breakdown in oxide layer. At 573 ˚C the breakdown is more severe as prominent spikes can be seen on the anodic curve as well as little spikes at the shift in anodic curve at about -100 mV. This phenomenon suggests an accelerated corrosion process. This same trend is seen as the temperature decreases and more spikes appear on the anodic curve of 543 ˚C, 523 ˚C and 502 ˚C. $I_{corr}$ generally increases with increasing temperature. As $i_{corr}$ increases the corrosion of the alloy is accelerated as seen in Table 4.20. The corrosion rate of the alloy is accelerated as the temperature decreases and in hindered as the temperature increases.

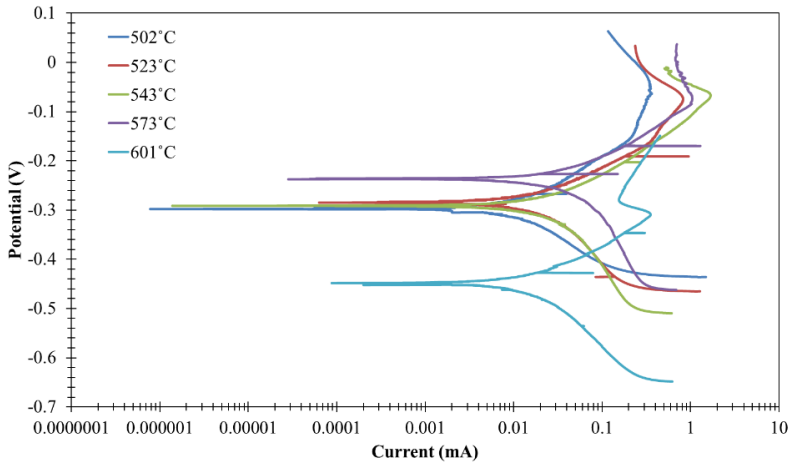


Figure 4.59. Polarization curves for Inconel 600 in composite $Li_2CO_3$-$K_2CO_3$ at 502 °C, 528 °C, 543 °C, 573°C and 601 °C, respectively, conducted at a potential range of -0.25V to 0.25V vs OCP.

Table 4.20. Cathodic beta ($b_c$) and anodic beta ($b_a$) constants from Tafel plots for Inconel 600 and calculated corrosion current density ($i_{corr}$) and corrosion rate (CR) for Inconel 600 using the $R_p$, $b_a$, and $b_c$ in composite $Li_2CO_3$-$K_2CO_3$ salt at 502 °C, 528 °C, 543 °C, 573°C and 601 °C.

| Temperature (˚C) | bc (mV) | ba (mV) | OCP (mV) | $i_{corr}$ (μA/cm$^2$) | CR (mm/yr) |
|---|---|---|---|---|---|
| 502 | 126 | 112 | -297 | 103.4 | 1.05 |
| 523 | 214 | 105 | -282 | 197.8 | 1.97 |
| 547 | 214 | 100 | -289 | 84.7 | 0.86 |
| 573 | 267 | 113 | -237 | 82.7 | 0.84 |
| 601 | 177 | 110 | -452 | 64.9 | 0.66 |

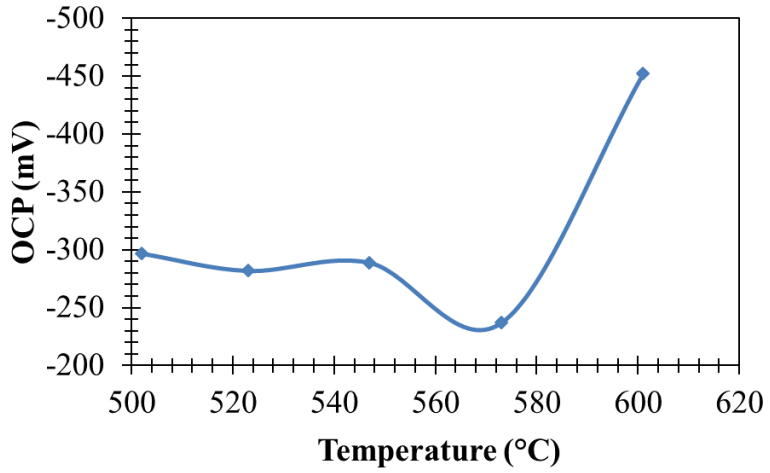


Figure 4.60. Open circuit potential versus temperature for Inconel 600 during Tafel measurement run in composite $Li_2CO_3$-$K_2CO_3$ salt at 502 °C, 528 °C, 543 °C, 573°C and 601 °C.

#### 4.3.3.3. EIS of Inconel 600 in composite salt

Figure 4.61 shows the equivalent circuit used to fit the EIS data for Inconel 600 in Figure 4.62 to Figure 4.66. Figure 4.61a and b are Voigt circuits with two time constants. Figure 4.61a in series with a Warburg element. However, Figure 4.61b is in series with an inductor and a Warburg element. On the other hand, Figure 4.61c is a simple Randles circuit in series with an inductor and Warburg element. The presence of a Warburg element could suggest an instable oxide later or a diffusion controlled reaction. From the frequency-impedance Bode plot, it can be seen that 504 ˚C and 601

˚C have the very resistance values. A close look at table Table 4.21 shows a value of 2707 Ω.cm$^2$ for $R_{po1}$ at 502 ˚C and 1165 ˚C for $R_{ct}$ for 600 ˚C suggesting a very stable oxide layer in contact with the salt. $P_{dl}$ is also very close to 1 adding to the fact that the oxide layer is less permeable to the molten salt even at high temperatures.

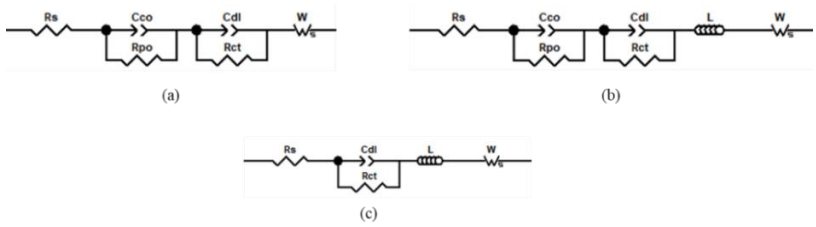


Figure 4.61. Equivalent circuits for fitting bode and Nyquist data of Inconel for 502˚C, 523˚C, 547˚C, 573˚C and 601˚C.(a) equivalent circuit for fitting of 502˚C, (b) equivalent circuit for fitting of 523˚C, 547˚C, and 573˚C. (c) equivalent circuit for fitting of 601˚C in composite $Li_2CO_3$-$K_2CO_3$ salt.

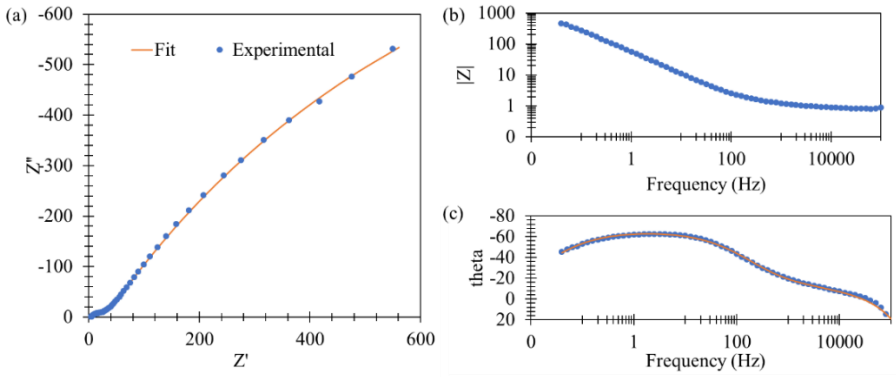


Figure 4.62. Nyquist (a) and Bode Plots (b,c) of Inconel 600 in composite $Li_2CO_3$-$K_2CO_3$ salt at 502 ˚C after electrochemical impedance spectroscopy measurements. The blue dots represent the experimental data. The orange line represents fitting with the equivalent model; figure 59a.

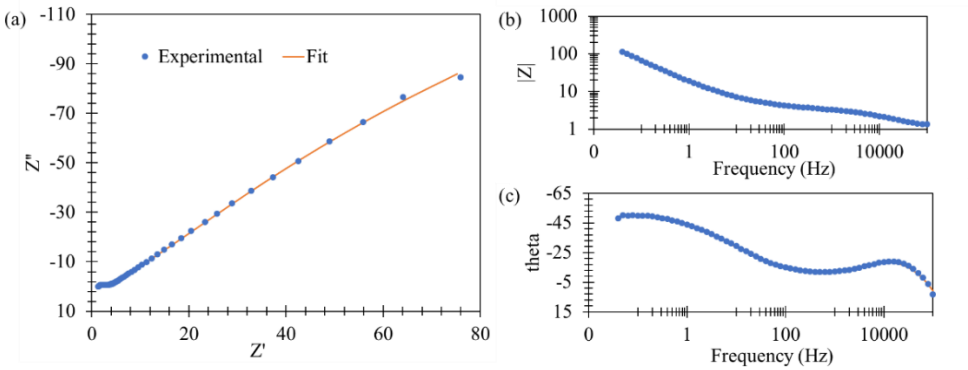


Figure 4.63. Nyquist (a) and Bode Plots (b,c) of Inconel 600 in composite $Li_2CO_3$-$K_2CO_3$ salt at 523 ˚C after electrochemical impedance spectroscopy measurements. The blue dots represent the experimental data. The orange line represents fitting with the equivalent model; figure 58b.

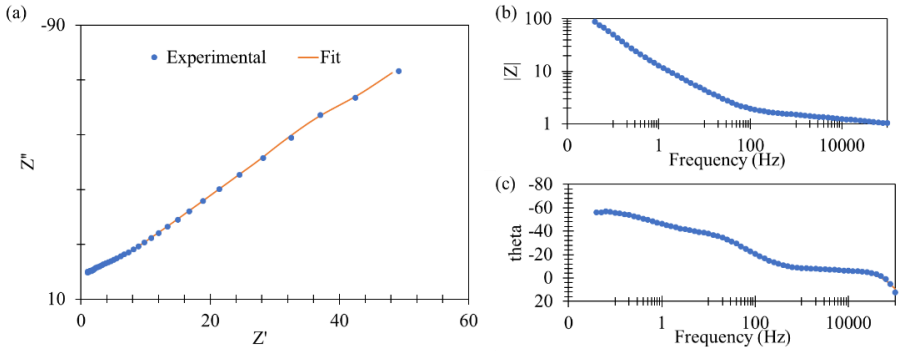


Figure 4.64. Nyquist (a) and Bode Plots (b,c) of Inconel 600 in composite $Li_2CO_3$-$K_2CO_3$ salt at 547 ˚C after electrochemical impedance spectroscopy measurements. The blue dots represent the experimental data. The orange line represents fitting with the equivalent model; figure 58b.

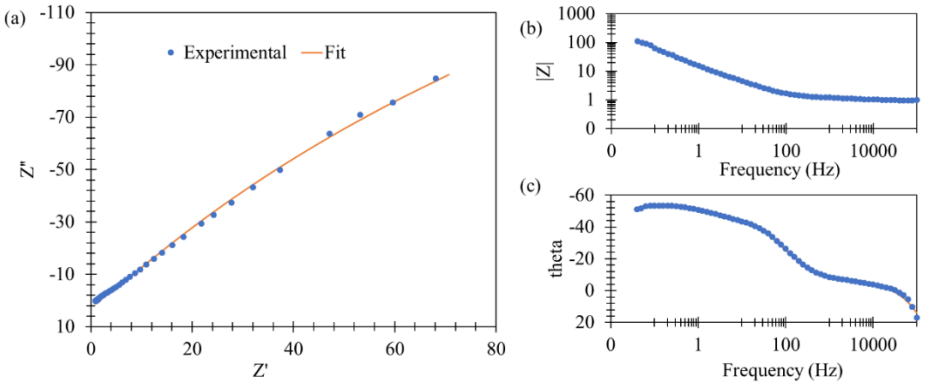


Figure 4.65. Nyquist (a) and Bode Plots (b,c) of Inconel 600 in composite $Li_2CO_3$-$K_2CO_3$ salt at 573 ˚C after electrochemical impedance spectroscopy measurements. The blue dots represent the experimental data. The orange line represents fitting with the equivalent model; figure 58b.

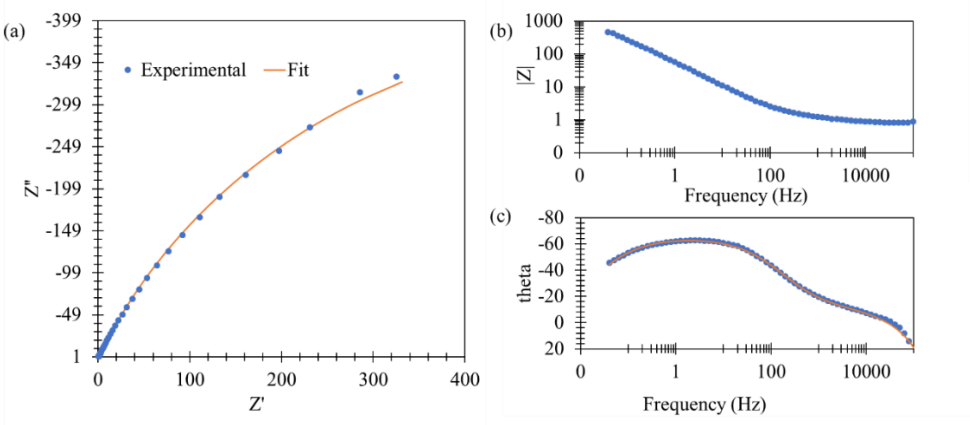


Figure 4.66. Nyquist (a) and Bode Plots (b,c) of Inconel 600 in composite $Li_2CO_3$-$K_2CO_3$ salt at 601 ˚C after electrochemical impedance spectroscopy measurements. The blue dots represent the experimental data. The orange line represents fitting with the equivalent model; figure 58c.

Table 4.21. Best fit values for various temperatures using appropriate equivalent circuits for Inconel 600 in composite $Li_2CO_3$-$K_2CO_3$ salt at various temperatures.

| Temperature (°C) | Rs (Ω cm2) | Tco (Ω-1S-pcm-2)-1 | Pco -1 | Rpo -1 (Ω cm2) | Tdl (Ω-1S-pcm-2) | Pdl | Rct (Ω cm2) | L (H) | W-R | W-T | W-P | Chi Square | SS |
|---|---|---|---|---|---|---|---|---|---|---|---|---|---|
| 502 | 2.76±0.01 | 1.47E-3±0.1 | 0.604±0.06 | 18.23±0.10 | 2.7E-3±0.003 | 0.657±0.005 | 2707±0.027 | | 12.5±0.09 | 4.9E-4±0.04 | 0.408±0.009 | 8.90E-05 | 0.011 |
| 523 | 1.037±0.02 | 2.09E-4±0.1 | 0.730±0.02 | 1.77±0.03 | 0.0223±0.02 | 0.696±0.03 | 576.7±0.1 | 5.04E-7±0.04 | 9.92±0.2 | 1.173±0.2 | 0.309±0.06 | 0.0002 | 0.027 |
| 547 | 0.773±0.1 | 32.1±0.05 | 0.666±0.005 | 2.54±0.08 | 5.11E-3±0.4 | 0.466±0.1 | 350.4±0.03 | 4.77E-7±0.06 | 0.764±0.1 | 0.0241±0.07 | 0.775±0.03 | 0.000403 | 0.048 |
| 573 | 0.859±0.04 | 0.0257±0.1 | 0.788±0.06 | 2.004±0.2 | 0.0211±0.007 | 0.681±0.02 | 592.2±0.1 | 4.47E-7±0.05 | 0.283±0.2 | 5.82E-7±0.2 | 0.329±0.2 | 0.000864 | 0.10287 |
| 601 | 0.706±0.03 | | | | 4.58±0.005 | 0.733±0.002 | 1165±0.02 | 5.13E-7±0.03 | 0.392±0.1 | 2.15E-4±0.2 | 0.320±0.10 | 0.000737 | 0.089862 |

#### 4.2.3.4 Corrosion mechanism of Inconel 600 in the composite GDC salt

Figure 4.67 shows the corrosion mechanism of Inconel 600 in relation to oxide layer and change in temperature. At 600 °C, there is only a formation of one oxide layer, However, as the temperature increases, two oxide layers are formed on the surface of the electrode.

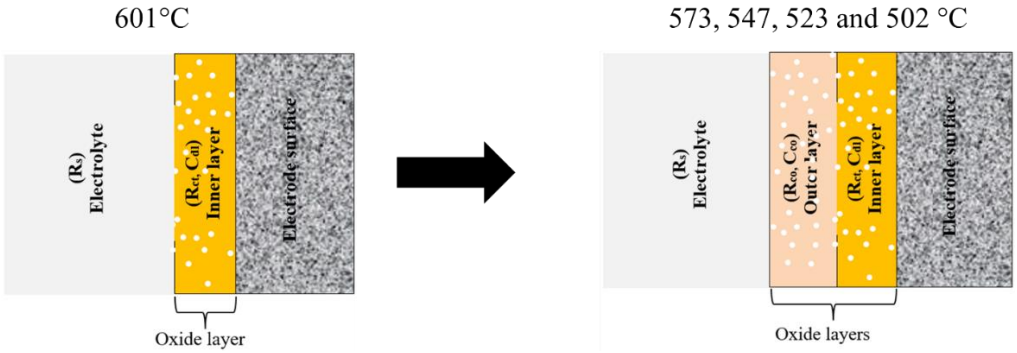


Figure 4.67. Corrosion mechanism for Inconel 600 in molten carbonate 0.3 GDC – 0.7 ($0.67Li_2CO_3$-$0.33K_2CO_3$) salts with varying temperatures of 502 °C, 523 °C, 547 °C, 573 °C and 601 °C, displaying the number of oxide layers formed of the surface of the electrode as modelled by Figure 4.61.

### 4.2.4. Summary of Electrochemical Measurements of electrodes in 0.3 GDC – 0.7 ($0.67Li_2CO_3$-$0.33K_2CO_3$) composite salt

Stainless steel 304, nickel and Inconel 600 were tested in molten 0.3 GDC – 0.7 (0.67Li2CO3-0.33K¬2CO3) composite salt. From the LPR measurements, Nickel showed more resilience to the molten salt, with higher $R_p$ values than stainless steel and Inconel 600 at approximately 500 °C and 600 °C. Stainless steel 304 however, showed very high resistances as well, whiles Inconel showed the least. Tafel measurements showed the least values of $i_{corr}$ for nickel suggesting a decelerated corrosion. However, Inconel 600 showed a different trend, in that it $i_{corr}$ increased as temperature increased, suggesting that Inconel 600 does better at higher temperatures. EIS measurements reaveled diffusion of charge carriers through the oxide layer at lower temperatures for stainless steel 304 with low permeability of oxide layer by salt. The equivalent circuit for nickel did not vary as temperature changed, meaning the oxide layer remained stable throughout the experiment. This can be seen by the consistent and high P values which suggest a very low permeability of salt through the oxide layer. The presence of the Warburg element in modeling the Inconel 600 data fit, suggest a constant diffusion of charge carries through the oxide layer. Nickel performed the best in the composite salt compared to stainless steel 304 and Inconel 600, with Inconel 600 performing better at higher temperatures in like manner with Nickel.

# Chapter 5: Conclusion

The Parametric study determined that scan rate of 1 mV/s with a step height of 0.1mV and a step time of 0.1 second is appropriate for electrochemical techniques measurements. It was also determined that larger step heights and times do not allow the system to stabilize before reading a potential and give rise to increasing error and variation. LPR, Tafel and EIS were applied for the study of the corrosion of stainless steel 304, nickel, and Inconel 600 in molten eutectic and composite salt. LPR and Tafel allowed for quick analysis of the three metals, whereas EIS allows for a more in-depth analysis with regards to kinetics.

The LPR analysis allowed for the measurements of $R_p$ for each individual electrode in both salts. The values of Rp for stainless steel 304 increased with decreasing temperature from 182 $\Omega.cm^2$ to 4862$\Omega.cm^2$ in the eutectic salt, and is significantly higher than the $R_p$ values of Nickel in the eutectic salt. For example, at ~500 °C the $R_p$ values of stainless steel 304 is 4862 $\Omega.cm^2$ and that of nickel is 1876 $\Omega.cm^2$ which is more than twice as much as the $R_p$ values for nickel and more than twenty times that of Inconel 600. At ~575 °C however, the $R_p$ value for nickel is higher than stainless steel 304 but subsequently reduces and then starts to increase as temperature decreases. Inconel 600 follows behind Nickel with the least values of $R_p$ from 513.2 $\Omega.cm^2$ to 225.5 $\Omega.cm^2$. Among all the three metals Inconel 600 has the highest $R_p$ at 600 °C. Stainless steel has least cathodic values for OCP. From the Tafel measurements anodic and cathodic reactions and slopes can be obtained. Stainless steel 304 reacts quickly with the salt therefore it has high anodic values compared to Nickel and Inconel 600. Between nickel and Inconel 600, Inconel 600 reacts quickly than nickel based on higher anodic values. The corrosion rate suggests that nickel is the best in the molten eutectic salt owing to slower anodic reaction. However, stainless steel is more resistant to the salt.

The EIS method provided information on the formation of oxide layers, number of oxide layers, permeability and stability of the oxide layers to the salt. Stainless steel 304 had two time constants which represent an outer and inner layer of oxide. Nickel showed two time constant except for 604 °C and 573 °C which show three time constants representing the formation of a short lived third layer. Inconel 600 also displayed two time constants, but at 577 °C there appears to be a third time constant which is short lived and not visible at 600 °C. The $R_{ct}$ values, which represent the resistance of the layer closest to the electrode, of stainless steel are very high, indicating a very resistant inner oxide layer. The $R_{ct}$ value of stainless steel 304 range from 3700 $\Omega.cm^2$ to 6000 $\Omega.cm^2$. Inconel 600 displayed the next highest values of $R_{ct}$, however the presence of the Warburg element at 552 °C indicates the instability of the oxide layer. Nickel showed the least in the $R_{ct}$ values as a result of the presence of a Warburg element at all temperatures. The $P_{dl}$ values represent

the permeability of the first oxide layer to the salt. The $P_{dl}$ values of stainless steel is are very similar and is an indication of the stability of the oxide layer. The presence of the dramatic decrease in at 600 °C for stainless steel can be attributed to the presence of the Warburg element. At 600 °C, Inconel 600 has the highest resistance followed by nickel. However, stainless steel does not perform very well at high temperatures.

In the composite salt, nickel has the least cathodic values for OCP employing the LPR method. Nickel also has the highest vales for $R_p$ (9200 Ω.cm$^2$ to 600 Ω.cm$^2$) in the composite salt, performing better than Stainless steel (3800 Ω.cm$^2$ to 156 Ω.cm$^2$) and Inconel (250 Ω.cm$^2$ to 547 Ω.cm$^2$). Between stainless steel and Inconel, stainless steel 304 has the highest resistance at 502 °C and 523 °C and decreases in $R_p$ value with increasing temperature. However, Inconel 600 increases in $R_p$ with increasing temperature, making Inconel 600 the best in this regard. The Tafel measurements describe the anodic and cathodic reactions. The corrosion of Nickel is much accelerated than stainless steel 304 and Inconel 600. This can be seen in the large anodic slope (ba) values in Table 4.17. The OCP of nickel is less cathodic compared to the other alloys and moves to more anodic values as temperature decreases. The $i_{corr}$ values of nickel is also less than stainless steel and Inconel. At ~ 502 and 528, stainless steel performs better in the composite salt than Inconel 600. However, as temperature continues to increase Inconel performs better than stainless steel. This makes nickel the first choice, Inconel 600 the second choice and stainless steel the third choice for suitability in the molten salt.

The EIS measurements in the composite salt for stainless steel reveal two time constants, representing two oxide layers. Nickel also reveals two time constants as well as Inconel 600. Nickel performs exceptionally well in the composite salt with no presence of the Warburg element, suggesting a more resistant oxide layer than Inconel and stainless steel. The $R_{ct}$ values for nickel are very high, more than twice that of Inconel 600 and stainless steel 304. The $P_{dl}$ and $P_{co}$ values for nickel are very similar at all temperatures. The $P_{co}$ values for nickel are also really high and suggest a less permeable second oxide layer. The $R_{po}$ values for nickel are also a lot higher than stainless steel 304 and Inconel 600 at all temperatures. Inconel performs the second best in the composite salt with higher $R_{ct}$ values than stainless steel. The EIS measurements suggest that nickel performs the best at all temperatures. However, at higher temperatures Inconel 600 proved to have the highest resistance.

**References**


[1] Y. Q. Wang, N. Li, and B. Yang, “Effect of ferrite on pitting corrosion of Fe20Cr9Ni cast austenite stainless steel for nuclear power plant pipe,” *Corros. Eng. Sci. Technol.*, vol. 50, no. 4, pp. 330–337, May 2015.

[2] M. Mayuzumi, J. Tani, and T. Arai, “Chloride induced stress corrosion cracking of candidate canister materials for dry storage of spent fuel,” *Nucl. Eng. Des.*, vol. 238, no. 5, pp. 1227–1232, May 2008.

[3] L. Wang, B. Kang, N. Gao, X. Du, L. Jia, and J. Sun, “Corrosion behaviour of austenitic stainless steel as a function of methanol concentration for direct methanol fuel cell bipolar plate,” *J. Power Sources*, vol. 253, pp. 332–341, May 2014.

[4] Y. Yang, L. Guo, and H. Liu, “Influence of fluoride ions on corrosion performance of 316L stainless steel as bipolar plate material in simulated PEMFC anode environments,” *Int. J. Hydrog. Energy*, vol. 37, no. 2, pp. 1875–1883, Jan. 2012.

[5] T. Evans, J. Olson, V. Bhat, and S.-H. Lee, “Corrosion of stainless steel battery components by bis(fluorosulfonyl)imide based ionic liquid electrolytes,” *J. Power Sources*, vol. 269, pp. 616–620, Dec. 2014.

[6] N. S. Patel, V. Pavlík, and M. Boča, “High-Temperature Corrosion Behavior of Superalloys in Molten Salts – A Review,” *Crit. Rev. Solid State Mater. Sci.*, vol. 42, no. 1, pp. 83–97, Jan. 2017.

[7] A. Nishikata, G. Zhang, and T. Tsuru, “Rapid Evaluation of Corrosion Resistance of Ni-Base Alloys in Molten Salts Using AC Impedance Method,” *Mater. Trans. JIM*, vol. 38, no. 4, pp. 312–318, 1997.

[8] K. Vignarooban, P. Pugazhendhi, C. Tucker, D. Gervasio, and A. M. Kannan, “Corrosion resistance of Hastelloys in molten metal-chloride heat-transfer fluids for concentrating solar power applications,” *Sol. Energy*, vol. 103, pp. 62–69, May 2014.

[9] W.-J. Cheng, D.-J. Chen, and C.-J. Wang, “High-temperature corrosion of Cr–Mo steel in molten LiNO3–NaNO3–KNO3 eutectic salt for thermal energy storage,” *Sol. Energy Mater. Sol. Cells*, vol. 132, pp. 563–569, Jan. 2015.

[10] A. Kruizenga and D. Gill, “Corrosion of Iron Stainless Steels in Molten Nitrate Salt,” *Energy Procedia*, vol. 49, pp. 878–887, Jan. 2014.

[11] K. Takeuchi, A. Nishijima, K. Ui, N. Koura, and C.-K. Loong, “Corrosion Behavior of Fe-Cr Alloys in Li2CO3-K2CO3 Molten Carbonate,” *J. Electrochem. Soc.*, vol. 152, no. 9, pp. B364–B368, Sep. 2005.

[12] S. Frangini and S. Loreti, “The role of alkaline-earth additives on the molten carbonate corrosion of 316L stainless steel,” *Corros. Sci.*, vol. 49, no. 10, pp. 3969–3987, Oct. 2007.

[13] A. A. Attia, S. A. Salih, and A. M. Baraka, “Corrosion and passivation behaviors of some stainless steel alloys in molten alkali carbonates,” *Electrochimica Acta*, vol. 48, no. 2, pp. 113–118, Nov. 2002.

[14] W. Wu, Y. Zhang, D. Ding, and T. He, “Achieving Direct Electrochemical Oxidation of Carbon below 600oC through a Novel Direct Carbon Fuel Cell,” *ArXiv Prepr. ArXiv180205789*, 2018.

[15] K. Jüttner, “Electrochemical impedance spectroscopy (EIS) of corrosion processes on inhomogeneous surfaces,” *Electrochimica Acta*, vol. 35, no. 10, pp. 1501–1508, Oct. 1990.

[16] M. Sarvghad, T. A. Steinberg, and G. Will, “Corrosion of steel alloys in eutectic NaCl+Na2CO3 at 700°C and Li2CO3 + K2CO3 + Na2CO3 at 450°C for thermal energy storage,” *Sol. Energy Mater. Sol. Cells*, vol. 170, pp. 48–59, Oct. 2017.

[17] G. W. Walter, “A review of impedance plot methods used for corrosion performance analysis of painted metals,” *Corros. Sci.*, vol. 26, no. 9, pp. 681–703, Jan. 1986.

[18] G. H. Meier, “A review of advances in high-temperature corrosion,” *Mater. Sci. Eng. A*, vol. 120–121, pp. 1–11, Nov. 1989.
[19] Y. Xie, S. Guo, A. Leong, J. Zhang, and Y. Zhu, “Corrosion behaviour of stainless steel exposed to highly concentrated chloride solutions,” *Corros. Eng. Sci. Technol.*, vol. 52, no. 4, pp. 283–293, May 2017.
[20] C. S. Ni and L. Y. Lu, “Electrochemical Impedance and Modelling Studies of the Corrosion of Three Commercial Stainless Steels in Molten Carbonate,” *International Journal of Corrosion*, 2014. [Online]. Available: https://www.hindawi.com/journals/ijc/2014/721208/. [Accessed: 23-Aug-2018].
[21] Z. He and F. Mansfeld, “Exploring the use of electrochemical impedance spectroscopy ( EIS ) in microbial fuel cell studies,” *Energy Environ. Sci.*, vol. 2, no. 2, pp. 215–219, 2009.
[22] R. Schurch, S. M. Rowland, R. S. Bradley, and P. J. Withers, “Imaging and analysis techniques for electrical trees using X-ray computed tomography,” *IEEE Trans. Dielectr. Electr. Insul.*, vol. 21, no. 1, pp. 53–63, Feb. 2014.
[23] M. Kouřil, P. Novák, and M. Bojko, “Limitations of the linear polarization method to determine stainless steel corrosion rate in concrete environment,” *Cem. Concr. Compos.*, vol. 28, no. 3, pp. 220–225, Mar. 2006.
[24] W. J. Lorenz and F. Mansfeld, “Determination of corrosion rates by electrochemical DC and AC methods,” *Corros. Sci.*, vol. 21, no. 9, pp. 647–672, Jan. 1981.
[25] G. Hinds, “The electrochemistry of corrosion,” *Natl. Physic Lab.*
[26] “Calculation of Corrosion Rate.” [Online]. Available: https://www.gamry.com/Framework%20Help/HTML5%20-%20Tripane%20-%20Audience%20A/Content/DC/Introduction_to_DC_Corrosion/Calculation%20of%20Corrosion%20Rate.htm. [Accessed: 14-May-2018].
[27] F. Kuang *et al.*, “Electrochemical Methods for Corrosion Monitoring: A Survey of Recent Patents~!2009-10-01~!2009-11-25~!2010-02-18~!,” *Recent Pat. Corros. Sci.*, vol. 2, no. 1, pp. 34–39, Mar. 2010.
[28] “The-Basics-of-EIS-Part-3.pdf.” .
[29] C. L. Zeng, W. Wang, and W. T. Wu, “Electrochemical impedance models for molten salt corrosion,” *Corros. Sci.*, vol. 43, no. 4, pp. 787–801, Apr. 2001.
[30] A. G. Fernández, A. Rey, I. Lasanta, S. Mato, M. P. Brady, and F. J. Pérez, “Corrosion of alumina-forming austenitic steel in molten nitrate salts by gravimetric analysis and impedance spectroscopy,” *Mater. Corros.*, vol. 65, no. 3, pp. 267–275, Mar. 2014.
[31] C. L. Zeng and J. Li, “Electrochemical impedance studies of molten (0.9Na,0.1K)2SO4-induced hot corrosion of the Ni-based superalloy M38G at 900°C in air,” *Electrochimica Acta*, vol. 50, no. 28, pp. 5533–5538, Sep. 2005.
[32] S. Frangini, A. Masci, and F. Zaza, “Molten salt synthesis of perovskite conversion coatings: A novel approach for corrosion protection of stainless steels in molten carbonate fuel cells,” *Corros. Sci.*, vol. 53, no. 8, pp. 2539–2548, Aug. 2011.
[33] Q. X. Fu, S. W. Zha, W. Zhang, D. K. Peng, G. Y. Meng, and B. Zhu, “Intermediate temperature fuel cells based on doped ceria–LiCl–SrCl2 composite electrolyte,” *J. Power Sources*, vol. 104, no. 1, pp. 73–78, 2002.
[34] M. Cassir, S. J. McPhail, and A. Moreno, “Strategies and new developments in the field of molten carbonates and high-temperature fuel cells in the carbon cycle,” *Int. J. Hydrog. Energy*, vol. 37, no. 24, pp. 19345–19350, Dec. 2012.
[35] B. Zhu, X. Liu, P. Zhou, X. Yang, Z. Zhu, and W. Zhu, “Innovative solid carbonate–ceria composite electrolyte fuel cells,” *Electrochem. Commun.*, vol. 3, no. 10, pp. 566–571, Oct. 2001.

[36] H.-J. Choi *et al.*, “Enhanced electrochemical performance of metal-supported solid oxide fuel cells via an inner coating of Gd0.1Ce0.9O2-δ nanosol in the porous NiFe-metal support,” *J. Power Sources*, vol. 406, pp. 81–87, Dec. 2018.
[37] “Polarization Resistance Tutorial.” [Online]. Available: https://www.gamry.com/application-notes/corrosion-coatings/corrosion-techniques-polarization-resistance/. [Accessed: 13-Feb-2018].
[38] “Electrochemical Corrosion Measurements-Galvanic Corrosion.” [Online]. Available: https://www.gamry.com/application-notes/corrosion-coatings/basics-of-electrochemical-corrosion-measurements/. [Accessed: 13-Feb-2018].
[39] D. G. Enos and L. L. Scribner, “The Potentiodynamic Polarization Scan,” Solartron Analytical, 33.
[40] C. Andrade and C. Alonso, “Test methods for on-site corrosion rate measurement of steel reinforcement in concrete by means of the polarization resistance method,” *Mater. Struct.*, vol. 37, no. 9, pp. 623–643, Nov. 2004.
[41] S. Frangini, “Testing procedure to obtain reliable potentiodynamic polarization curves on type 310S stainless steel in alkali carbonate melts,” *Mater. Corros.*, vol. 57, no. 4, pp. 330–337, Apr. 2006.
[42] S. Choudhary, A. Garg, and K. Mondal, “Relation Between Open Circuit Potential and Polarization Resistance with Rust and Corrosion Monitoring of Mild Steel,” *J. Mater. Eng. Perform.*, vol. 25, no. 7, pp. 2969–2976, Jul. 2016.
[43] Y. Wang, H. Liu, G. Yu, J. Hou, and C. Zeng, “Electrochemical study of the corrosion of a Ni-based alloy GH3535 in molten (Li,Na,K)F at 700°C,” *J. Fluor. Chem.*, vol. 178, pp. 14–22, Oct. 2015.
[44] F. K. Sahrani, M. Aziz, Z. Ibrahim, and A. Yahya, “Open circuit potential study of stainless steel in environment containing marine sulphate-reducing bacteria,” *Sains Malays.*, vol. 37, no. 4, pp. 359–364, 2008.
[45] M. Sarvghad, T. A. Steinberg, and G. Will, “Corrosion of stainless steel 316 in eutectic molten salts for thermal energy storage,” *Sol. Energy*, vol. 172, pp. 198–203, Sep. 2018.
[46] D. D. Macdonald, “The Point Defect Model for the Passive State,” *J. Electrochem. Soc.*, vol. 139, no. 12, pp. 3434–3449, Dec. 1992.
[47] C. M. Abreu, M. J. Cristóbal, R. Losada, X. R. Nóvoa, G. Pena, and M. C. Pérez, “High frequency impedance spectroscopy study of passive films formed on AISI 316 stainless steel in alkaline medium,” *J. Electroanal. Chem.*, vol. 572, no. 2, pp. 335–345, Nov. 2004.
[48] C. Exartier, S. Maximovitch, and B. Baroux, “Streaming potential measurements on stainless steels surfaces: evidence of a gel-like layer at the steel/electrolyte interface,” *Corros. Sci.*, vol. 46, no. 7, pp. 1777–1800, Jul. 2004.
[49] G. Y. Lai, *High Temperature Corrosion and Materials Application*. ASM International, 2007.
[50] S. Torabi *et al.*, “Rough Electrode Creates Excess Capacitance in Thin-Film Capacitors,” *ACS Appl. Mater. Interfaces*, vol. 9, no. 32, pp. 27290–27297, Aug. 2017.
[51] C. S. Ni, L. Y. Lu, C. L. Zeng, and Y. Niu, “Electrochemical impedance studies of the initial-stage corrosion of 310S stainless steel beneath thin film of molten (0.62Li,0.38K)2CO3 at 650°C,” *Corros. Sci.*, vol. 53, no. 3, pp. 1018–1024, Mar. 2011.